2021

Fabricating delivery platforms for wound management and tissue regeneration

Luciana Yumiko Daikuara

UNIVERSITY
OF WOLLONGONG
AUSTRALIA

Fabricating delivery platforms for wound management and tissue regeneration

Luciana Yumiko Daikuara

Under the supervision of Zhilian Yue, Danielle Skropeta, and Gordon G. Wallace

This thesis is presented as part of the requirement for the conferral of the degree of Doctor of Philosophy from University of Wollongong

University of Wollongong
Intelligent Polymer Research Institute

July 2021

This thesis is dedicated to my beloved parents, Manoel and Julia, and my brother, Daniel for their unconditional love and support every step of the way.

Certification

I, Luciana Yumiko Daikuara, declare that this thesis submitted in fulfilment of the requirements for the conferral of the degree Doctor of Philosophy, from the University of Wollongong, is wholly my own work unless otherwise referenced or acknowledged. This document has not been submitted for qualifications at any other academic institution.

Luciana Yumiko Daikuara

July 2021

Abstract

Skin provides the protective surface for animals and humans and is therefore prone to physical, chemical, and biological injuries. In all but superficial wounds, the capacity to repair by regeneration is lost and the mechanisms involved in wound closure are unable to restore the skin's original functions. In this context, skin repair is achieved using surgical techniques including skin grafts, and a range of synthetic or biological scaffolds. Wounds impact millions of patients every year and represent a serious cause of morbidity and mortality worldwide. The increase in need for better skin repair, in part due to issues such as the aging population coupled with chronic conditions has driven the development of products to enhance therapeutic outcomes, yet current treatment outcomes are far from ideal and complete replication of the cellular structure and tissue functional requirements of skin remains a challenge.

General aims: Address the major drawbacks of available skin substitutes and delivery system platforms. Herein two approaches are proposed, the first one (Chapters 2-3) involves the development and initial in vitro characterization of a 3D multifunctional bioprinted platform based on platelet lysate, which could be used to deliver cells and growth factors to the wound site while providing a supportive network that mimics the native ECM for skin cells to infiltrate and thrive. This system was designed with the aim of providing an advanced alternative to current skin grafts and skin substitutes available for clinical use. The second system proposed (Chapter 4) is based on an electrofluidic approach for control of bioactive molecule delivery into soft tissue model using threads and surgical sutures which was designed with the aim of being used in sutures for surgical wound closure.

Methods: (Chapter 2-3) 3D printed HDF-PLGMA bioink were fabricated using a pneumatic extrusion-based 3D Bioplotter. The epidermal-dermal model was fabricated by seeding HaCaT on top of 3D printed HDF-PLGMA constructs. The innervated dermal model was fabricated by seed hNSC H9 neurospheres to the bottom of 3D printed HDF-PLGMA constructs. (Chapter 4) Commonly employed surgical sutures were used to create an adequate fluid connection between the electrodes and a tissue-like 3D hydrogel support. The platform consisted of two reservoirs into which the ends of the thread/suture were immersed. The anode and cathode were placed separately into each reservoir. The thread/suture was taken from one reservoir to the other through the gel. When the current was applied, biomolecules loaded onto the thread/suture were directed into the gel, and the rate of movement of the biomolecules was dependent on the magnitude of the current.

Results: (Chapter 2) Briefly, the work described in this chapter relates to the development of a multifunctional bioink consisting of PL and GelMA (PLGMA) and the biofabrication of a 3D printed dermal-like structure. The data presented shows that the proposed PLGMA bioink meets essential requirements of printability in terms of rheological properties and shape fidelity. Moreover, its mechanical properties can be readily tuned to achieve stiffness that is equivalent to native skin tissue. Biologically relevant factors were successfully released in a sustainable manner and the bioavailability of those factors was demonstrated by high cell viability, good cell attachment, and improved proliferation of printed dermal fibroblasts, as well as by upregulation of ECM synthesis by dermal fibroblasts. (Chapter 3) Continuing the work described in chapter 2, chapter 3 relates the fabrication of a more complex skin equivalent based on the PLGMA platform previously established. Bilayer skin model:

The expression of general keratinocyte differentiation markers was used to confirm the capacity of the platform to promote normal epithelial morphogenesis and differentiation of keratinocytes. Innervated skin model: The expression of development neuronal markers, as well as a general neuronal marker, was used to demonstrate that the proposed platform supported hNSC-H9 neurosphere neurite outgrowth and neuronal differentiation. Challenges faced in the co-incorporation of HaCaT and hNSC-H9 neurospheres to HDF-PLGMA construct that need to be considered to progress with this research will also be presented. (Chapter 4) A novel electrofludic system for the controlled release of bioactive molecules such as small molecules, drugs, polysaccharides, or proteins via an electric field is described for the first time. In a proof-of-concept study, the controlled delivery of dexamethasone 21-phosphate disodium salt (DSP), a clinically relevant anti-inflammatory prodrug, as well as other molecules were used to demonstrate the feasibility of the proposed system. Despite being peripherally related to the overall PhD theme; this system could be potentially integrated in the PLGMA matrix by printing the 3D skin cells-PLGMA on top of the suture for precise delivery of growth factors and cells to sutured wounds.

Taken together, although it is still at an early stage of development, the bioprinting platform, as well as the electrofludic systems demonstrated to hold potential as a foundation for the fabrication of complex and physiologically relevant delivery platforms for wound management and tissue regeneration.

.

Acknowledgments

I would like to express my sincere gratitude to my supervisors Prof. Gordon Wallace, Zhilian Yue and A/Prof Danielle Skropeta for their continuous support and guidance throughout my PhD study. I decided to apply for this PhD position after watching the online course 'Bioprinting: 3D Printing of Body Parts' offered by UOW, where Prof Gordon talked about bioprinting and 'the world of exciting possibilities' this technology will open over the coming years. His enthusiasm for innovation and love for what he does sparked my own motivation and kept me going. It was a great honour for me to work under the supervision of an internationally renowned scientist. To Zhilian, who patiently guided me from day one, gave encouragement, countless advice and all support to ensure everything was alright, I will be forever thankful. I am really grateful for the opportunity to be part of ARC Centre of Excellence for Electromaterials Science (ACES) and Intelligent Polymer Research Institute, which opened many doors for collaborative research and networking. I also would like to extend my gratitude to all the past and present members of IPRI and collaborators, especially Mirella Dottori and Sara Miellet. Special thanks to FIL4IT, who would always make my day a little brighter with his great sense of humour and iconic desktop wallpaper.

To my beloved family and dearest friends, words cannot describe how thankful I am for your unconditional love and emotional / active support over this past 4 years. Because you were there to encourage me throughout the entire process and comfort me when I was down, I could cry a little less, create many wonderful memories and enjoy this journey a lot more. Lastly, I would like to thank God, for all that I am and all that I have. A thousand times I've failed, still Your mercy remains, so I thank you for Your grace and everlasting love.

List of Abbreviations

ADMSC	Adipose-derived mesenchymal stem cells
AFS	Amniotic fluid-derived stem cells
ALI	Air-liquid interface
BDNF	Brain-derived neurotrophic factor
BM-MSC	Bone marrow-derived mesenchymal stem cells
BRN3A	Brain-specific homeobox/POU domain protein 3a
CAD	Computer-aided-design
CEA	Cultured epithelial autografts
CK	Cytokeratin
DFUs	Diabetic foot ulcers
DLP	Digital light processing
DSP	Dexamethasone 21-phosphate disodium salt
EC	Human endothelial cells
ECM	Extracellular matrix
EGF	Epidermal growth factor
FBS	Fetal bovine serum
FGF	Fibroblast growth factor
FITC-BSA	Fluorescein isothiocyanate labelled bovine serum albumin
FITC-dextran	Fluorescein isothiocyanate labelled dextran
FTSG	Full-thickness skin graft
GAGs	Glycosaminoglycans
GDNF	Glial cell line-derived neurotrophic factor
GelMA	Gelatin methacryloyl

HA	Hyaluronic acid
HaCaT	Immortalized human keratinocytes
HDF	Primary human dermal fibroblasts
HEK	Primary human epidermal keratinocytes
HEM	Human epidermal melanocytes
hEPC	Human endothelial progenitor cells
HEPES	4-(2-hydroxyethyl) piperazine-1-ethanesulfonic acid
HGF	Hepatocyte growth factor
hNSC-H9	Embryonic stem cell-derived human neural stem cells
HPAd	Human preadipocytes
hPC-PL	Human pericytes from placenta
HUVEC	Human umbilical vein endothelial cells
HUVEC	Human umbilical vein endothelial cells
IGF-1	Insulin-like growth factor 1
IL	Interleukin
KGF	Keratinocyte growth factor
LaBP	Laser-assisted bioprinting
LAP	Lithium phenyl-2,4,6-trimethylbenzoylphosphinate
MAP 2	Microtubule-associated protein 2
MMP	Matrix metalloproteases
MMP	Matrix metalloproteinases
MSC	Mesenchymal stem cells
NGF	Nerve growth factor
NIH3T3	Immortalized non-tumorigenic murine fibroblast

NT-3	Neurotrophin-3
OCT	Optimal cutting temperature
P/S	Penicillin/streptomycin
PBS	Phosphate buffered saline
PCL	Polycaprolactone
PDGF	Platelet derived growth factor
PE2	Prostaglandin E2
PEG	Polyethylene glycol
PFA	Paraformaldehyde
PG	Proteoglycans
PI	Propidium iodide
PL	Human platelet lysate
PRP	Platelet-rich plasma
PVP	Poly(vinyl pyrrolidone)
RGD	Arginine-glycine-aspartic acid
STSG	Split-thickness skin graft
TGF	Transforming growth factor
TN-α	Tumour necrosis factor α
TRIS	Tris(hydroxymethyl)aminomethane
TrK	Tropomyosin receptor kinase
VEGF	Vascular endothelial growth factor
VLU	Venous leg ulcers
α-SMA	Smooth muscle alpha-actin

List of Publications

(Published) Daikuara, L.Y., Chen, X., Yue, Z., Skropeta, D., Wood, F., Wallace, G.G. (2021) Bioprinting for complex skin constructs fabrication. Advanced Functional Materials, 202105080

(Published) Daikuara, L.Y., Yue, Z., Skropeta, D., Wallace, G.G. (2021) *In vitro* characterisation of 3D printed platelet lysate-based bioink for potential application in skin tissue engineering. Acta Biomaterialia. 123:286-297.

Co-author (equal contribution) Cabot, J., **Daikuara, L. Y.**, Yue, Z., Hayes, P., Liu, X., Wallace, G. G. & Paull, B. (2020). Electrofluidic control of bioactive molecule delivery into soft tissue models based on gelatin methacryloyl hydrogels using threads and surgical sutures. Scientific Reports, 10 (1).

(Collaboration) Ruland, A., Gilmore, K. J., **Daikuara, L. Y.**, Fay, C. D., Yue, Z. & Wallace, G. G. (2019). Quantitative ultrasound imaging of cell-laden hydrogels and printed constructs. Acta Biomaterialia, 91 173-185.

(Collaboration) Molino, P.J, Will J., **Daikuara, L.Y.**, Harris, A.R., Yue, Z., Dinoro, J., Winberg, P., Wallace, G.G. (2021). Fibrinogen, collagen, and transferrin adsorption to poly(3,4-ethylenedioxythiophene)-xylorhamno-uronic glycan composite conducting polymer biomaterials for wound healing applications. Biointerphases, 16(2):021003.

List of Conferences

Daikuara, L. Y., Yue, Z., Skropeta**,** D., Wallace G. G. Human Platelet Lysate-based platforms for Wound Healing Application. 14th Annual International ARC Centre of Excellence for Electromaterials Science Symposium. 5th – 7th February 2020, Canberra, Australia. (poster presentation)

Daikuara, L. Y., Yue, Z., Skropeta**,** D., Wallace G. G. Human Platelet Lysate-Based Bioink for Wound Healing Application. Tissue Engineering & Regenerative Medicine International Society - AP Chapter and the 7th Asian Biomaterials Congress (TERMIS-AP + ABMC7). 14th – 17th October 2019, Brisbane, Australia. (Oral presentation)

Daikuara, L. Y., Yue, Z., Skropeta**,** D., Wallace G. G. Fabricating Delivery System for Wound Healing. Annual Conference of the International Society for Biofabrication (ISBF). 28th - 31th October 2018, Würzburg, Germany. (Poster presentation)

Daikuara, L. Y., Yue, Z., Skropeta**,** D., Wallace G. G. Fabricating Delivery System for Wound Healing. ARC Centre of Excellence for Electromaterials Science Full Centre meeting. 19th – 20th July, Melbourne, Australia. (Poster presentation)

Daikuara, L. Y., Yue, Z., Skropeta**,** D., Wallace G. G. Fabricating Delivery System for Wound Healing. 26th Annual Conference of the Australasian Society for Biomaterials and Tissue Engineering (ASBTE). 3rd – 5th April 2018, Fremantle, Australia. (Oral / Poster presentation)

Daikuara, L. Y., Yue, Z., Skropeta, D., Wallace G. G. Fabricating Delivery System for Wound Healing. International Conference on Nanoscience and Nanotechnology (ICONN). 29th Jan - 2nd Feb 2018, Wollongong, Australia (Poster presentation)

List of Figures

List of Tables

Table of Contents

1 Chapter

Introduction

Part of the review presented in this chapter formed the basis of a first author review paper published to the journal Advanced Functional Materials 1616-301X (2021). https://doi.org/10.1002/adfm.202105080 by Daikuara, Luciana Y.; Chen, Xifang; Yue, Zhilian; Skropeta, Danielle; Wood, Fiona M.; Fear, Mark W.; Wallace, Gordon G. Bioprinting for complex skin constructs fabrication

Table of Contents

1.1 Introduction

This general introductory chapter includes the background information about the skin, wound healing, current treatments, and the need for advanced alternatives. The 3D printing and electrofluidic approaches this thesis will be focussing on, as well as the gaps in the clinic that are driving the investigation will also be introduced in this chapter. Relevant information will be further discussed in corresponding chapters. Briefly, following chapters 2-3 will detail the development and initial *in vitro* characterisation of a 3D multifunctional bioprinted platform based on platelet lysate. Chapter 4 will detail the design and proof-of-concept study of the electrofluidic approach for controlled delivery of bioactive molecule into soft tissue model using threads/surgical sutures. Lastly, chapter 5 will present the conclusion and future directions of this research.

1.2 Skin tissue

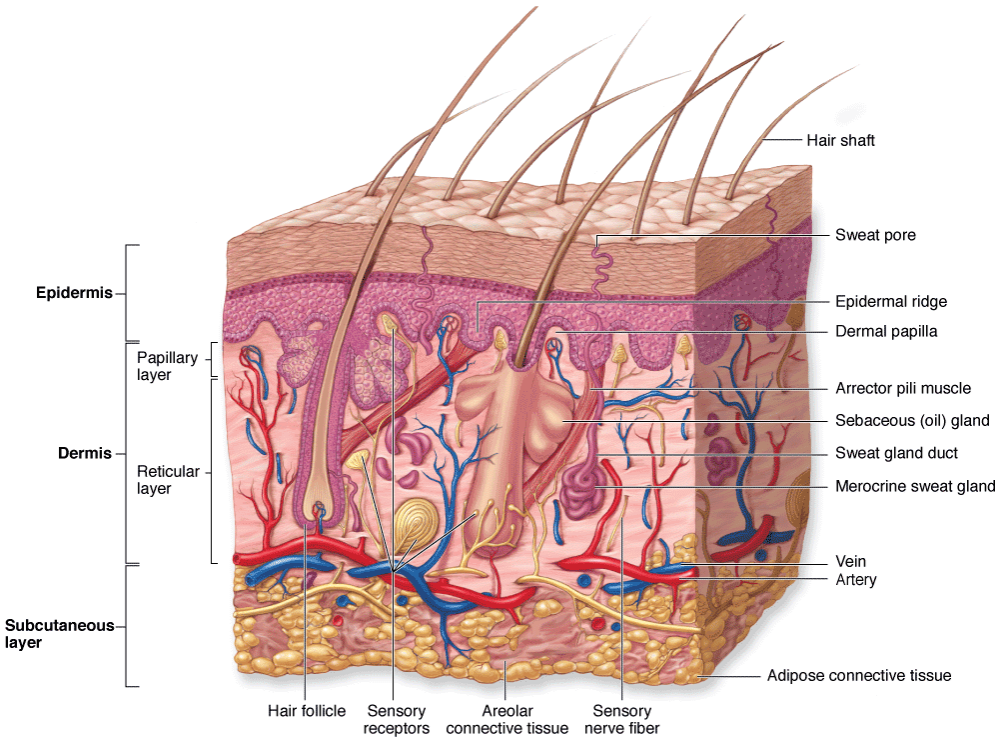

Figure 1.1 Cross-section of the human skin showing its multi-layered structure. Adapted from [1]

Skin, the largest organ of the human body, is formed by a highly stratified and multi-layered structure (Figure 1.1). The skin's primary role is to protect the internal organs from the external environment,[2-4] but it also performs a range of regulatory, perceptive, cosmetic and supplementary functions.[2] The skin is composed of three main layers: epidermis, dermis, and hypodermis.[5] The outer most layer of the epithelium, the epidermis, is responsible for the mechanical strength and physical protection of the skin, preventing moisture loss and pathogen entry.[6] This avascular layer is composed mainly of keratinocytes, but also contains other cell lines such as melanocytes and Langerhans cells.[2, 7] Beneath the epidermal layer is the dermis, this layer provides elasticity and mechanical integrity, besides a vascular plexus to nourish the integument. It consists of various glycosaminoglycans (GAGs), elastin and collagen, which compose the extracellular matrix (ECM).[8] Skin appendages, such as hair follicles, nail, sebaceous, sweat and apocrine glands can also be found in this layer.[9] The cellular components of the dermal layer include fibroblasts, endothelial cells, smooth muscle cells and mast cells.[10] Hypodermis, the most inner layer of the skin, is composed by loose fatty connective tissue.[11] Lipocytes and collagen present on this layer assist in the regulation of the body temperature and homeostasis.[10]

1.3 Skin components

1.3.1 Fibroblasts

Fibroblasts are a highly heterogeneous and dynamic cell lineage prevalent in the human dermis, which plays an important role in the healing process by maintaining the physical

integrity of connective tissue. Fibroblasts are remarkably plastic in nature and are capable of altering its function, physiology or transitioning into a new cell type such as myofibroblasts.[12] During the early stages of the healing process, fibroblasts occupy the provisional matrix composed of fibrin, fibrinogen and fibronectin, and proliferate in response to cytokines produced by neutrophils and macrophages that have migrated into the wound tissue. Then, a series of factors such as mechanical tension, cytokines and TGF-β drive the phenotypic change of fibroblasts to myofibroblasts. Myofibroblasts exhibit decreased proliferative capacity and increased deposition of the dense, fibrotic collagen matrix (comprising of collagen I, III, IV, and V) and wound contraction. During the remodelling phase, myofibroblasts produce decorin, which regulates collagen fibrillogenesis. Matrix breakdown promotes disassembly of cellular focal adhesions, the reduced ability of myofibroblasts to adhere to the matrix leads to cellular apoptosis, with the myofibroblasts apoptosis towards the end of the healing phase, a collagen-rich, hypocellular scar is formed.[13]

1.3.2 Keratinocytes

Keratinocytes are the main cellular component of the outermost layer of the skin, and function as a barrier against the outer environment.[13] Keratinocytes are involved in alterations in the cell-matrix adhesions and cell-cell junction that are crucial for wound closure and reepithelization.[14] Moreover, keratinocytes secrete ECM, growth factors and matrix metalloproteinases, which are key regulators of multiple aspects of tissue repair. Matrix metalloproteinases (MMPs) that are mostly deposited by keratinocytes are: MMP-1, MMP-7, MMP-9, and MMP-10. MMP-1 expression rises rapidly in response to injury and peaks in migrating basal keratinocytes at the wound margin at day 1 followed by a gradual decrease, until being undetectable when reepithelization is

completed.[13] Activation signals of several driving growth factors such as hepatocyte growth factor (HGF), fibroblast growth factor (FGF) and epidermal growth factor (EGF) by keratinocytes are also needed to induce reepithelialisation.[14] The production of transforming growth factor (TGF- β1 and - β3) by human keratinocytes is required to assist preventing excessive scar formation.[13]

1.3.3 Extracellular matrix

The extracellular matrix is a highly dynamic microenvironment that comprises the noncellular component present in tissues. The composition and properties of the ECM varies according to different tissues and physiological changes, such as aging and in response to injury.[15, 16] The ECM has many functions including: providing a physical scaffolding for cell attachment, acting as a reservoir of growth factors, providing signalling cues that are required to orchestrate cell function in tissue formation and homeostasis.[16, 17] This extracellular component of the skin can be divided into: proteoglycans (PGs) and GAGs (Table 1.1) which provide dynamic, and osmotically active properties of the ECM; and fibrous structural proteins such as collagens, and laminins, elastin and fibronectin which provide the core structure and tensile strength of the tissue, enable connection of the matrix components, and regulate cell function.[12, 15, 16]

Table 1.1 Glycosaminoglycans in human skin extracellular matrix.

Glycosaminoglycans	Main disaccharide unit	Ref.
Heparin	L-iduronic acid 2-sulfate (1→4) N-acetyl-D-glucosamine-2&6 sulfate	[18]
Heparan sulfate	β-D-glucuronic acid 2-sulfate (1→4) N-acetyl-D-glucosamine-2 sulfate	[19]

Chondroitin sulfate	β-D-glucuronic acid β (1→3) N-acetyl-D-galactosamine-4 sulfate	[20]
Dermatan sulfate	L-iduronic acid β-(1→4)/α (1→3) N-acetyl-D-galactosamine-4 sulfate	[21]
Hyaluronic acid	β-D-glucuronic acid β- (1→4)/(1→3) N-acetyl-D-glucosamine	[22]

Collagens are the most abundant fibrous proteins within a healthy ECM. Fibrillar collagens are present in the dermis as collagen type I and collagen type III, represents about 80% and 10% of the dermal ECM, respectively. These fibrillar proteins are organized into complex network of long-chain fibres, intermingled with bundles of elastic fibres and stabilized by the formation of covalent crosslinks, which is a mechanism fibronectin-dependant. These fibres provide the skin its mechanical resilience, tensile strength and structural support, as well as regulate cellular functions.[15] Abnormalities in genes that encode collagen are linked with several connective tissue diseases including skin disorders.[13] During the early stages of granulation tissue formation, myofibroblasts synthesise collagen III, which plays a regulatory role in the assembly of collagen fibrils and determination of the fibril diameter of collagen I.

In the early stages of the healing cascade, collagen III expression rises more than the collagen I expression, leading to an increased ratio of collagen I/III from 20% up to 50% collagen III. The collagen I/III ratio decreases to normal levels again during late stages of the healing cascade. Increased levels of collagen III relative to collagen I in the late stages of the healing process characterises an immature scar.[13] Abnormal levels or irregular ratio of types of collagens can affect cellular function apart from the

mechanical stress imposed by collagen fibrils, which directly affect the healing capacity of the tissue.[12] Collagen III-deficiency, for example, may lead to severe spontaneous skin wounds with non-uniform collagen fibrils,[13] promote myofibroblast differentiation and more noticeable wound contracture.[12]

Nonfibrillar collagens comprises collagen type IV, VI, VIII, and XIV. Instead of forming fibrils, nonfibrillar collagens forms reticular networks, that connect cells to the basement membrane, or support the structural organization of fibrillar collagens. Collagen IV is found in the basement membrane and promote keratinocyte and fibroblast migration and support cell adhesion to the basement membrane. Collagen VI assemblies anchor cells to the connective tissue and has demonstrated to inhibit fibroblast apoptosis. Collagen VII has demonstrated to play a role in dermal fibroblast migration and cytokine expression in wound-infiltrating macrophages. Collagen XIV, on the other hand, has shown to play a role in reducing dermal fibroblast differentiation and significantly down-regulating fibroblast DNA synthesis while keeping viability and cell number stable.[12]

Fibronectin is a glycoprotein assembled into a fibrillar network on the cell surface, it connects cells to collagen fibres by binding to integrin receptors in the ECM, which leads to modulation of the cell's cytoskeleton and enable cell migration. Upon tissue injury, fibronectin mediate homeostasis, and together with fibrin, provides temporary meshwork which helps to seal the wound and guide invading leukocytes and endothelial cell to the wound site. In the later stages of the healing cascade, fibronectin is synthesised by keratinocytes, endothelial, and dermal myofibroblasts and is found in the dermis and dermal–epidermal basement membrane.[13] Elastin are synthesised by fibroblasts and smooth muscle cells and found in skin and blood vessels. Elastin also

regulates various ECM processes, including the recoil and resilience of the skin. In mature skin, elastin comprises about 3–4% of the dry weight of tissue.[13]

1.4 Wound healing

The disruption of the skin triggers a highly coordinated series of interconnected events toward the restoration of the injured or lost tissue. The healing process involves an integrated action of multiple mediators such as ECM molecules, platelets, GF, inflammatory cells, cytokines, and chemokines; throughout the sequential, yet overlapping phases of haemostasis, inflammation, migration, proliferation, and remodelling (Figure 1.2).[4] The first stage of wound healing starts immediately after injury occurs.[23] It begins with vasoconstriction of damaged vessels, which is caused by the activity of vasoconstriction factors such as serotonin, thromboxane A2.[24] Following, the clotting cascade is activated by extrinsic and intrinsic pathways. Fibrin along with platelets form a temporary network protecting the structural integrity of vessels, preventing pathogens from coming in,[25] as well as forming a pathway to aid cell migration. Platelets are early modulators of the healing process. When injury occur, the platelets in the blood get activated, adhering and releasing numerous proteins, GFs and cytokines in the injured site, such as platelet derived growth factor (PDGF), transforming growth factor (TGF-α, TGF-β), basic fibroblast growth factor (bFGF), insulin-like growth factor 1 (IGF-1), and vascular endothelial growth factor (VEGF). PDGF is an important growth factor for tissue regeneration, with numerous functions such as being a chemoattractant for neutrophils and macrophages.[26]

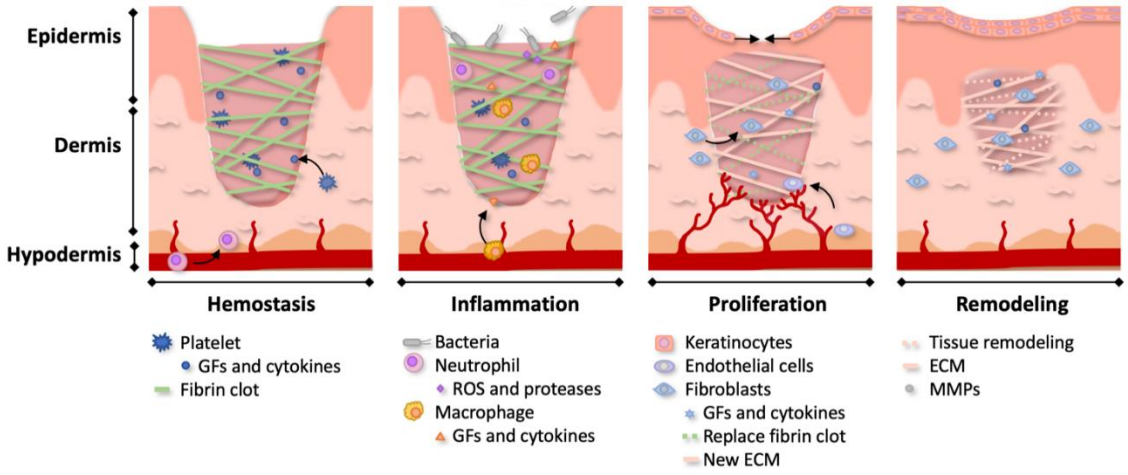

Figure 1.2 Schematic representation of the different stages of the wound healing process.

The typical wound healing process can be sectioned into four overlapping phases hemostasis, inflammation, proliferation and remodelling. Each phase is dominated by different types of cells responsible for distinct cellular events. The cellular activities are regulated by various growth factors and cytokines secreted by the cells; MMPs: matrix metalloproteinases; and ECM: extracellular matrix components.

After bleeding is under control and a barrier is secured, the subsequent inflammation phase starts. The predominant cells in this phase are phagocytic cells, such as neutrophils and macrophages.[27] The previous constricted vessel now expands and the permeability of its walls are increased, facilitating the migration of cells to the wound area.[28] Neutrophils are recruited by chemotactic factors like thrombin, products of fibrin decomposition, bacteria, complement (C5a) components, histamine, prostaglandin E2 (PGE2), leukotrienes, TGF-β, and PDGF.[26] These cells are the first to arrive in the wound area and are the first line of defence against infection phagocytising and killing pathogens by releasing proteases and ROS.[29] After 2-3 days in the wound area, neutrophils are depleted and replaced by monocytes.[23] Macrophages are very important cells for the healing process because they not only participate in the phagocytosis process of killing bacteria and removing debris, but also are the major

source of GFs and cytokines stimulating the proliferation of fibroblasts and collagen synthesis. [24]

At this stage, the process of rebuilding the damaged tissue is intensified by the migration and proliferation of fibroblasts, endothelial cells, and keratinocytes. These cells release mediators that modulate the granulation tissue formation, epithelialization, and angiogenesis.[30] The temporary fibrin network is replaced by granulation tissue, which consists of collagen (mainly type I and III), elastin, proteoglycans, glycosaminoglycan, and non-collagen proteins. These cells are synthetized mainly by fibroblasts whose activity is regulated by PDGF and TGF-β. Epithelialization, a multiphase process to reconstruct the epithelium after the injury, comprises of cellular detachment, migration, proliferation, and differentiation. Angiogenesis restores the development of ischemic necrosis simultaneously stimulating the tissue repair process. Endothelial cells migrate and create a network branching into tubular structure beginning the new blood vessel loop. When tissue is replaced by collagen matrix and later by scar, the oxygen influx and nutrients decrease significantly. Angiogenesis is halted and part of the capillaries disintegrate during apoptosis.[31]

During the last phase of the healing process the granulation tissue matures to form a scar. The maturation process of the granulation tissue comprises the reduction of capillary amounts by aggregating into bigger blood vessels, lowering the content of glycosaminoglycans and proteoglycans. Cell density and metabolic activity of the tissue are also lowered. The proportion of collagen changes (type III collagen content is converted to collagen type I), the total collagen content increases and its spatial organization rearrange, forming more covalent cross-links, which leads to increased tensile strength of the tissue. This stage can last months to years and the new tissue

could reach from 50-80% of the some of its original healthy functions, depending on the severity of the initial wound.[31]

1.5 Scar formation

Normal scar formation is the body's natural response to tissue injury and does not develop until after the wound has completely healed. During the healing process, dermal ECM composition is remodelled - dense ECM network comprised mostly of collagen gradually replace the original loose and hydrated ECM. A visible scar will be formed if a wound takes more than 3-4 weeks to be re-epithelialized. The scar tissue loses its original strength and functionality as there will be less blood vessels, which will limit its blood irrigation, and denser ECM network will make the tissue less tolerant to shape change. Impaired wound healing and abnormal scar formation is a huge cause of morbidity as cosmetic/function impairment, and mobility limitation due to scar contraction and pain, deeply affect the patient quality of life. Scar tissue exhibit disturbance of the alignment of collagen fibres - collagen fibres are aligned in a single direction parallel to the skin, differently from healthy skin where collagen fibres are organised in a random basket weave pattern. Scar tissue is formed by the same ECM molecules as the tissue they replace, however, the levels of those molecules are altered in scar tissue, for example, dermal scar tissue displays higher levels of collagen I and III, fibronectin, and laminin.[13]

Scars can be classified according to their clinical behaviour and physical aspects. Atrophic scars are characterised by an indented recess of the skin due to loss of underlying supportive structure like muscle or fat, and it is often a result of severe acne or chickenpox. Hypertrophic scars are characterised by the excessive deposition and

alterations of collagen and other ECM proteins, which gives the skin raised and often red appearance. It is often developed post thermal or traumatic injury. Keloids are also raised and red in appearance, but differently than hypertrophic scars, it grows outside the original wound area. Keloid scars are characterised by the excessive deposition of collagen and high ratio of collagen I/III – (about 17:1) compared to normal scars (about 6:1), which may be a result of high proliferative activity of keloid fibroblasts.[13] Figure 1.3 shows the histological assessment of scars highlighting the epidermal abnormalities in different scars.

Differently from the adult skin wound healing process that involves fibrosis and scarring, foetal wound healing is able to fully regenerate the skin and restore the normal ECM architecture, strength and function, resulting in a scarless phenotype. Even though the mechanism of the foetal healing is still unknown, studies have reported different inflammatory response, cellular mediators, cytokines, growth factors, and ECM modulators and structures between postnatal and foetal wound repair.[13] Key differences in the foetal healing process that may influence its remarkable regeneration ability are the concentration of collagen I and III, and the ratio of collagen III/I. It has been reported that foetal ECM is rich in collagen III and hyaluronic acid (HA), and even though collagen I is the major ECM component, like in adult skin, the total amount of collagen I is lower in foetal skin compared to adult skin. The ratio of collagen III/I in foetal skin is also higher, having collagen III comprising 30–60% of the total collagen compared to 10–20% in adult skin.[13]

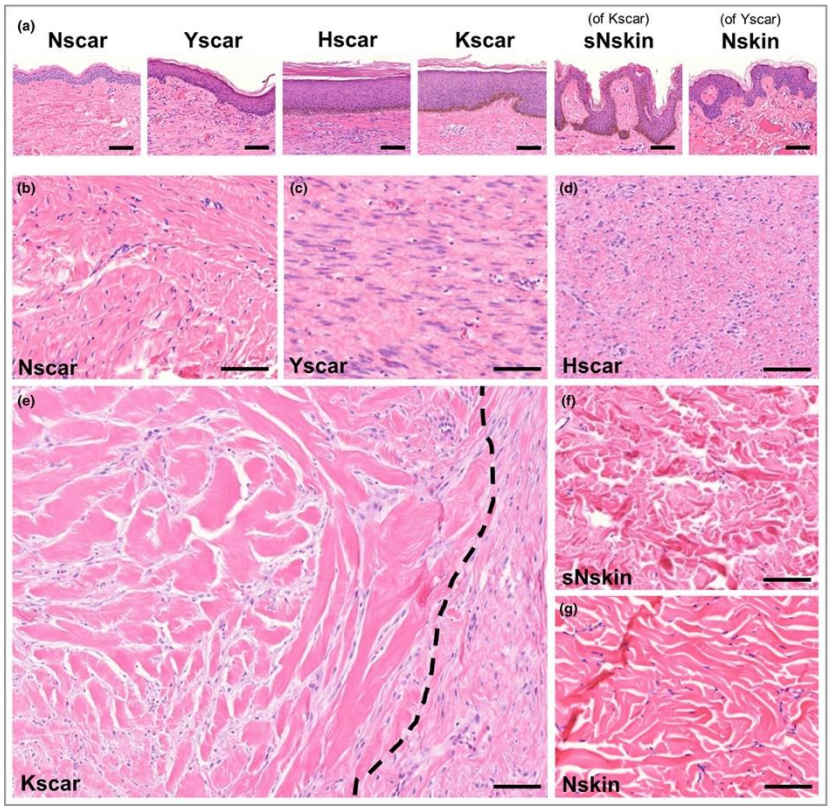

Figure 1.3 Histological assessment of scars.

Haematoxylin and eosin staining images of (a) Epidermis, (b–g) Dermis of (b) normotrophic scar (Nscar), (c) young immature scar (Yscar) with (g) adjacent normal skin (Nskin), (d) hypertrophic scar (Hscar), and (e) keloid scar (Kscar) with (f) surrounding-normal-skin (sNskin). Scale bar = 100 μm. The dashed line in (e) indicates the border between 'keloidal collagen' (left) and normal scar dermis (right). [32]

1.6 Cutaneous wounds

As the skin is permanently exposed to the external atmosphere, it is constantly susceptible to mechanical and chemical insults.[33] According to the Wound Healing Society, a wound can be described as the result of disruption of normal anatomic structure and function of the skin.[34] Wounds can be sorted into various categories.[35] Based on their time frame of healing, wounds can be clinically classified as acute and chronic. Acute wounds normally proceed by following a timely and orderly

healing cascade of haemostasis, inflammation, migration, proliferation, and remodelling, achieving functional and anatomical restoration of the skin, with minimal scarring.[35] Completely healing within the expected healing time frame of 8 to 12 weeks.[36] The primary causes of acute wounds include: abrasions; penetrating caused by knives, gun shots and surgical incisions; as well as burns, chemicals and thermal sources.[37]

Complex wounds, or hard-to-heal wounds, is a term used to describe wounds that may involve multiple tissues, where healing is prolonged/disrupted or fails completely, often complicated by comorbidities or infection.[38] Impaired wound healing and abnormal scar formation is a significant cause of morbidity as cosmetic/function impairment, and mobility limitation deeply affect the patient quality of life.[13] Chronic wounds do not follow the conventional stages of healing in an orderly and timely manner[27] remaining open for more than 12 weeks and/or often reoccurring.[39] Chronic wounds can be classified as diabetic ulcers; venous and arterial ulcers; and pressure ulcers.[40] Despite differences in ethology at the molecular level, chronic wounds share lack of balance between pro- and anti-inflammatory factors such as cytokines, growth factors (GF), proteases, and metabolically competent leading to excessive and prolonged inflammation, persistent infections, and the inability of dermal and/or epidermal cells to respond to reparative stimuli.[41] For this reason, it is important to re-establish the balance of cytokines, GF, proteases, and metabolically competent cells in order to restore the skin healing ability.[27]

Burn injury is a significant cause of morbidity and mortality related to the depth and surface area of the skin involved.[42] Due to the disruption of the barrier integrity, the risk of systemic infections in burn patients is high, which accounts for most of the

associated death. To improve patient outcome, covering the wound in a timely manner is key to reducing infection and to restoring the barrier function. Historically the drive for a tissue engineered solution was the need to repair the skin in massive burn injuries. The use of laboratory based tissue expansion in the form of cultured epithelial autografts (CEAs) was first clinically used in 1982.[43] Further development has been made by shortening the lengthy time needed for the preparation of CEAs through delivering autologous cell suspension using a spray system.[43-46] However, for full-thickness burns, the healing is less ideal as CEAs address only the epidermal repair. The development of dermal scaffolds has facilitated in situ tissue guided regeneration of the dermal elements to repair full-thickness wounds when the donor sites for traditional skin grafts are compromised.[42, 47]

1.7 Current strategies for skin regeneration

The treatment of cutaneous wounds is a critical issue in healthcare, requiring deep understanding of several factors affecting the healing process, such as the wound cause or type (burn, ulcer, acute and chronic wound), the wound depth (which can be classified as epidermal, superficial partial-thickness, deep partial-thickness and full-thickness wounds), the patient's health condition like diabetes and persistent infections, as well as the level of the exudate.[4, 26] One of the main goals and biggest challenges of current skin wound treatments is to stimulate fast wound closure coupled with optimal aesthetics and functional regeneration.[48] To date, a great variety of wound care products are available for the treatment of different types of skin wounds. Table 1.2 summaries some of the current and emerging strategies available for treating skin wounds.

Table 1.2 Current and emerging strategies for the treatment of skin wounds. Adapted from [4]

Treatment	Advantages	Limitations
Autografts	'Golden standard' in skin regeneration; good adhesion to the wound bed; provides pain relief; reduced rejection	Limited availability of donor sites; induce scar formation; patient morbidity; lengthy hospital stays
Allografts	Temporary prevention of wound dehydration and contamination; incorporate into deep wounds	Limited availability; may lead to immune rejection; transmission of diseases
Creams, solutions, and ointments	Ease of use; provide disinfection, cleaning, and debridement; not expensive in general	Limited skin regeneration; short residence time on the wound (require frequent administrations)
Traditional dressings	Not expensive; provide a protective barrier against the penetration of exogenous microbes	High absorption capacity; do not provide a moist environment; adhere to the wound bed; may inhibit the healing process
Modern dressings	Create and maintain a moist wound environment; can be made from a wide range of materials with different properties; ability to hydrate the wound and remove excess exudate	More expensive; low adhesion to the wound bed; inability to promote the regeneration of lost skin, in particular the dermal layer
Tissue-engineered skin substitutes	Promote the regeneration of dermis and epidermis; prevent fluid loss and provide protection from contamination; may deliver extracellular matrix components, cytokines, growth factors and drugs to the wound bed, enhancing the healing process; can be used in combination with autografts	High manufacturing costs; difficult handling; poor adhesion to the wound bed; possibility of immune rejection and transmission of diseases (allogeneic skin cells); inability to promote the regeneration of full-thickness wounds; poor vascularization; impossibility of reproducing skin appendages

Complex wounds are incapable of steering cellular events toward tissue regeneration and healing; therefore, they require skin substitutes to address these limitations. Traditional skin grafts including autografts, allografts and xenografts face significant limitations regarding availability, safety, and risks of morbidity.[49] For instance, autologous skin grafts include split-thickness skin graft (STSG) and full-thickness skin graft (FTSG). STSG, which contain the epidermal compartment plus a portion of the dermal compartment, are used in the treatment of extensive injures, and full-thickness burns. The main drawback of this type of graft is the poor cosmetic outcome with significant scarring and lack of adnexal structures.[50] FTSG, which contain the epidermal, dermal and subcutaneous compartments are the gold standard procedure in

cutaneous reconstruction and wound coverage. However, these grafts also have intrinsic and extrinsic limitations such as limited donor site availability, limited expansion capability and limited graft survival.[51] These issues are especially prominent when a large piece of skin graft is needed, which drives the development of skin tissue engineering and synthetic skin substitutes.

Skin regeneration via transplantation of cellular skin substitutes, using autologous or allogenic cells, has shown a broad variety of outcomes for temporary or permanent wound coverage.[52] Its therapeutical effect relies on the ability of cells to self-assemble to form a neo-tissue, and in the production of signalling molecules and ECM to promote healing.[43] Traditional cell therapies involves the combination of fibroblast and/or keratinocytes with biodegradable scaffolds, or fluid solutions for manual delivery of cells.[43] For example, Apligraf® is composed by a type I collagen-based dermal matrix populated with allogenic fibroblasts and an epidermal compartment composed of top-seeded keratinocytes.[53] DermaGraft® is a polyglactin-910 or polyglycolic acid-based dermal matrix populated with human foreskin fibroblasts.[54] EpiCel is a sheet of cultured keratinocytes, from an autologous source.[43] ReCell is cell suspention spray which contains a mixed population of cells such as keratinocytes, fibroblasts, Langerhans cells and melanocytes.[55, 56] Limitations of these traditional therapies include poor durability, inability to reproduce skin appendages,[57] and lack of spatiotemporal control in cell delivery to form skin-mimicking layered structures.[58, 59] For this reason, traditional wound care and closure products are being increasingly replaced by more advanced wound treatments. Attempts to decrease the length of stays at acute care hospitals to reduce surgical healthcare costs and the rising inclination

towards products that enhance therapeutic outcomes are driving the demand for state-of the-art wound care and closure products.[4]

Growth factors are soluble proteins capable of modulating a variety of cellular events important for the healing process.[60] Deficiency of various growth factors have been reported in chronic wounds and imparted wounds, including reduced levels of TGF-β, EGF, FGF, VEGF, and PDGF.[61] Commercially available growth factors-based preparations for external use includes: Becaplermin, recombinant human PDGF for treatment of DFUs;[62-64] recombinant human bFGF for treatment of burn wounds and diabetic leg ulcers;[65] as well as recombinant human EGF for treatment of DFUs.[66-69] Although topical administration of human-recombinant growth factors has been approved for clinical use, reported studies have shown conflicting evidences on the efficacy of topical growth factor in improving healing.[70] Some of the factors that could be limiting the therapeutical efficacy of growth factors includes low stability, rapid elimination by exudation in the wound bed, high degradation rate[61] or failure to provide enough stimulus to initiate the complex cascade of the healing process.[71] In order to improve the effectiveness of growth factors therapies, several growth factor delivery systems have been proposed for the treatment of acute and chronic wounds.

1.8 Compelling needs for advanced wound healing products

Wounds, more specifically chronic wounds, are recognised as a silent epidemic as they have been a major contributor to mortality, morbidity and permanent disability worldwide.[72] The increase in the aging population coupled with prevalence of lifestyle diseases and chronic wounds; increase of complex surgical procedures and introduction of government initiatives to decrease lengths of hospital stays are some of

the factors driving the demand of the advanced wound care market. The global wound closure and advanced wound care management market is estimated to reach $26 million by 2026.[73] The global tissue engineered skin substitutes market is valued around $131 billion (2020) and is estimated to reach $335 billion by 2025.[74] Burn is one of the leading causes of non-intentional death/injury worldwide with an estimated of 180,000 deaths every year,[75] in the United States alone with an estimated of 40,000 hospitalizations related acute burn injuries occurred in United States in 2016.[76] A retrospective analysis of the national health insurance program in the United States 5% dataset (2014) showed that in the US, about 8.2 million patients presented at least one type of wound/related infection in 2014, and the treatment cost was conservatively estimated in about $32 billion.[77] In Australia, the precise health and economic burden of wounds is unknown, however, it has been estimated that about 400,000 hospitalizations and residential care settings occur in Australia each year. From those cases, pressure wounds represent 84%, venous leg ulcers (VLUs) 12%, diabetic foot ulcers (DFUs) (3%) and arterial insufficiency ulcers (1%). General wound treatment costs was estimated in about AUD$3 billion a year, which represents approximately 2% of the Australian national healthcare expenditure.[78]

1.9 Bioprinting technology

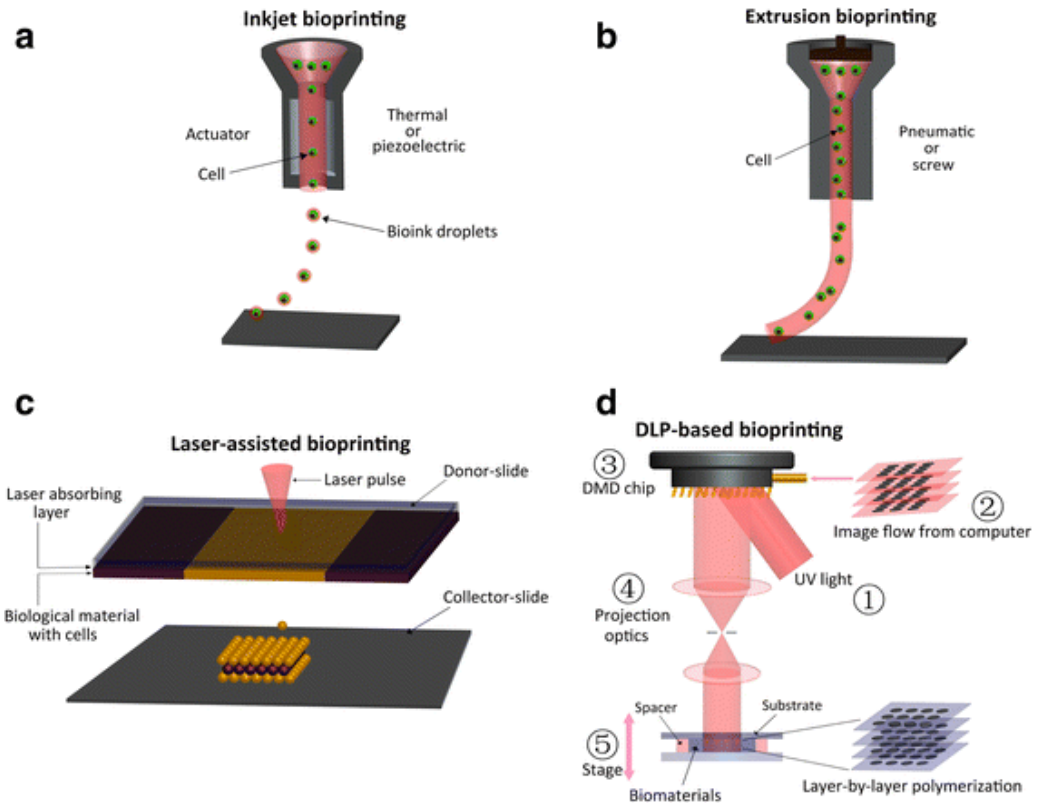

Figure 1.4 Schematic illustration of 3D bioprinting capabilities reported for skin bioprinting.

(a) Inkjet bioprinting: the ejection of bioink droplets is controlled by either a thermal or piezoelectric actuator where pressure pulses are generated to regulate the valve-opening time. (b) Extrusion bioprinting: driven by either pneumatic pressure, or an advancing piston or screw, highly viscous bioinks are extruded in the form of continuous filaments into direct contact with the substrate. (c) Laser-assisted bioprinting: a laser provides the driving force to propel the cell-laden bioink onto a collector platform. (d) Digital light processing-based bioprinting: the photosensitive polymer precursor in a container is cured layer-by-layer by projected and patterned UV and/or visible light generated by a digital micromirror device.[79]

Tissue engineering is an interdisciplinary field which applies principles and technologies in engineering, materials science, cell biology, and biomedicine to restore,

maintain, or improve biological tissues.[80] One of the tissue engineering approaches for wound healing application involves the development of functional yet biocompatible three-dimensional (3D) skin substitutes consisting of biomaterials and living cells to support and guide the regeneration of injured or lost tissue.[80] Tissue engineering techniques including bioprinting, photolithography, and electrospinning[81] have been proposed to overcome existing limitations of traditional skin wound treatments.[11] Among them, bioprinting is rapidly emerging as a promising technique for precise spatial manipulation of living cells, bioactive molecules and functional components, with the potential to mimic the complex physiological microenvironment of tissues and organs.[81]

Bioprinting is an additive manufacturing technique based on computer-aided-design (CAD), wherein living cells and biomaterials are dispensed in a temporal and spatial controlled fashion.[6] A complex 3D microenvironment can be fabricated by using a bioprinting approach, in which the cells can be encapsulated into hydrogel to mimic natural ECM of a specific tissue; thereby overcoming various limitations faced in tissue engineering and regenerative medicine.[6] Common bioprinting strategies used to produce tissue scaffolds include inkjet printing, extrusion printing and laser-assisted bioprinting.[81] In this thesis, extrusion-based bioprinting will be further described, as this was the method chosen for the fabrication of tissue-like structure, which will be presented in the following chapters.

1.9.1 Extrusion Bioprinting

Extrusion-based bioprinting has become one of the most widely used bioprinting platform due its great versatility and feasibility in the fabrication of scaffolds for tissue

engineering. Some of the advantages of this method are its relatively low cost; capacity to dispense a wide array of biomaterials and cells; ability to dispense viscous inks (30 mPa s^{-1} to > 60 kPa s^{-1}) with high cell density; and fast deposition speed, which is often used to produce large-scale scaffolds. By using extrusion-based bioprinting platforms, tissue scaffolds can be developed with biological and mechanical properties appropriate for the restoration of damaged-tissue.[80] Extrusion-based bioprinting platform is composed of a fluid-dispensing head (or multiple fluid-dispensing heads) and an automated robotic system. During bioprinting, the dispensing head is moved along X-Y-Z axes depositing cylindrical filaments of desired 3D designed model layer-by-layer. This rapid fabrication technique provides better structural integrity due to the continuous deposition of filaments.[82] Extrusion-based methods can be classified into three categories: pneumatic, piston, and screw-based bioprinting. In piston- or screw-based systems, the ink is mechanically pushed by a linear moving piston or a rotating screw-driven configuration.[80] Pneumatic-based bioprinting utilizes pneumatic pressure to extrude the ink from the nozzle at a controllable volume and flow rate. The deposition accuracy highly dependent on the flow properties of the ink and can be significantly affected by the viscosity of the ink solution.[83]

1.9.2 Bioinks

Hydrogel-based bioinks which can encapsulate living cells and bioactive molecules are commonly used for bioprinting process (Figure 1.5).[81] The hydrogels used for tissue engineering application are predominantly from natural biopolymers. High water content hydrogels provide an optimal environment for incorporation of cells and bioactive molecules, because they can provide an instructive, aqueous 3D matrix, mimicking the native ECM. The chemical signals present in these hydrogels, lead to

high cell viability and proliferation rates.[84] Understanding the performance of materials is necessary for developing bioink formulation. The basic properties of an optimal biomaterial for tissue regeneration are biocompatibility with the target tissue; biodegradability rate compatible with native ECM; non-cytotoxicity; and non-immunogenicity.[11] In addition to these intrinsic biological properties, it is extremely important to assess the physicochemical properties of the hydrogel ink to determine its suitability for printing under the conditions imparted by the chosen biofabrication approach. The main parameters that determine the suitability of a hydrogel ink includes rheological behaviour and crosslinking mechanisms.[84] A common way to improve printability of hydrogels is by modulating the polymer concentration or crosslink density.[85]

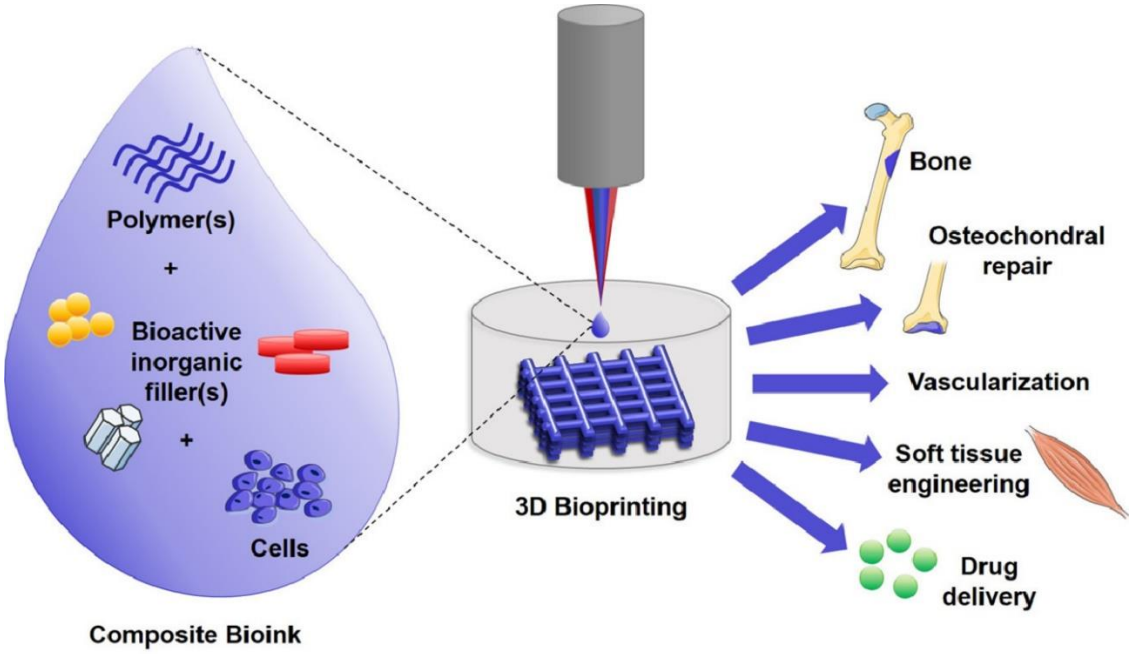

Figure 1.5 Schematic representation of a bioink components.[86]

1.9.3 Crosslinking Mechanisms for Hydrogels

The gelation achieved through different crosslinking mechanism is used to hold the structural shape of a printed hydrogels. The crosslinking can either be physical, chemical, forming of covalent chemical bonds, or combination of both processes. Physical crosslinking mechanisms rely on non-chemical interactions of high molecular polymer chains, such as ionic interactions, hydrogen bonds, or hydrophobic interactions. Chemical crosslinking mechanisms forms hydrogels through irreversible covalent bonds, which can provide high mechanical strength to the printed construct.[84] Table 1.3 adapted from Malda et al. summarizes the crosslinking strategies and compares their advantages and disadvantages.

Table 1.3 Crosslinking strategies for biofabrication. Adapted from[84]

Crosslinking strategies		**Advantages**	**Disadvantages**
Physical	**Ionic**	Reversible interactions ensure constant viscosity during printing, Excellent compatibility with biological systems.	Requires additional crosslinking agent and/or post-processing crosslinking, Mechanically weak constructs,
	Stereo complex	Reversible interactions ensure constant viscosity during printing, Excellent compatibility with biological systems.	Relatively slow gelation, Relatively high viscosity of the building blocks Requires additional crosslinking agent and/or post-processing crosslinking Mechanically weak constructs
Chemical	**Thermal**	Reversible interactions ensure constant viscosity during printing Rapid reassembly to gels after printing Excellent compatibility with biological systems	Requires post-processing crosslinking
	UV	Polymerisation through irradiation during printing does not affect viscosity during printing in the nozzle Allows for post-processing crosslinking (stabilization) of mechanically weak physically crosslinked hydrogel constructs	High reaction rates necessary as polymerisation needs to be completed between nozzle and deposition May involve exposure of constructs to irradiation
	Wet chemical	No need for irradiation or other further stabilization - Mechanically stable constructs	Irradiation may affect embedded cells May require (potentially harmful) crosslinking agent A trigger for chemical reactivity with required stringent control

			of crosslinking kinetics is needed to avoid viscosity change in the nozzle throughout printing time but ensure crosslinking between nozzle and deposition

Physical crosslinking is the most prominent method used to produce crosslinked hydrogels through biofabrication processes,[87] because of its excellent compatibility with fragile molecules and with living cells. Physical crosslinking forms non-covalent interactions between hydrophilic polymer chains preventing hydrogel dissolution in an aqueous environment.[84] The major drawback of physically crosslinked hydrogels is their poor mechanical properties, which may cause instability, difficulties in handling and poor overall performance. For this reason, increasing attention has been driven to hydrogels which can be pre-crosslinked prior to printing allowing better filament deposition, and chemically crosslinked after printing by exposure to radiation or post-processing reaction of complementary chemical groups to fixate and stabilize the printed structure.[84]

1.9.4 Biomaterials

Material selection is one of the most important steps of the tissue scaffold biofabrication because they provide a structural interface required for interaction between ECM, cell and growth factors.[88] Synthetic polymers commonly used in bioink formulations include polyethylene glycol (PEG)[89], pluronic[90], poly(vinyl pyrrolidone) (PVP)[91] and polycaprolactone (PCL)[92]. Materials modified to include cell-instructive molecular motifs are promising candidates with the ability to tailor cell-material interactions. For example, Lutolf et al. engineered cell-responsive PEG hydrogels that contain specific amino acid sequences cleavable by MMP. Human foreskin fibroblasts

were shown to be able to breakdown and remodel the densely crosslinked PEG network as a result of the enzymatic activity of secreted MMP.[93]

Naturally derived materials include collagen, gelatin, albumin, thrombin, fibrinogen; polysaccharides such as chitosan, chitin, cellulose, and etc (Table 1.4).[11] These natural biopolymers are being widely used for tissue engineering application because of their similarities to the ECM, biological characteristics and inherent cellular interaction. However, inadequate mechanical properties or poor processability of currently available biopolymers are limiting their application to a certain extend.[88] Therefore, improvements on the properties of biopolymers, composites with natural and synthetic materials, and discovery of new biomaterials are needed to increase the available materials for biomedical applications. Table 1.4 summarizes examples of the recent bioinks used for bioprinting as related to skin regeneration. The range of bioinks for inkjet printing is limited due to the low viscosity requirements. Here, GelMA and growth factor-rich biomaterials will be further discussed as these biomaterials were used in bioink formulations in the following chapters.

Table 1.4 Review of biomaterials used as bioink components for 3D printing of skin-like structures.

Biomaterial components	**Printing**	**Cells**	**Ref**
Collagen I	Inkjet	HDFa / HEKa	[94]
Collagen	Inkjet	HDFn / HaCaT	[95]
PEG-based BioInk	Inkjet	HDF / HEK	[96]
D: collagen E: PVP-based bioink	Inkjet	HDF / HEK / HEM	[91]
Collagen I	Inkjet	HDFn / HEKn / HEMn	[97]
Fibrinogen/collagen I	Inkjet	AFS / BM-MSC	[59]
fibrinogen/collagen I; plasma thrombin	Inkjet	HDF / HEK	[58]
Chitosan/PEG	Inkjet	HDFn	[98]
Collagen I	Laser-assisted	NIH3T3 / HaCaT	[99]
Collagen	Laser-assisted	NIH3T3 / HaCaT	[100]
Human plasma containing fibrinogen	Extrusion	HDF / HEK	[101]

Gelatin/chitosan	Extrusion	HDFn	[102]
Alginate/gelatin	Extrusion	HDF	[103]
Gelatin/alginate/fibrinogen	Extrusion	NIH3T3/GFP / HEK	[104]
Chitosan/D-(+)raffinose pentahydrate	Extrusion	HDF / HaCaT (seeded)	[105]
GeMA/collagen, tyrosinase-doped	Extrusion	HDF / HaCaT / HEM	[106]
Silk fibroin/gelatin	Extrusion	HDF / HEKa	[107]
Pectin methacrylate/peptide RGD	Extrusion	HDFn	[108]
Human platelet lysate/GelMA	Extrusion	HDF	[109]
Ulvan methacrylate/gelatin	Extrusion	HDF	[110]
Ulvan methacrylate/GelMA/gelatin	Extrusion	HDF	[111]
Alginate/honey	Extrusion	NIH3T3	[112]
Decellularized dermis/alginate	Extrusion	NIH3T3	[113]
Collagen I/PCL mesh	D: Extrusion E: Inkjet	HDF / HEK	[114]
D: skin-dECM/fibrinogen HD: adipose-dECM/fibrinogen V: Gelatin, glycerol/thrombin	D: Extrusion E: Inkjet	HDF / HEK / HUVEC / HPAd	[115]
dECM	D: Extrusion E: Inkjet	HDFn / HEKn / ADMSC / hEPC	[116]
D: Gelatin/fibrinogen/collagen I/elastin BM: Laminin/entactin	D: Extrusion E: Inkjet BM: Inkjet	HDFn / HEKn	[117]
D: Collagen E: Culture medium	Inkjet	HDF / HEK / hEC / hPC-PL	[118]
Silk fibroin/4-arm PEG	DLP	NIH3T3 / HEK	[119]
GelMA/HA-NB	DLP	HDF / HUVEC	[120]

Note: D: Dermal compartment; E: Epidermal compartment; BM: Basement membrane; HD: Hypodermal compartment; and V: Vascular compartment. DLP: Digital light processing. HDF: Primary human dermal fibroblasts (a:adult/n:neonatal); HEK: Primary human epidermal keratinocytes (a:adult/n:neonatal); HaCaT: Immortalized human keratinocytes; NIH3T3: Immortalized non-tumorigenic murine fibroblast; HEM: Human epidermal melanocytes (n:neonatal); AFS: Amniotic fluid-derived stem cells; HPAd: Human preadipocytes; HUVEC: Human umbilical vein endothelial cells; BM-MSC: Bone marrow-derived mesenchymal stem cells; ADMSC: Adipose-derived mesenchymal stem cells. hEPCs: Human endothelial progenitor cells; EC: Human endothelial cells; hPC-PL: Human pericytes from placenta.

1.9.4.1 Gelatin methacryloyl (GelMA)

GelMA is a denatured type of collagen that has been widely used as a versatile matrix for tissue engineering scaffolds.[121-124] GelMA's inherent thermo-responsive characteristics and pseudoplastic behaviour facilitate filament deposition during the extrusion process and reduce nozzle-clogging,[125] whilst protecting cells against excessive shear stress.[126] Moreover, its photo-crosslinkable methacryloyl groups

enable irreversible shape fixation of the final printed construct.[127] GelMA hydrogels exhibit remarkable tunable physical and chemical properties, which makes them ideal candidate for skin tissue printing.[124] Several GelMA bioinks composites have been proposed for skin bioprinting. For example, Shi et al. describe a bioink composite made of GelMA and collagen doped with tyrosinase for the 3D bioprinting of living skin tissues.[106] Zhou et al. reported a bioink composite (GelMA/HA-NB/LAP) to print functional living skin tissue using digital light processing (DLP)-based 3D printing technology.[120] Even though it has proven to be a promising material for regenerative medicine and tissue engineering application, GelMA faces similar drawbacks to collagen as lacking mechanical strength and being subject to fast degradation. A general strategy to overcome these drawbacks is to make use of a secondary material without much elevation in the mechanical stiffness.

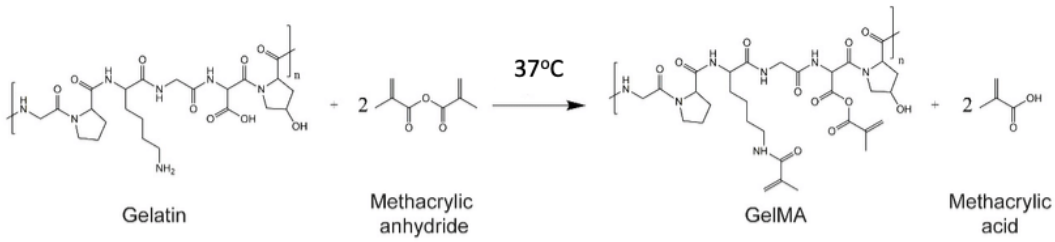

Figure 1.6 Gelatin methacryloyl (GelMA) synthesis reaction. Adapted from [128]

1.9.4.2 Growth factor-rich biomaterials

This category includes platelet bioproducts, such as platelet-rich plasma and platelet lysate. Platelet bioproducts are growth factor-rich serums derived from human platelets. Platelet bioproducts are a cost-effective source of growth factors containing high concentration of several relevant factors in wound healing, including PDGF, bFGF, VEGF and TGF-β.[129, 130] They can be obtained from an autologous source for

application in personalized medicine. Autologous platelet derived products present reduced risk of adverse immune reactions, but the volume of product produced from an autologous material may not be enough for clinical application, moreover, issues related to lack of standardization, and growth factor heterogeneity may lead to variations in the therapeutic efficacy. On the other hand, allogenic platelet derived products can be pooled to reduce individual donor variation. It can be automatized and standardized for production in large scale, however, it has higher risk of contamination and immune reaction.[71, 131, 132]

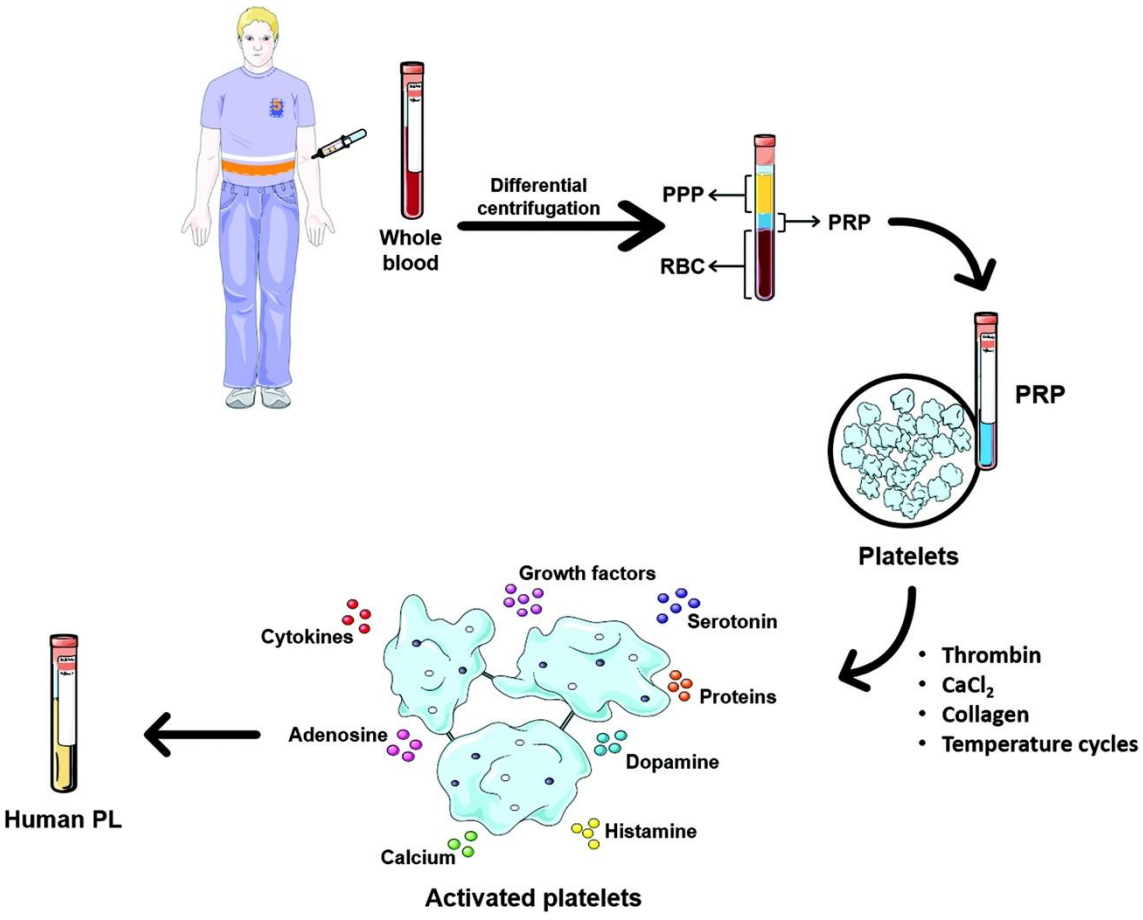

Figure 1.7 Schematic representation showing the PL preparation
from whole blood collection, activation/lysis of the platelets, and release of cytokines or growth factors. PRP, platelet-rich plasma; PL, platelet lysate.[133]

The therapeutical integration of 3D printing and growth factors have shown improvement in the manufacturing speed process for personalized approach, enable spatial dictation and controlled release of growth factors.[134] Xiong et al. reported the incorporation of FGF-2 into printed gelatin-sulfonated silk composite scaffold. FGF-2 shown to support re-epithelialization and promote expression of blood vessel related proteins such as smooth muscle alpha-actin (α-SMA) and CD31 *in vivo*.[52] Moreover, Wan et al. demonstrated that silver and PDGF-ββ co-loaded 3D printed scaffolds improved *in vivo* re-epithelialization, granulation tissue formation and angiogenesis in type II diabetic mice.[135] Intrinsic characteristics of the delivery vehicle material also heavily influence the release kinetic of growth factors. For this reason, material whose affinity with growth factors, and tuneable mechanical, physical, degradation properties are preferred.[120] Novel 3D printing strategies for controlled and smart release of biologically relevant factors in a spatiotemporal fashion may provide more effective and safe alternatives as well as great benefits to patients in the near future.

1.10 Electrofluidic approach

With increasing complexity of surgical procedures, appropriate post-operative wound management is crucial to prevent complications and achieve the best aesthetical and functional healing possible. Therefore, in addition to the hydrogel-based delivery system introduced earlier, it is also of interest to explore an electrofluidic approach using surgical sutures for post-surgical wounds. Thread and textiles have recently gained considerable attention as low-cost substrates for microfluidics and biosensor applications, based upon their mechanical strength and the ability to facilitate and direct fluid movement. Fluid flow in threads arise from wicking processes as a result of capillary forces generated within the gaps between directionally aligned fibres.[136]

Threads have been used for variety of applications, including bioanalysis,[137-143] and embedded in a hydrogel as a network for chemotaxis studies[144] or multilayer feeding of cell cultures.[145] Threads can be readily integrated into a gel to provide an easy and robust way to transport liquid in or out of a gel. Direct application of biomolecules onto a thread or yarn is trivial and enables dispatch at a targeted location.[138] Therefore, chapter 4 will introduce a novel electrofluidics system for precise control and manipulation of fluids on threads/sutures to deliver biomolecules into and throughout a gel, via control of an applied electric field, to provide a simple approach involving no moving parts or pumps. This work was possible through a collaboration between ARC Centre of Excellence for Electromaterials Science (ACES) nodes, the University of Tasmania (UTAS) and the University of Wollongong (UOW) node. Even though the theme of chapter 4 slightly diverges from the thesis main theme, this system was designed with the aim to be used for would healing application and be potentially integrated with the bioprinted PLGMA matrix in surgical wounds.

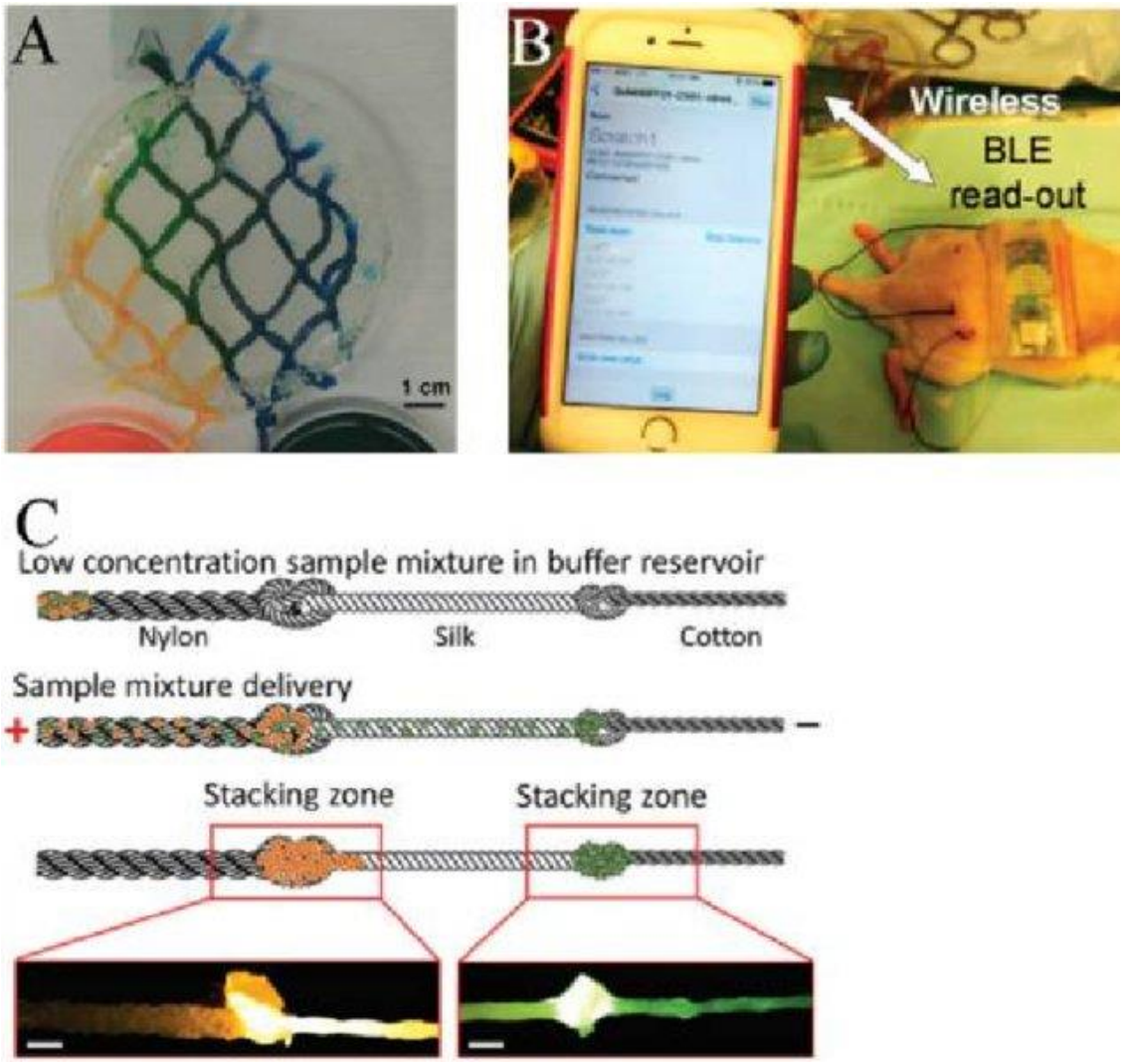

Figure 1.8 Incorporation of threads to electrofluidic and microfluidictechnology for biorelated studies.

(A) Acoustically driven fluid into a thread network embedded in transparent hydrogel. (B) pH-sensing system communicating with a smart phone via a Bluetooth platform. (c) The use of knotting to link different thread materials to trap bacteria for urinary tract infection. [146]

1.11 Research aim

This thesis will investigate two innovative approaches to meet the challenges of current wound healing treatments. The first approach will be introduced in chapters 2-3 and will detail the development and initial *in vitro* characterisation of a novel 3D multifunctional bioprinted skin platform based on platelet lysate. The hypothesis is that by developing a 3D printed platform containing multifunctional biomaterials and skin cells, this platform could be used to deliver cells and growth factors to the wound site, while providing a supportive network that mimics the native ECM for skin cells to infiltrate and thrive. The second approach will be introduced in chapter 4 and will detail the design development and proof-of-concept study of a novel electrofluidic approach for controlled delivery of bioactive molecule into soft tissue model using threads/surgical sutures. The hypothesis is that by using surgical sutures and electric field to deliver bioactive species into tissue-like materials, delivery of relevant drugs for wound healing could be finely controlled by alternating the field on/off.

1.12 References

[1] A. Mescher, Junqueira's Basic Histology: Text & Atlas (12th ed.), by Anthony L. Mescher, 2010.

[2] D.M. Supp, S.T. Boyce, Engineered skin substitutes: practices and potentials, Clin Dermatol 23(4) (2005) 403-12.

[3] F. Groeber, M. Holeiter, M. Hampel, S. Hinderer, K. Schenke-Layland, Skin tissue engineering--in vivo and in vitro applications, Adv Drug Deliv Rev 63(4-5) (2011) 352-66.

[4] R.F. Pereira, C.C. Barrias, P.L. Granja, P.J. Bartolo, Advanced biofabrication strategies for skin regeneration and repair, Nanomedicine (Lond) 8(4) (2013) 603-21.

[5] R.B. Groves, S.A. Coulman, J.C. Birchall, S.L. Evans, Quantifying the mechanical properties of human skin to optimise future microneedle device design, Comput Methods Biomech Biomed Engin 15(1) (2012) 73-82.

[6] D. Singh, D. Singh, S.S. Han, 3D Printing of Scaffold for Cells Delivery: Advances in Skin Tissue Engineering, Polymers (Basel) 8(1) (2016).

[7] S.H. Mathes, H. Ruffner, U. Graf-Hausner, The use of skin models in drug development, Adv Drug Deliv Rev 69-70 (2014) 81-102.

[8] I. Jones, L. Currie, R. Martin, A guide to biological skin substitutes, British Journal of Plastic Surgery 55(3) (2002) 185-193.

[9] L. Yildirimer, N.T.K. Thanh, A.M. Seifalian, Skin regeneration scaffolds: a multimodal bottom-up approach, Trends in Biotechnology 30(12) (2012) 638-648.

[10] A.D. Metcalfe, M.W.J. Ferguson, Bioengineering skin using mechanisms of regeneration and repair, Biomaterials 28(34) (2007) 5100-5113.

[11] S. Vijayavenkataraman, W.F. Lu, J.Y.H. Fuh, 3D bioprinting of skin: a state-of-the-art review on modelling, materials, and processes, Biofabrication 8(3) (2016) 032001.

[12] L.E. Tracy, R.A. Minasian, E.J. Caterson, Extracellular Matrix and Dermal Fibroblast Function in the Healing Wound, Adv Wound Care (New Rochelle) 5(3) (2016) 119-136.

[13] M. Xue, C.J. Jackson, Extracellular Matrix Reorganization During Wound Healing and Its Impact on Abnormal Scarring, Adv Wound Care (New Rochelle) 4(3) (2015) 119-136.

[14] S.A. Eming, P. Martin, M. Tomic-Canic, Wound repair and regeneration: mechanisms, signaling, and translation, Sci Transl Med 6(265) (2014) 265sr6.
[15] P.S. Briquez, J.A. Hubbell, M.M. Martino, Extracellular Matrix-Inspired Growth Factor Delivery Systems for Skin Wound Healing, Adv Wound Care (New Rochelle) 4(8) (2015) 479-489.
[16] C. Frantz, K.M. Stewart, V.M. Weaver, The extracellular matrix at a glance, Journal of cell science 123(Pt 24) (2010) 4195-4200.
[17] H. Jarvelainen, A. Sainio, M. Koulu, T.N. Wight, R. Penttinen, Extracellular matrix molecules: potential targets in pharmacotherapy, Pharmacol Rev 61(2) (2009) 198-223.
[18] G. Gatti, B. Casu, G.K. Hamer, A.S. Perlin, Studies on the conformation of heparin by ^{1}H and ^{13}C NMR spectroscopy, Macromolecules 12(5) (1979) 1001-1007.
[19] S. Sarrazin, W.C. Lamanna, J.D. Esko, Heparan sulfate proteoglycans, Cold Spring Harbor Perspectives in Biology 3(7) (2011) a004952.
[20] K. Sugahara, T. Mikami, T. Uyama, S. Mizuguchi, K. Nomura, H. Kitagawa, Recent advances in the structural biology of chondroitin sulfate and dermatan sulfate, Current Opinion in Structural Biology 13(5) (2003) 612-620.
[21] R. Sasisekharan, R. Raman, V. Prabhakar, Glycomics approach to structure-function relationships of glycosaminoglycans, Annual Review of Biomedical Engineering 8 (2006) 181-231.
[22] N. Itano, K. Kimata, Mammalian hyaluronan synthases, IUBMB Life 54(4) (2002) 195-199.
[23] J.M. Shah, E. Omar, D.R. Pai, S. Sood, Cellular events and biomarkers of wound healing, Indian J Plast Surg 45(2) (2012) 220-8.
[24] Y.S. Wu, S.N. Chen, Apoptotic cell: linkage of inflammation and wound healing, Front Pharmacol 5 (2014) 1.
[25] R. Riessen, T.N. Wight, C. Pastore, C. Henley, J.M. Isner, Distribution of hyaluronan during extracellular matrix remodeling in human restenotic arteries and balloon-injured rat carotid arteries, Circulation 93(6) (1996) 1141-7.
[26] S. Guo, L.A. Dipietro, Factors affecting wound healing, J Dent Res 89(3) (2010) 219-29.
[27] R.G. Frykberg, J. Banks, Challenges in the Treatment of Chronic Wounds, Adv Wound Care (New Rochelle) 4(9) (2015) 560-582.
[28] H. Sinno, S. Prakash, Complements and the wound healing cascade: an updated

review, Plast Surg Int 2013 (2013) 146764.
[29] K.R. Taylor, J.M. Trowbridge, J.A. Rudisill, C.C. Termeer, J.C. Simon, R.L. Gallo, Hyaluronan fragments stimulate endothelial recognition of injury through TLR4, J Biol Chem 279(17) (2004) 17079-84.
[30] M.C. Robson, Cytokine manipulation of the wound, Clin Plast Surg 30(1) (2003) 57-65.
[31] P. Olczyk, L. Mencner, K. Komosinska-Vassev, The role of the extracellular matrix components in cutaneous wound healing, Biomed Res Int 2014 (2014) 747584.
[32] G.C. Limandjaja, J.M. Belien, R.J. Scheper, F.B. Niessen, S. Gibbs, Hypertrophic and keloid scars fail to progress from the CD34−/α-smooth muscle actin (α-SMA)+ immature scar phenotype and show gradient differences in α-SMA and p16 expression, British Journal of Dermatology 182(4) (2020) 974-986.
[33] R.F. Pereira, P.J. Bartolo, Traditional Therapies for Skin Wound Healing, Adv Wound Care (New Rochelle) 5(5) (2016) 208-229.
[34] G.S. Lazarus, D.M. Cooper, D.R. Knighton, D.J. Margolis, R.E. Pecoraro, G. Rodeheaver, M.C. Robson, Definitions and Guidelines for Assessment of Wounds and Evaluation of Healing, Archives of Dermatology 130(4) (1994) 489-493.
[35] T. Velnar, T. Bailey, V. Smrkolj, The Wound Healing Process: An Overview of the Cellular and Molecular Mechanisms, Journal of International Medical Research 37(5) (2009) 1528-1542.
[36] N.J. Percival, Classification of Wounds and their Management, Surgery (Oxford) 20(5) (2002) 114-117.
[37] J.S. Boateng, K.H. Matthews, H.N.E. Stevens, G.M. Eccleston, Wound healing dressings and drug delivery systems: A review, Journal of Pharmaceutical Sciences 97(8) (2008) 2892-2923.
[38] H. Park, C. Copeland, S. Henry, A. Barbul, Complex wounds and their management, Surg Clin North Am 90(6) (2010) 1181-94.
[39] K.G. Harding, H.L. Morris, G.K. Patel, Healing chronic wounds, BMJ 324(7330) (2002) 160.
[40] R. Nunan, K.G. Harding, P. Martin, Clinical challenges of chronic wounds: searching for an optimal animal model to recapitulate their complexity, Disease Models & Mechanisms 7(11) (2014) 1205.
[41] M. Edmonds, Body of knowledge around the diabetic foot and limb salvage, J

Cardiovasc Surg (Torino) 53(5) (2012) 605-16.
[42] D.P. Orgill, Excision and skin grafting of thermal burns, New England Journal of Medicine 360(9) (2009) 893-901.
[43] B. ter Horst, G. Chouhan, N.S. Moiemen, L.M. Grover, Advances in keratinocyte delivery in burn wound care, Advanced Drug Delivery Reviews 123 (2018) 18-32.
[44] J.N. Mcheik, C. Barrault, G. Levard, F. Morel, F.-X. Bernard, J.-C. Lecron, Epidermal healing in burns: autologous keratinocyte transplantation as a standard procedure: update and perspective, Plastic and Reconstructive Surgery Global Open 2(9) (2014) e218.
[45] F.M. Wood, M.L. Kolybaba, P. Allen, The use of cultured epithelial autograft in the treatment of major burn injuries: A critical review of the literature, Burns 32(4) (2006) 395-401.
[46] F.M. Wood, M.L. Kolybaba, P. Allen, The use of cultured epithelial autograft in the treatment of major burn wounds: Eleven years of clinical experience, Burns 32(5) (2006) 538-544.
[47] J.F. Burke, I.V. Yannas, W.C. Quinby Jr, C.C. Bondoc, W.K. Jung, Successful use of a physiologically acceptable artificial skin in the treatment of extensive burn injury, Annals of Surgery 194(4) (1981) 413-427.
[48] M. Blais, R. Parenteau-Bareil, S. Cadau, F. Berthod, Concise review: tissue-engineered skin and nerve regeneration in burn treatment, Stem Cells Transl Med 2(7) (2013) 545-51.
[49] I.V. Yannas, J.F. Burke, D.P. Orgill, E.M. Skrabut, Wound tissue can utilize a polymeric template to synthesize a functional extension of skin, Science 215(4529) (1982) 174-176.
[50] N.J. Turner, S.F. Badylak, 18 - Engineered tissues for wound repair, in: D. Farrar (Ed.), Advanced Wound Repair Therapies, Woodhead Publishing2011, pp. 463-494.
[51] C.W. Patterson, M. Stark, S. Sharma, G.S. Mundinger, Regeneration and expansion of autologous full-thickness skin through a self-propagating autologous skin graft technology, Clinical Case Reports 7(12) (2019) 2449-2455.
[52] S. Xiong, X. Zhang, P. Lu, Y. Wu, Q. Wang, H. Sun, B.C. Heng, V. Bunpetch, S. Zhang, H. Ouyang, A Gelatin-sulfonated Silk Composite Scaffold based on 3D Printing Technology Enhances Skin Regeneration by Stimulating Epidermal Growth and Dermal Neovascularization, Sci Rep 7(1) (2017) 4288.

[53] L. Zaulyanov, R.S. Kirsner, A review of a bi-layered living cell treatment (Apligraf®) in the treatment of venous leg ulcers and diabetic foot ulcers, Clinical Interventions in Aging 2(1) (2007) 93-98.
[54] G. Naughton, J. Mansbridge, G. Gentzkow, A metabolically active human dermal replacement for the treatment of diabetic foot ulcers, Artificial Organs 21(11) (1997) 1203-1210.
[55] R.V. Shevchenko, S.L. James, S.E. James, A review of tissue-engineered skin bioconstructs available for skin reconstruction, Journal of the Royal Society Interface 7 (2010) 229-258.
[56] G. Gravante, M.C. Di Fede, A. Araco, M. Grimaldi, B. De Angelis, A. Arpino, V. Cervelli, A. Montone, A randomized trial comparing ReCell® system of epidermal cells delivery versus classic skin grafts for the treatment of deep partial thickness burns, Burns 33(8) (2007) 966-972.
[57] S.T. Boyce, A.L. Lalley, Tissue engineering of skin and regenerative medicine for wound care, Burns & trauma 6 (2018) 4-4.
[58] M. Albanna, K.W. Binder, S.V. Murphy, J. Kim, S.A. Qasem, W. Zhao, J. Tan, I.B. El-Amin, D.D. Dice, J. Marco, J. Green, T. Xu, A. Skardal, J.H. Holmes, J.D. Jackson, A. Atala, J.J. Yoo, *In situ* bioprinting of autologous skin cells accelerates wound healing of extensive excisional full-thickness wounds, Scientific Reports 9(1) (2019) 1-15.
[59] A. Skardal, D. Mack, E. Kapetanovic, A. Atala, J.D. Jackson, J. Yoo, S. Soker, Bioprinted amniotic fluid-derived stem cells accelerate healing of large skin wounds, Stem Cells Translational Medicine 1(11) (2012) 792-802.
[60] L. Fu, Delivery Systems in Wound Healing and Nanomedicine, 2016.
[61] J.W. Park, S.R. Hwang, I.S. Yoon, advanced growth factor delivery systems in wound management and skin regeneration, Molecules 22(8) (2017).
[62] T.J. Wieman, J.M. Smiell, Y. Su, Efficacy and Safely of a Topical Gel Formulation of Recombinant Human Platelet-Derived Growth Factor-BB (Becaplermin) in Patients With Chronic Neuropathic Diabetic Ulcers: A phase III randomized placebo-controlled double-blind study, Diabetes Care 21(5) (1998) 822.
[63] T.J. Wieman, Clinical efficacy of becaplermin (rhPDGF-BB) gel, The American Journal of Surgery 176(2, Supplement 1) (1998) 74S-79S.
[64] N. Papanas, E. Maltezos, Becaplermin gel in the treatment of diabetic neuropathic

foot ulcers, Clinical interventions in aging 3(2) (2008) 233-240.
[65] M. Abdelhakim, X. Lin, R. Ogawa, The Japanese Experience with Basic Fibroblast Growth Factor in Cutaneous Wound Management and Scar Prevention: A Systematic Review of Clinical and Biological Aspects, Dermatology and therapy 10(4) (2020) 569-587.
[66] J.I. Fernández-Montequín, B.Y. Betancourt, G. Leyva-Gonzalez, E.L. Mola, K. Galán-Naranjo, M. Ramírez-Navas, S. Bermúdez-Rojas, F. Rosales, E. García-Iglesias, J. Berlanga-Acosta, R. Silva-Rodriguez, M. Garcia-Siverio, L.H. Martinez, Intralesional administration of epidermal growth factor-based formulation (Heberprot-P) in chronic diabetic foot ulcer: treatment up to complete wound closure, International Wound Journal 6(1) (2009) 67-72.
[67] J.I. Fernandez-Montequin, C.M. Valenzuela-Silva, O.G. Diaz, W. Savigne, N. Sancho-Soutelo, F. Rivero-Fernandez, P. Sanchez-Penton, L. Morejon-Vega, H. Artaza-Sanz, A. Garcia-Herrera, C. Gonzalez-Benavides, C.M. Hernandez-Canete, A. Vazquez-Proenza, J. Berlanga-Acosta, P.A. Lopez-Saura, G. Cuban Diabetic Foot Study, Intra-lesional injections of recombinant human epidermal growth factor promote granulation and healing in advanced diabetic foot ulcers: multicenter, randomised, placebo-controlled, double-blind study, Int Wound J 6(6) (2009) 432-43.
[68] V. Viswanathan, U. Juttada, M. Babu, Efficacy of Recombinant Human Epidermal Growth Factor (Regen-D 150) in Healing Diabetic Foot Ulcers: A Hospital-Based Randomized Controlled Trial, Int J Low Extrem Wounds 19(2) (2020) 158-164.
[69] H.L. Tuyet, T.T. Nguyen Quynh, H. Vo Hoang Minh, D.N. Thi Bich, T. Do Dinh, D. Le Tan, H.L. Van, T. Le Huy, H. Doan Huu, T.N. Tran Trong, The efficacy and safety of epidermal growth factor in treatment of diabetic foot ulcers: the preliminary results, International Wound Journal 6(2) (2009) 159-166.
[70] S. Barrientos, H. Brem, O. Stojadinovic, M. Tomic-Canic, Clinical application of growth factors and cytokines in wound healing, Wound repair and regeneration : official publication of the Wound Healing Society [and] the European Tissue Repair Society 22(5) (2014) 569-578.
[71] G. Sandri, M.C. Bonferoni, S. Rossi, F. Ferrari, M. Mori, C. Del Fante, C. Perotti, C. Caramella, Thermosensitive eyedrops containing platelet lysate for the treatment of corneal ulcers, Int J Pharm 426(1-2) (2012) 1-6.
[72] K. Järbrink, G. Ni, H. Sönnergren, A. Schmidtchen, C. Pang, R. Bajpai, J. Car,

Prevalence and incidence of chronic wounds and related complications: a protocol for a systematic review, Systematic reviews 5(1) (2016) 152-152.

[73] Wound Closure & Advanced Wound Care Global Market - Forecast to 2026, IQ4I Research & Consultancy Pvt. Ltd, Research and Market, 2020, p. 566.

[74] Tissue Engineered - Skin Substitutes Market - Forecast (2020 - 2025), IndustryARC, Research and Market, 2020, p. 108.

[75] W.H.O. (WHO), Burns, 2018. https://www.who.int/news-room/fact-sheets/detail/burns. 2020).

[76] A.B. Association, Burn Incidence Fact Sheet, 2016. http://ameriburn.org/who-we-are/media/burn-incidence-fact-sheet/. 2020).

[77] S.R. Nussbaum, M.J. Carter, C.E. Fife, J. DaVanzo, R. Haught, M. Nusgart, D. Cartwright, An Economic Evaluation of the Impact, Cost, and Medicare Policy Implications of Chronic Nonhealing Wounds, Value Health 21(1) (2018) 27-32.

[78] R. Pacella, R. Tulleners, Q. Cheng, E. Burkett, H. Edwards, S. Yelland, D. Brain, J. Bingley, P. Lazzarini, J. Warnock, L. Barnsbee, T. Pacella, K. Clark, M. Smith, A. Iddir, I. Griffiths, G. Sussman, J. Van Netten, M. Gibb, J. Gordon, G. Harvey, D. Hickling, X. Lee, B. Ploderer, A. Vallejo, S. Whalley, N. Graves, Solutions to the chronic wounds problem in Australia: A call to action, Australian Centre for Health Services Innovation (AusHSI), Australia, 2018.

[79] P. He, J. Zhao, J. Zhang, B. Li, Z. Gou, M. Gou, X. Li, Bioprinting of skin constructs for wound healing, Burns and trauma 6(1) (2018) 5-5.

[80] L. Ning, X. Chen, A brief review of extrusion-based tissue scaffold bio-printing, Biotechnol J 12(8) (2017).

[81] W. Liu, M.A. Heinrich, Y. Zhou, A. Akpek, N. Hu, X. Liu, X. Guan, Z. Zhong, X. Jin, A. Khademhosseini, Y.S. Zhang, Extrusion Bioprinting of Shear-Thinning Gelatin Methacryloyl Bioinks, Adv Healthc Mater 6(12) (2017).

[82] I.T. Ozbolat, M. Hospodiuk, Current advances and future perspectives in extrusion-based bioprinting, Biomaterials 76 (2016) 321-43.

[83] X. Chen, G. Schoenau, W. Zhang, On the Flow Rate Dynamics in Time-Pressure Dispensing Processes, Journal of Dynamic Systems Measurement and Control-transactions of The Asme - J DYN SYST MEAS CONTR 124 (2002).

[84] J. Malda, J. Visser, F.P. Melchels, T. Jungst, W.E. Hennink, W.J. Dhert, J. Groll, D.W. Hutmacher, 25th anniversary article: Engineering hydrogels for biofabrication,

Adv Mater 25(36) (2013) 5011-28.
[85] A. Tirella, A. Orsini, G. Vozzi, A. Ahluwalia, A phase diagram for microfabrication of geometrically controlled hydrogel scaffolds, Biofabrication 1(4) (2009) 045002.
[86] S. Heid, A.R. Boccaccini, Advancing bioinks for 3D bioprinting using reactive fillers: A review, Acta Biomaterialia 113 (2020) 1-22.
[87] A. Pfister, R. Landers, A. Laib, U. Hübner, R. Schmelzeisen, R. Mülhaupt, Biofunctional rapid prototyping for tissue-engineering applications: 3D bioplotting versus 3D printing, Journal of Polymer Science Part A: Polymer Chemistry 42(3) (2004) 624-638.
[88] S. Huang, X. Fu, Naturally derived materials-based cell and drug delivery systems in skin regeneration, J Control Release 142(2) (2010) 149-59.
[89] C.W. Peak, J. Stein, K.A. Gold, A.K. Gaharwar, Nanoengineered colloidal inks for 3D bioprinting, Langmuir 34(3) (2018) 917-925.
[90] M. Müller, J. Becher, M. Schnabelrauch, M. Zenobi-Wong, Nanostructured Pluronic hydrogels as bioinks for 3D bioprinting, Biofabrication 7(3) (2015) 035006.
[91] W.L. Ng, J.T.Z. Qi, W.Y. Yeong, M.W. Naing, Proof-of-concept: 3D bioprinting of pigmented human skin constructs, Biofabrication 10(2) (2018) 025005.
[92] J. Visser, F.P. Melchels, J.E. Jeon, E.M. Van Bussel, L.S. Kimpton, H.M. Byrne, W.J. Dhert, P.D. Dalton, D.W. Hutmacher, J. Malda, Reinforcement of hydrogels using three-dimensionally printed microfibres, Nature Communications 6(1) (2015) 1-10.
[93] M.P. Lutolf, J.L. Lauer-Fields, H.G. Schmoekel, A.T. Metters, F.E. Weber, G.B. Fields, J.A. Hubbell, Synthetic matrix metalloproteinase-sensitive hydrogels for the conduction of tissue regeneration: engineering cell-invasion characteristics, Proceedings of the National Academy of Sciences 100(9) (2003) 5413-5418.
[94] W. Lee, J.C. Debasitis, V.K. Lee, J.-H. Lee, K. Fischer, K. Edminster, J.-K. Park, S.-S. Yoo, Multi-layered culture of human skin fibroblasts and keratinocytes through three-dimensional freeform fabrication, Biomaterials 30(8) (2009) 1587-1595.
[95] V. Lee, G. Singh, J.P. Trasatti, C. Bjornsson, X. Xu, T.N. Tran, S.-S. Yoo, G. Dai, P. Karande, Design and fabrication of human skin by three-dimensional bioprinting, Tissue Engineering, Part C: Methods 20(6) (2014) 473-484.
[96] M. Rimann, E. Bono, H. Annaheim, M. Bleisch, U. Graf-Hausner, Standardized 3D bioprinting of soft tissue models with human primary cells, Journal of Laboratory

Automation 21(4) (2016) 496-509.
[97] D. Min, W. Lee, I.H. Bae, T.R. Lee, P. Croce, S.S. Yoo, Bioprinting of biomimetic skin containing melanocytes, Experimental Dermatology 27(5) (2018) 453-459.
[98] F. Hafezi, N. Scoutaris, D. Douroumis, J. Boateng, 3D printed chitosan dressing crosslinked with genipin for potential healing of chronic wounds, International Journal of Pharmaceutics 560 (2019) 406-415.
[99] L. Koch, A. Deiwick, S. Schlie, S. Michael, M. Gruene, V. Coger, D. Zychlinski, A. Schambach, K. Reimers, P.M. Vogt, B. Chichkov, Skin tissue generation by laser cell printing, Biotechnology and Bioengineering 109(7) (2012) 1855-1863.
[100] S. Michael, H. Sorg, C.-T. Peck, L. Koch, A. Deiwick, B. Chichkov, P.M. Vogt, K. Reimers, Tissue engineered skin substitutes created by laser-assisted bioprinting form skin-like structures in the dorsal skin fold chamber in mice, PLoS One 8(3) (2013) e57741.
[101] N. Cubo, M. Garcia, J.F. del Cañizo, D. Velasco, J.L. Jorcano, 3D bioprinting of functional human skin: production and *in vivo* analysis, Biofabrication 9(1) (2016) 015006.
[102] W.L. Ng, W.Y. Yeong, M.W. Naing, Polyelectrolyte gelatin-chitosan hydrogel optimized for 3D bioprinting in skin tissue engineering, International Journal of Bioprinting 2(1) (2016) 53-62.
[103] L. Shi, L. Xiong, Y. Hu, W. Li, Z. Chen, K. Liu, X. Zhang, Three-dimensional printing alginate/gelatin scaffolds as dermal substitutes for skin tissue engineering, Polymer Engineering & Science 58(10) (2018) 1782-1790.
[104] L.J. Pourchet, A. Thepot, M. Albouy, E.J. Courtial, A. Boher, L.J. Blum, C.A. Marquette, Human skin 3D bioprinting using scaffold-free approach, Advanced Healthcare Materials 6(4) (2017) 1601101.
[105] C. Intini, L. Elviri, J. Cabral, S. Mros, C. Bergonzi, A. Bianchera, L. Flammini, P. Govoni, E. Barocelli, R. Bettini, M. McConnell, 3D-printed chitosan-based scaffolds: An *in vitro* study of human skin cell growth and an *in-vivo* wound healing evaluation in experimental diabetes in rats, Carbohydrate Polymers 199 (2018) 593-602.
[106] Y. Shi, T.L. Xing, H.B. Zhang, R.X. Yin, S.M. Yang, J. Wei, W.J. Zhang, Tyrosinase-doped bioink for 3D bioprinting of living skin constructs, Biomedical Materials 13(3) (2018) 035008.
[107] P. Admane, A.C. Gupta, P. Jois, S. Roy, C.C. Lakshmanan, G. Kalsi, B.

Bandyopadhyay, S. Ghosh, Direct 3D bioprinted full-thickness skin constructs recapitulate regulatory signaling pathways and physiology of human skin, Bioprinting 15 (2019) e00051.
[108] R.F. Pereira, A. Sousa, C.C. Barrias, P.J. Bártolo, P.L. Granja, A single-component hydrogel bioink for bioprinting of bioengineered 3D constructs for dermal tissue engineering, Materials Horizons 5(6) (2018) 1100-1111.
[109] L.Y. Daikuara, Z. Yue, D. Skropeta, G.G. Wallace, In vitro characterisation of 3D printed platelet lysate-based bioink for potential application in skin tissue engineering, Acta Biomaterialia 123 (2021) 286-297.
[110] X. Chen, Z. Yue, P.C. Winberg, J.N. Dinoro, P. Hayes, S. Beirne, G.G. Wallace, Development of rhamnose-rich hydrogels based on sulfated xylorhamno-uronic acid toward wound healing applications, Biomaterials Science 7(8) (2019) 3497-3509.
[111] X. Chen, Z. Yue, P.C. Winberg, Y.-R. Lou, S. Beirne, G.G. Wallace, 3D bioprinting dermal-like structures using species-specific ulvan, Biomaterials Science (2021).
[112] S. Datta, R. Sarkar, V. Vyas, S. Bhutoria, A. Barui, A. Roy Chowdhury, P. Datta, Alginate-honey bioinks with improved cell responses for applications as bioprinted tissue engineered constructs, Journal of Materials Research 33(14) (2018) 2029-2039.
[113] S.J. Lee, J.H. Lee, J. Park, W.D. Kim, S.A. Park, Fabrication of 3D Printing Scaffold with Porcine Skin Decellularized Bio-Ink for Soft Tissue Engineering, Materials (Basel) 13(16) (2020).
[114] B.S. Kim, J.-S. Lee, G. Gao, D.-W. Cho, Direct 3D cell-printing of human skin with functional transwell system, Biofabrication 9(2) (2017) 025034.
[115] B.S. Kim, G. Gao, J.Y. Kim, D.W. Cho, 3D cell printing of perfusable vascularized human skin equivalent composed of epidermis, dermis, and hypodermis for better structural recapitulation of native skin, Advanced Healthcare Materials 8(7) (2019) 1801019.
[116] B.S. Kim, Y.W. Kwon, J.-S. Kong, G.T. Park, G. Gao, W. Han, M.-B. Kim, H. Lee, J.H. Kim, D.-W. Cho, 3D cell printing of *in vitro* stabilized skin model and in *vivo* pre-vascularized skin patch using tissue-specific extracellular matrix bioink: a step towards advanced skin tissue engineering, Biomaterials 168 (2018) 38-53.
[117] K. Derr, J. Zou, K. Luo, M.J. Song, G.S. Sittampalam, C. Zhou, S. Michael, M. Ferrer, P. Derr, Fully three-dimensional bioprinted skin equivalent constructs with

validated morphology and barrier function, Tissue Engineering, Part C: Methods 25(6) (2019) 334-343.
[118] T. Baltazar, J. Merola, C. Catarino, C.B. Xie, N.C. Kirkiles-Smith, V. Lee, S. Hotta, G. Dai, X. Xu, F.C. Ferreira, W.M. Saltzman, J.S. Pober, P. Karande, Three dimensional bioprinting of a vascularized and perfusable skin graft using human keratinocytes, fibroblasts, pericytes, and endothelial cells, Tissue Engineering, Part A 26(5-6) (2020) 227-238.
[119] H. Kwak, S. Shin, H. Lee, J. Hyun, Formation of a keratin layer with silk fibroin-polyethylene glycol composite hydrogel fabricated by digital light processing 3D printing, Journal of Industrial and Engineering Chemistry 72 (2019) 232-240.
[120] F. Zhou, Y. Hong, R. Liang, X. Zhang, Y. Liao, D. Jiang, J. Zhang, Z. Sheng, C. Xie, Z. Peng, X. Zhuang, V. Bunpetch, Y. Zou, W. Huang, Q. Zhang, E.V. Alakpa, S. Zhang, H. Ouyang, Rapid printing of bio-inspired 3D tissue constructs for skin regeneration, Biomaterials 258 (2020) 120287.
[121] K. Yue, G. Trujillo-de Santiago, M.M. Alvarez, A. Tamayol, N. Annabi, A. Khademhosseini, Synthesis, properties, and biomedical applications of gelatin methacryloyl (GelMA) hydrogels, Biomaterials 73 (2015) 254-71.
[122] L. Kessler, S. Gehrke, M. Winnefeld, B. Huber, E. Hoch, T. Walter, R. Wyrwa, M. Schnabelrauch, M. Schmidt, M. Kückelhaus, M. Lehnhardt, T. Hirsch, F. Jacobsen, Methacrylated gelatin/hyaluronan-based hydrogels for soft tissue engineering, J Tissue Eng 8 (2017) 2041731417744157-2041731417744157.
[123] S. Xiao, T. Zhao, J. Wang, C. Wang, J. Du, L. Ying, J. Lin, C. Zhang, W. Hu, L. Wang, K. Xu, Gelatin Methacrylate (GelMA)-Based Hydrogels for Cell Transplantation: an Effective Strategy for Tissue Engineering, Stem Cell Reviews and Reports 15(5) (2019) 664-679.
[124] X. Zhao, Q. Lang, L. Yildirimer, Z.Y. Lin, W. Cui, N. Annabi, K.W. Ng, M.R. Dokmeci, A.M. Ghaemmaghami, A. Khademhosseini, Photocrosslinkable Gelatin Hydrogel for Epidermal Tissue Engineering, Advanced healthcare materials 5(1) (2016) 108-118.
[125] J.K. Carrow, P. Kerativitayanan, M.K. Jaiswal, G. Lokhande, A.K. Gaharwar, Chapter 13 - Polymers for Bioprinting, in: A. Atala, J.J. Yoo (Eds.), Essentials of 3D Biofabrication and Translation, Academic Press, Boston, 2015, pp. 229-248.
[126] N.E. Fedorovich, W. Schuurman, H.M. Wijnberg, H.J. Prins, P.R. van Weeren, J.

Malda, J. Alblas, W.J. Dhert, Biofabrication of osteochondral tissue equivalents by printing topologically defined, cell-laden hydrogel scaffolds, Tissue Eng Part C Methods 18(1) (2012) 33-44.
[127] I. Pepelanova, K. Kruppa, T. Scheper, A. Lavrentieva, Gelatin-Methacryloyl (GelMA) Hydrogels with Defined Degree of Functionalization as a Versatile Toolkit for 3D Cell Culture and Extrusion Bioprinting, Bioengineering 5(3) (2018) 55.
[128] M. Vigata, C. Meinert, S. Pahoff, N. Bock, D. Hutmacher, Gelatin Methacryloyl Hydrogels Control the Localized Delivery of Albumin-Bound Paclitaxel, Polymers 12 (2020) 501.
[129] E. Jooybar, M.J. Abdekhodaie, M. Karperien, A. Mousavi, M. Alvi, P.J. Dijkstra, Developing hyaluronic acid microgels for sustained delivery of platelet lysate for tissue engineering applications, International Journal of Biological Macromolecules 144 (2020) 837-846.
[130] L.Y. Daikuara, Z. Yue, D. Skropeta, G.G. Wallace, In vitro characterisation of 3D printed platelet lysate-based bioink for potential application in skin tissue engineering, Acta Biomaterialia (2021).
[131] K. Plöderl, C. Strasser, S. Hennerbichler, A. Peterbauer-Scherb, C. Gabriel, Development and validation of a production process of platelet lysate for autologous use, Platelets 22(3) (2011) 204-209.
[132] C.E. Martínez, P.C. Smith, V.A. Palma Alvarado, The influence of platelet-derived products on angiogenesis and tissue repair: a concise update, Frontiers in Physiology 6(290) (2015).
[133] S.C.N.d.S. Santos, Ó.E. Sigurjonsson, C.d.A. Custódio, J.F.C.d.L. Mano, Blood Plasma Derivatives for Tissue Engineering and Regenerative Medicine Therapies, Tissue Engineering Part B: Reviews 24(6) (2018) 454-462.
[134] G.L. Koons, A.G. Mikos, Progress in three-dimensional printing with growth factors, J Control Release 295 (2019) 50-59.
[135] W. Wan, F. Cai, J. Huang, S. Chen, Q. Liao, A skin-inspired 3D bilayer scaffold enhances granulation tissue formation and anti-infection for diabetic wound healing, Journal of Materials Chemistry B 7(18) (2019) 2954-2961.
[136] S. Farajikhah, J.M. Cabot, P.C. Innis, B. Paull, G. Wallace, Life-Saving Threads: Advances in Textile-Based Analytical Devices, ACS Comb Sci 21(4) (2019) 229-240.
[137] C. Zhao, S. Farajikhah, C. Wang, J. Foroughi, X. Jia, G.G. Wallace, 3D braided

yarns to create electrochemical cells, Electrochemistry Communications 61 (2015) 27-31.
[138] J.M.J.M. Cabot, N.P.N.P. Macdonald, S.C.S.C. Phung, M.C. Breadmore, B. Paull, Fibre-based electrofluidics on low cost versatile 3D printed platforms for solute delivery, separations and diagnostics; from small molecules to intact cells, The Analyst 141(23) (2016) 6422-6431.
[139] R. Safavieh, G.Z. Zhou, D. Juncker, Microfluidics made of yarns and knots: from fundamental properties to simple networks and operations, Lab on a chip 11(15) (2011) 2618-2624.
[140] P. Mostafalu, M. Akbari, K.A. Alberti, Q. Xu, A. Khademhosseini, S.R. Sonkusale, A toolkit of thread-based microfluidics, sensors, and electronics for 3D tissue embedding for medical diagnostics, Microsystems & Nanoengineering 2(April) (2016) 16039-16039.
[141] J.M. Cabot, M.C. Breadmore, B. Paull, Thread based electrofluidic platform for direct metabolite analysis in complex samples, Analytica Chimica Acta (2017).
[142] X. Li, J. Tian, W. Shen, Thread as a versatile material for low-cost microfluidic diagnostics, ACS Applied Materials and Interfaces 2(1) (2010) 1-6.
[143] M. Reches, K.A. Mirica, R. Dasgupta, M.D. Dickey, M.J. Butte, G.M. Whitesides, Thread as a Matrix for Biomedical Assays, ACS Applied Materials and Interfaces 2(6) (2010) 1722-1728.
[144] S. Ramesan, A.R. Rezk, K.W. Cheng, P.P.Y. Chan, L.Y. Yeo, Acoustically-driven thread-based tuneable gradient generators, Lab Chip 16(15) (2016) 2820-2828.
[145] A. Nilghaz, S. Hoo, W. Shen, X. Lu, P.P.Y. Chan, Multilayer cell culture system supported by thread, Sensors and Actuators, B: Chemical 257 (2018) 650-657.
[146] S. Farajikhah, J. Cabot, P. Innis, B. Paull, G. Wallace, Life-Saving Threads: Advances in Textile-Based Analytical Devices, ACS Combinatorial Science 21 (2019).

2 Chapter

In vitro characterization of 3D printed platelet lysate-based bioink for potential application in skin tissue engineering

The work presented in this chapter was adapted from the manuscript published at the Journal Acta Biomaterialia S1742-7061(21)00048-9 (2021). doi: 10.1016/j.actbio.2021.01.021 by Daikuara LY, Yue Z, Skropeta D, Wallace GG. In vitro characterisation of 3D printed platelet lysate-based bioink for potential application in skin tissue engineering.

Table of Contents

2.1 Introduction

Platelet derived products have been gaining considerable attention lately as an autologous source of biologically active molecules[71] and have been proposed for regeneration of skin wounds,[147-150] bone,[151] cartilage,[152] cornea[153] and ligaments[154]. Platelet lysate (PL), obtained by disruption of platelets, has been used in the clinic as a topical administration or local injection to damaged tissue.[155] Despite the optimistic scenario, the major drawback of these approaches is the poor retention of bioactive molecules to the wound site due to rapid access of these molecules to the blood stream and excessive enzymatic degradation, hindering the effectiveness of the therapy.[155] Since The therapeutical outcome of GFs are known to be dependent on their spatial distribution. Controlling the delivery of GFs both spatially and temporally is essential for successful translation of GFs as a regenerative medicine tool into clinical practice.[61] In order to meet these challenges, the combination of bioprinting technology and platelet bioproducts has been proposed for the fabrication of functional tissue engineering models[156, 157] Bioprinting is an attractive approach to fabricate effective 3D hydrogel-based delivery systems that can mimic the function of the target tissue, protect GFs from degradation and enable spatial-temporal GF delivery.

As the interest for PL rises, more studies about the incorporation of PL into different platforms for tissue regeneration have been reported,[155, 158] however, its use as a bioink component for wound healing application has yet to be explored. Therefore, as the initial step towards the biofabrication of a complex skin equivalent which can co-deliver GFs and skin cells for complete functional regeneration of skin, the present work focused on the development of a multifunctional bioink for the fabrication of a 3D printed dermal equivalent and *in vitro* investigation of its potential to deliver relevant

GFs while providing support for cell proliferation and deposition of extracellular matrix (ECM). Herein, we demonstrated that by direct assembly of biologically active GFs into a 3D polymeric network, we were able to achieve controlled release of GFs, at the same time, immobilized GFs in the matrix showed a positive effect on cell behaviour. The proposed platform was evaluated regarding its physical, rheological, and mechanical properties. The cytocompatibity of the bioink formulation were firstly assessed by means of *in vitro* cellular viability, proliferation, morphology, and ECM production using human dermal fibroblasts (HDFs), cells of great importance in the wound healing process and commonly used in bioengineered dermal equivalents. [159-161] Potential application of the proposed bioengineered skin equivalent includes use in the clinic for wound healing, providing temporary wound coverage while supporting new tissue formation; and as an ex-vivo skin model for animal-free testing.

2.2 Experimental Section

2.2.1 General materials

Key materials used in this chapter are introduced in detail as follow.

Materials	Source	Cat Number
Ink formulation		
Human dermal fibroblasts	Cell Applications	-
Human platelet lysate (PL)	PL BioScience	-
Heparin	Sigma-Aldrich	H3149
Gelatin (porcine skin, Type A, 300 Bloom)	Sigma-Aldrich	G2500
Methacrylic anhydride	Sigma-Aldrich	P5927
Lithium phenyl-2,4,6-trimethylbenzoylphosphinate (LAP)	Sigma-Aldrich	900889
DMEM, high glucose, HEPES	Sigma-Aldrich	D1152
Fetal Bovine Serum	Interpath	SFBSN2
Penicillin/Streptomycin	Gibco	15140122
Characterisation		
PrestoBlueTM	Invitrogen	A13262
Calcein AM	Invitrogen	C3099
Propidium iodide (PI)	Invitrogen	P3566
Donkey serum	Merck	S30
Paraformaldehyde	Fluka	76240
PBS tablet	Sigma-Aldrich	P3813
Triton X-100	Sigma-Aldrich	T8532
Collagenase (type I)	Sigma-Aldrich	C2674
Antibodies		
Rabbit polyclonal anti-collagen I	ABCAM	ab21286
Rabbit polyclonal anti-collagen III	ABCAM	ab7778
Rabbit polyclonal anti-elastin	ABCAM	ab21610
Rabbit polyclonal anti-fibronectin	ABCAM	ab2413
Alexa Fluor 488	Invitrogen	a21206
DAPI	Invitrogen	D1306
PCR		
AurumTM Total RNA 96 Kit	Bio-rad	7326800
iScript RT Supermix, 100 rxns	Bio-rad	1708841
SYBR® Select Master Mix	Life Technologies	4472897

ELISA		
DuoSet ELISA development kit PDGF-AB	R&D Systems	DY222
DuoSet ELISA development kit VEGF	R&D Systems	DY293B
DuoSet Ancillary Reagent Kit 2	R&D Systems	DY008
Simple Step ELISA kit PDGF-BB	ABCAM	ab184860
Simple Step ELISA kit EGF	ABCAM	ab217772
Simple Step ELISA kit FGF	ABCAM	ab219636
ELISA kit TGF-β1	ABCAM	ab108912

2.2.2 Cell culture

Human dermal fibroblasts (HDFs; Cell Applications) were cultured in Dulbecco's Modified Eagle Medium (DMEM, high glucose, HEPES; Sigma-Aldrich) supplemented with 10% *v/v* fetal bovine serum (FBS), 1% *v/v* penicillin/streptomycin (P/S) under standard culture conditions in a humidified atmosphere with 5% CO2 at 37°C. Culture media was changed every three days. The cells were routinely passaged in tissue culture flasks when they reached 80% confluence and were discarded after 20 passages to ensure reproducibility of key characteristics.

2.2.3 Human platelet lysate

Human platelet lysate (PL) research grade was provided by PL BioScience (PL BioScience GmbH). After thawing, 2U of heparin was added, PL was aliquoted in 1mL Eppendorf tubes and stored at -80°C as recommended. Some aliquots were stored at -20°C to be used within two months. Before use, PL was thawed in the water bath. Repeated freeze-thaw cycles were avoided to prevent precipitation.

2.2.4 Gelatin methacryloyl (GelMA)

Gelatin methacryloyl (GelMA) was synthesized by a direct reaction of gelatin with methacrylic anhydride. Gelatin (porcine skin, Type A, 300 Bloom, Sigma-Aldrich) was dissolved in 10% *w/v* phosphate buffered saline (PBS), the solution was then autoclaved using the liquid cycle. Sterilised gelatin solution was vigorously stirred at 37°C, while methacrylic anhydride (0.6 mL/g gelatin) (MW=154.16, Sigma-Aldrich) was added. The reaction was continued for 4 hours and terminated by centrifugation. Next, 5M sodium hydroxide was added to the supernatant to adjust the pH 7. Chloroform was added to the solution for sterilization purposes and the solution was dialyzed against deionized water at 50°C for 4 days (cellulose membrane, molecular weight cut off (MWCO): 12kDa). Lastly, the dialyzed GelMA solution was lyophilized and stored at -30°C until further use. High degree of functionalization was verified by 1H nuclear magnetic resonance (NMR) using a Bruker Avance III HD 400 MHz NMR spectrometer (Bruker BioSpin Corp., Billerica, USA) (Figure 2.S1).

2.2.5 Bioink formulation

The HDF-PLGMA bioink was formulated as follow. HDF cells from passage 5 were retrieved from liquid nitrogen and sub-cultured twice before being harvested with trypsin and collected by centrifugation at 1200 rpm for 5 minutes. Cells were then reconstituted in PLGMA bioink – based on a blend of 50% *v/v* PL, 15% *w/v* GelMA dissolved in DMEM (supplemented with 10% *v/v* FBS, 1% *v/v* P/S) and 0.06% *w/v* lithium phenyl-2,4,6-trimethylbenzoylphosphinate (LAP) – at a cell density of 1×10^6 cells/mL.

The HDF-GelMA control bioink was formulated as follow. HDF were then reconstituted in GelMA bioink –15% *w/v* GelMA dissolved in DMEM (supplemented with 10% *v/v* FBS, 1% *v/v* P/S) and 0.06% *w/v* LAP – at a cell density of 1×10^6 cells/mL. All steps were performed within a sterile biosafety cabinet following good laboratory guidelines to ensure sterility.

If not stated otherwise, experiments were performed with a PLGMA formulation containing a blend of 50% v/v PL, 15% w/v GelMA and 0.06% w/v LAP, and GelMA control formulation containing 15% w/v GelMA and 0.06% w/v LAP.

2.2.6 Fabrication of casted constructs

Constructs were casted by pipetting the ink formulation into custom-made moulds of dimensions 8mm·5mm (D·H) and subjecting to UV light of 400 nm wavelength (λ) for 60 s (792 mJ). Immediately after crosslinking, constructs were placed in 12 well-plates containing DMEM (10% v/v FBS, 1% v/v P/S) and cultured under 5% CO_2 at 37°C.

2.2.7 Fabrication of 3D bioprinted constructs

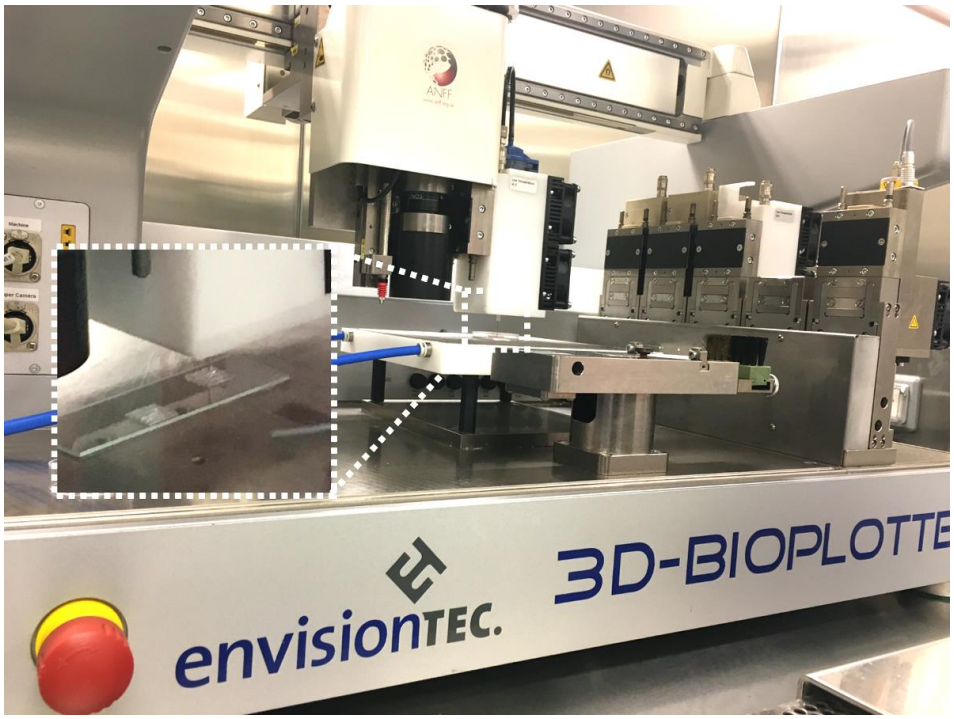

Figure 2.1 Bioplotter used for fabrication of biological relevant constructs.

A pneumatic extrusion-based 3D Bioplotter (Envision TEC, Gladbeck, Germany) positioned inside a Class II biological safety cabinet was used to fabricate the 3D printed PL-based (PLGMA) constructs. The 3D cuboid model was designed using CAD software, exported as STL files, and sliced into layers using the Bioplotter RP® software. The 3D constructs were then fabricated layer-by-layer in a dimension of 10 mm·10 mm·2 mm (W·L·H) with 0°/90° a crosshatch pattern, using disposable needle tips of 200 µm, a slicing thickness 200 µm and strand spacing of 1.0 mm. For optimal plotting of PLGMA constructs, the ink was allowed to reach the equilibrium temperature (19°C) for 5-10minutes, the ink was then printed at a speed of 10 mm/s under a pneumatic pressure of 2.6 bar onto a cooled platform (15°C). Right after printing, constructs were moved to the crosslinking station where they were crosslinked

under UV light of 400 nm wavelength (λ) for 60 seconds (792 mJ). Immediately after crosslinking, constructs were placed in 12 well plates containing DMEM (10% *v*/*v* FBS, 1% *v*/*v* P/S). After all constructs were printed, well plates were placed in a double container and transferred to a PC2 laboratory. Growth media was then changed in a biosafety cabinet (BSC) utilising sterile instruments and wearing proper personal protective equipment (PPE) and constructs were cultured under 5% CO_2 at 37°C until they were ready for experimentation.

2.2.8 Preliminary bioink characterization

The preliminary experiment to assess the printability of ink formulation was carried as follow. Ink formulations were loaded into 1 mL disposable syringes and extruded manually using constant force on microscope glass slides. Viscosity and extrudability of different inks were determined from visual qualitative evaluation of single extruded filaments images. The formulations were then compared according to those indicators, and further rheological investigation was then carried with the ink formulation which presented best behaviour in the qualitative printability evaluation.

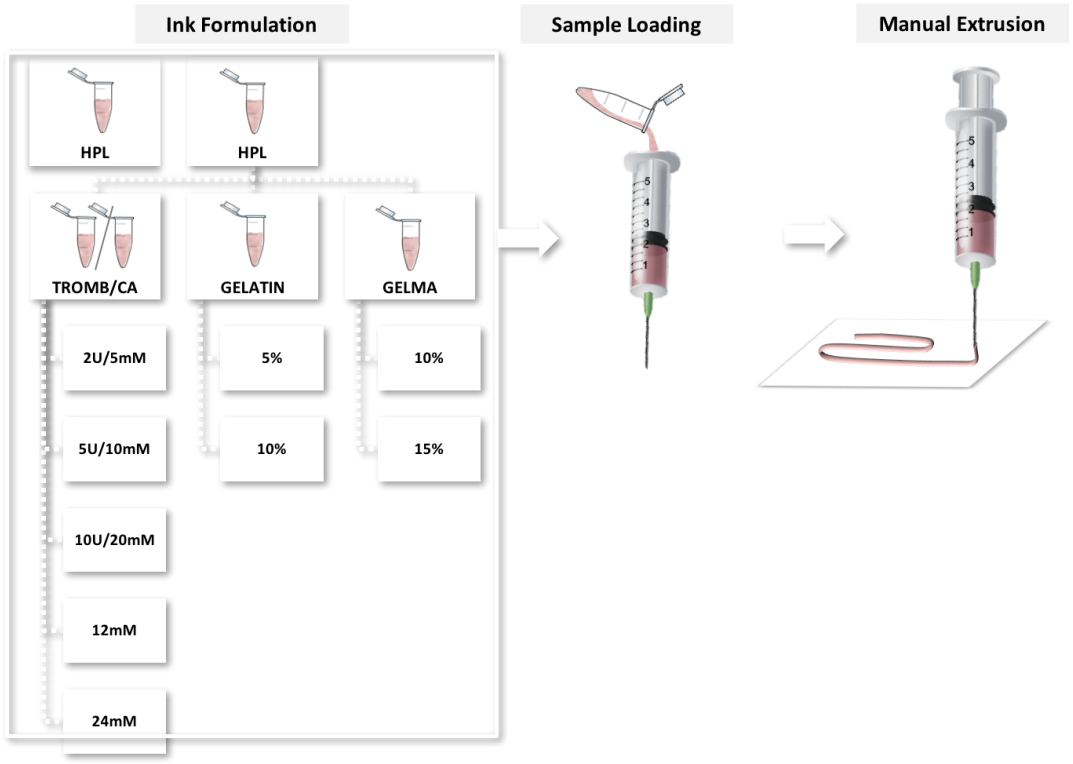

Figure 2.2 Schematic representation of the preliminary experiment used to measure the ink printability.

2.2.9 Rheological characterization

Oscillatory and rotational rheological characterization were performed using an AR-G2 rheometer (TA Instruments) fitted with a stainless-steel cone-plate geometry (15 mm/ 2°/ 55 μm). Pre-shear of 0.6 Pa was applied for 1 minute and the bioink was allowed to reach the equilibrium temperature for 2 minutes prior to performing the experiments. For each measurement, the cell-free bioink (PLGMA bioink, GelMA control and PL control) was loaded in a liquid state onto the Peltier stage, tested only once and discarded once investigated. Oscillatory temperature sweep from 35°C to 5°C at a rate of 1.5°C/min, time sweep up to 10 minutes and stress sweep from 0.1 to 1000 were carried out at a constant strain and frequency of 1% and 1Hz respectively. Strain sweep from 0.01 to 1 was performed at fixed frequency of 1Hz and frequency sweep from 0.1

to 100 Hz was performed at a fixed strain of 1%. The rotational steady state flow was carried out at a shear rate (s^{-1}) from 0.1 to 100 s^{-1} to analyse whereas the fluid's viscosity decreases over time under shearing.

Figure 2.3 AR-G2 rheometer fitted with a stainless-steel cone-plate geometry

2.2.10 Shape fidelity

After printing, shape fidelity was assessed by qualitative screening of extruded filaments from macroscopic images and by the printability index (*Pr*) according to Ouyang et al. parameter.[162] Macroscopic images of PLGMA printed constructs were processed using ImageJ software, which measured the perimeter and area of interconnected channels (n > 20). The *Pr* value was then calculated to find the pore perimeter normalized by pore area following this equation:

$$Pr = L^2/16A \qquad \text{Eq. (1)}$$

Where, L is perimeter and A is area. Pr = 1 indicates perfect extrusion line uniformity and Pr > 1.1 had unacceptable uniformity.

2.2.11 Mechanical characterization

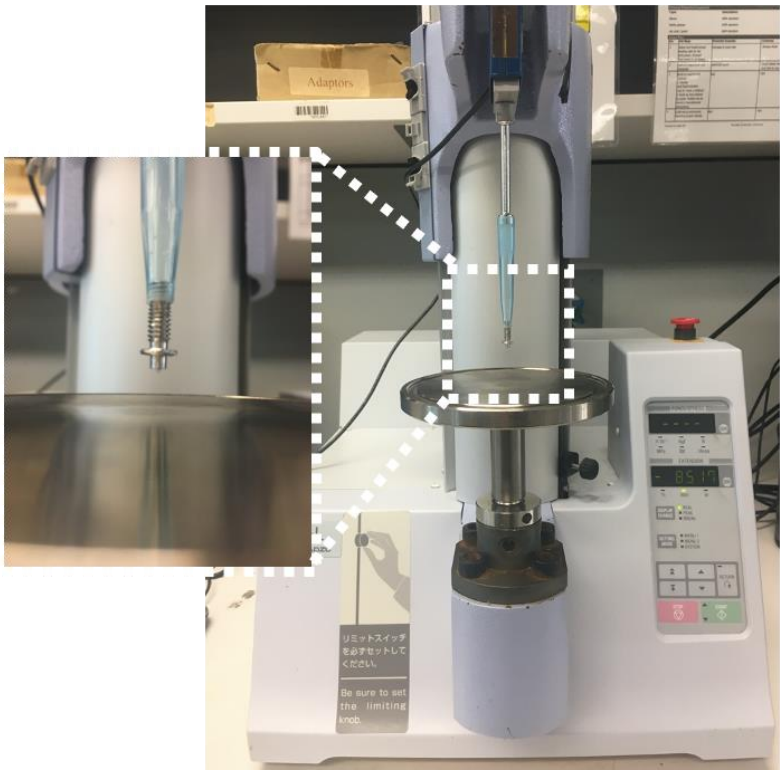

Figure 2.4 EZ-S mechanical tester.

The indentation test was carried out on an EZ-S mechanical tester (Shimadzu Co.) using a cylindrical flat ended, stainless-steel indenter (990 μm in diameter) attached to a 10 N load cell at a crosshead speed of 0.5 mm/min. The Young's modulus of each cell-free PLGMA construct was calculated through the slope of the applied force against indentation depth (0-100 μm) plot following this equation:

$$F = 8/3\, aEd \qquad \text{Eq. (2)}$$

Where, F is the applied force (Newton), d is the indentation depth (mm), and a is the radius of the indenter tip (0.495 mm). The slope of the linear fit was then used to

calculate the hydrogel modulus (E). In each case, five cell-free specimens were tested, and the average values were calculated.

2.2.12 Swelling behavior

The swelling behaviour of cell-free PLGMA casted constructs and GelMA control was evaluated after incubation in solutions PBS solution pH 7.4 or pH 5 (to simulate swelling behaviour in different stages of the healing process) at 37 °C for 24 h to reach the swelling equilibrium. After removal from the swelling solution, the constructs were gently blotted with Kimwipes to remove residual liquid, and the swollen weight of each construct was recorded (Ws). The samples were subsequently lyophilized and weighed again to determine the dry weight of each construct (Wd). The swelling ratio of the swollen hydrogels was calculated according to equation (3). [124, 163]

$$WU = (WS - WD)/WD \qquad \text{Eq. (3)}$$

Three samples of each group were used to calculate the means and standard deviation.

2.2.13 Enzymatic degradation

Accelerated enzymatic degradation of cell-free PLGMA constructs and GelMA control was performed as follows. After polymerization, casted constructs were placed in 24-well plate and allowed to reach swelling equilibrium overnight at 37 ◦C. Following this, constructs were gently blotted with Kimwipes to remove the residual liquid, and the initial weight of each construct was recorded (W_1). Constructs were then immersed in the digest solution containing type I collagenase (Sigma-Aldrich) dissolved in PBS (pH 7.4) and incubated at 37 ◦C. [164] At specific time points, samples were removed from the enzymatic solution, gently blotted, and the residual mass was of each construct was

recorded (W_2). The degree of degradation of each sample at specific time point was calculated according to the following equation:

$$Residual\ mass(\%) = W2/W1 * 100 \quad \text{Eq. (4)}$$

Four samples of each group were used to calculate the mean and standard deviation.

2.2.14 Growth factor release

The *in vitro* release study of GFs from cell-free printed PLGMA were carried out in PBS at 37 °C for up to 2 weeks. After UV crosslinking, the 3D printed constructs were placed in a 24 well-plate containing 1 mL of PBS/well, which was changed to new PBS prior to incubation to remove non-crosslinked material. Samples were then incubated at 37°C. At determinate time points (day 1, 3, 5, 7, 10 and 14), the supernatant was collected and stored at -20 °C until further use. Total amount of GF in the PL raw material and amounts of the released GFs from the PLGMA constructs were quantified by Enzyme-Linked Immunosorbent Assay (ELISA) according to the manufacturer's protocol. PDGF-αβ and VEGF were quantified using respective DuoSet ELISA development kit with DuoSet Ancillary Reagent Kit 2. PDGF-ββ, EGF, FGF and TGF-β1 were quantified using the Simple Step ELISA kit (ABCAM). Concentrations of GF were calculated based on a standard curve generated using the standard run with that assay. The optical density of the three replicates were used to calculate the means and standard deviation. At day 14, constructs were enzymatically digested using 20 U of collagenase I and the amounts of entrapped GFs were quantified by ELISA respectively. The GF release profile was calculated according to the following equation:

$$(GF\ released)/(GF\ total)\ \times\ 100\% \quad \text{Eq. (5)}$$

Where $GF_{released}$ is the amount of GF released at specific time point and GF_{total} is the sum of GF released plus GF remaining in the PLGMA construct.

2.2.15 HDF morphology, viability, and proliferation

Actin filaments from the HDF cytoskeleton were visualized by phalloidin staining according to the manufacturer protocol (ThermoFisher Scientific). HDF-laden PLGMA constructs and HDF-laden GelMA control were first fixed in 3.7% paraformaldehyde for 30 minutes. Fixed samples were incubated in a blocking solution containing 5% *v/v* donkey serum diluted in 0.3% *v/v* Triton X-100 at room temperature for 1 hour. Samples were then stained with Alexa Fluor 488 phalloidin (5:200) in 5% *v/v* donkey serum for 1 hour and counterstained with 4′,6-di-amidino-2-phenylindole dihydrochloride (DAPI, 1 μg/mL) diluted in 5% *v/v* donkey serum for 10 minutes and imaged using a confocal laser scanning microscope (Leica TSC SP5 II). Cell viability was evaluated through LIVE/DEAD staining using calcein AM (5 μg/mL) / propidium iodide (PI, 1 μg/mL) according to the manufacturer protocol. Images were acquired at day 1, 7 and 14. ImageJ was used to quantify the number of total live and dead cells within the samples (n = 10). The PrestoBlue assayTM was performed according to the manufacturer's protocol to measure the proliferation of HDFs encapsulated in the 3D printed hydrogels. Cells were cultured up to 14 days and data was collected at day 1, 7 and 14. At these time points, samples were incubated with the PrestoBlue reagent, and their optical density (OD) was measured at 544/590 nm using a microplate reader (POLAR star Omega, BMG Labtech). Three independent samples of each group were used to calculate the means and standard deviations.

2.2.16 Immunohistochemistry assay

HDF-laden PLGMA constructs were first fixed in 3.7% *w/v* paraformaldehyde for 30 minutes. Fixed samples were incubated in a blocking solution containing 10% *v/v* donkey serum in PBS diluted in 0.3% *v/v* Triton X-100 at room temperature for 1 hour. Samples were then incubated with primary antibody appropriately diluted in antibody dilution buffer, 10% *v/v* donkey serum in PBS, overnight at 4°C. Rinsed with 0.1% *v/v* Triton X-100 in PBS for three changes. The primary antibodies used were rabbit polyclonal anti-collagen I, rabbit polyclonal anti-collagen III, rabbit polyclonal anti-elastin. Samples were incubated with Alexa 488 anti-rabbit conjugated secondary antibody at room temperature for 1 hour. Rinsed with 0.1% *v/v* Triton X-100 in PBS for three changes. Lastly, samples were counterstained with DAPI at room temperature for 5 minutes, rinsed and mounted. The staining was then imaged by confocal laser scanning microscopy (Leica TSC SP5 II, USA).

2.2.17 RNA isolation and RT-qPCR analysis

Real-Time PCR was used to quantify the gene expression of type I and type III collagen, fibronectin and elastin, major components of the ECM synthesized by fibroblasts. HDF-laden PLGMA constructs and HDF-laden GelMA control were first mechanically broken using a tissue homogeniser. Total RNA was extracted from cells using AurumTM Total RNA Mini Kit according to the manufacturer's protocol. The RNA isolated was then reverse transcribed into cDNA according to the manufacturer's protocol. After cDNA transcription, cDNA was quantified by Nanodrop and normalized to 50 ng/mL. Real-time PCR was then performed using the SsoAdvancedTM Universal SYBR® Green RT- PCR Kit. A list of primer sequence information is provided in Table 2.S1. All reactions were performed in triplicate. Relative gene expression represents

data normalized to GAPDH and expressed relative to 2D HDFs. Data were analysed according to the comparative threshold Cycle ($\Delta\Delta Ct$) method using the formula:

$$\Delta Ct = Ct\ target - Ct\ norm \quad \text{Eq. (6)}$$

$$\Delta\Delta Ct = \Delta Ct\ sample - \Delta Ct\ calibrator \quad \text{Eq. (7)}$$

$$Relative\ gene\ expression = 2^{-\Delta\Delta Ct} \quad \text{Eq. (8)}$$

Firstly, ΔCt is calculated by the difference between Ct values of the target and the normalizer (housekeeping gene), subsequently, samples are normalized to the ΔCt of a control (2D HDFs culture), which is then used to find the relative expression of the gene of interest using the expression $2^{-\Delta\Delta Ct}$. Means and standard deviation for each relative gene expression were calculated.

2.2.18 Statistical analysis

One-way analysis of variance (ANOVA) test followed by Tukey's post-hoc test was used to assess the statistical significance of results between groups. The statistical analysis was performed with the software OriginPro at a confidence level of 95%. Differences were considered statistically significant at $p < 0.05$. Data were expressed as the mean ± standard deviation (SD) for $n > 3$.

2.3 Results

2.3.1 Bioink formulation and characterization

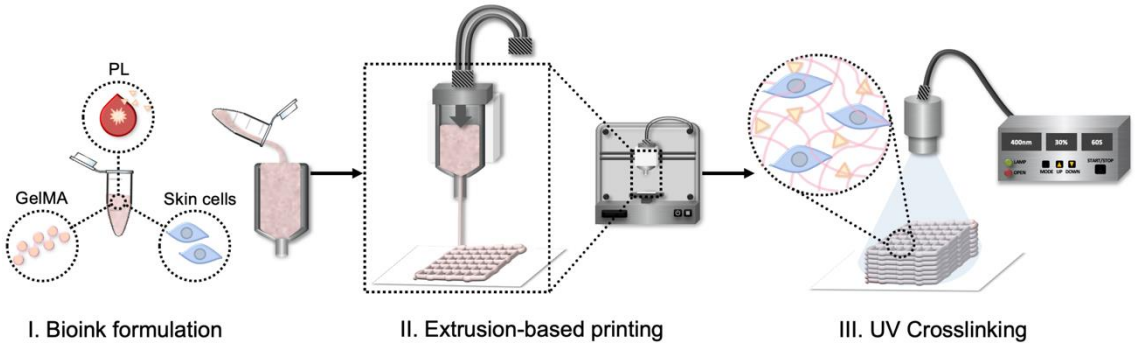

Figure 2.5 Schematic representation of the bioprinting process from material selection/ink formulation to shape fixation though UV light.

GelMa – gelatin methacryloyl, PL – platelet lysate, Skin cells – human dermal fibroblasts. The fabrication process of the 3D printed multifunctional construct consisting of platelet lysate (PL) and gelatin methacryloyl (GelMA) (PLGMA) is illustrated in Figure 2.6 showing the pre-printing, printing, and post-printing stages. This process enables encapsulation of cells and direct immobilization of GFs in the PLGMA final 3D printed construct.

Table 2.1 Preliminary experiments on ink viscosity.

	PL	DMEM	Thrombin (U)	Ca (mM)	Gelatin (*w/v*)	Gelma (*w/v*)	Hydrogel characteristics
Ink 1	100%	-	-	-	-	-	F
Ink 2	100%	-	2	5	-	-	WG/F
Ink 3	50%	50%	2	5	-	-	WG/F
Ink 4	50%	50%	5	10	-	-	WG/F
Ink 5	50%	50%	10	20	-	-	WG/F
Ink 6	50%	50%	-	12	-	-	WG/F
Ink 7	50%	50%	-	24	-	-	WG/F
Ink 8	50%	50%	-	-	5%	-	F
Ink 9	75%	25%	-	-	5%	-	F
Ink 10	50%	50%	-	-	10%	-	G
Ink 11	75%	25%	-	-	10%	-	G
Ink 12	50%	50%	-	-	-	10%	G*
Ink 13	50%	50%	-	-	-	15%	G

F: Fluid solution; WG/F: Weak gel while in the Eppendorf, but fluid once extruded. G: Gel-like solution. G*= may need lower temperature to become gel.

A preliminary experiment was performed to assess the printability of various cell-free bioink formulation. The results show that PL is crosslinked with thrombin and/or calcium, however, the pressure applied during the extrusion process irreversibly disrupt the fibrin network. Therefore, gelatin or GelMA was added to improve its extrudability.

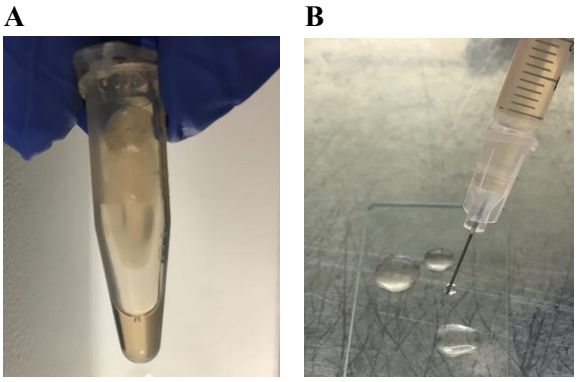

Figure 2.6 Platelet lysate gel crosslinked with calcium and thrombin.
(A) The non-homogeneous PL crosslinked gel (B) lost its consistency once extruded.

PL-gelatin formulation containing 10% of gelatin allowed appropriate filament deposition, however post-crosslinking with calcium and/or thrombin (Table 2.1) was not strong enough to hold the structure after 10 min at 37^{o}C. Gelatin methacryloyl (GelMa) was then incorporated into the PL bioink, it not only allowed appropriate filament deposition during extrusion but also enabled irreversible crosslinking through UV light. Because of that, the formulation containing PL and GelMA (PLGMA) was chosen for the following experiments.

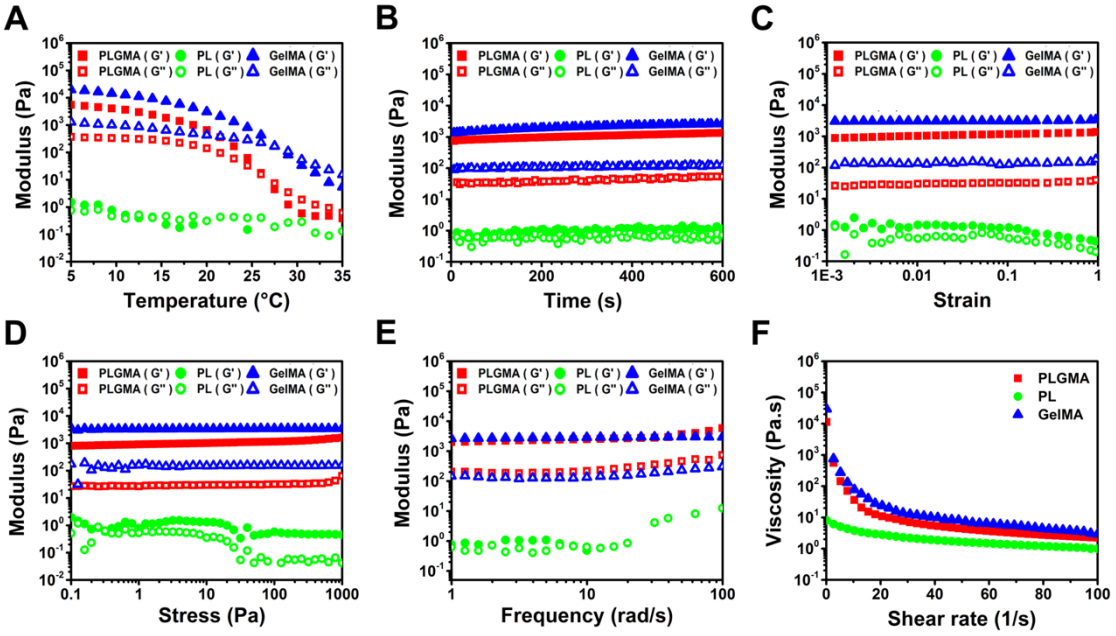

Figure 2.7 Oscillatory and rotational rheological behavior of PLGMA.
(A) Oscillatory temperature sweep from 35°C to 5°C showing modulus (Pa) as function of temperature (°C). (B) Time sweep up to 10 minutes showing modulus (Pa) as function of time. (C) Strain sweep from 0.01-1 showing modulus (Pa) as function of strain. (D) Stress sweep from 0.1 to 1000 showing modulus (Pa) as function of stress. (E) Frequency sweep from 1 to 100Hz showing modulus (Pa) as function of frequency. (F) Rotational steady state flow showing viscosity as a function of shear rate (1/s).

Oscillatory and rotational rheological characterization (Figure 2.7) was performed with the cell-free PLGMA bioink to obtain an accurate analysis of the bioink behaviour and predict its printability. The PLGMA bioink sol-gel transition point was determined by a temperature sweep from 35°C to 5°C, when the storage modulus (G′) surpassed the loss modulus (G″) around 25°C (Figure 2.7A). Therefore, subsequent experiments were performed at 19°C (G′ > G″). Time dependent rheological properties were demonstrated by time sweep, showing G' and G" modulus was relatively stable over 600s, suggesting PLGMA does not undergo major structural rearrangement that would influence its

rheological behaviour within the period of 600 s (Figure 2.7B). The strain amplitude sweep (0.01 – 1) and stress sweep (0.1 – 1000) demonstrated the PLGMA possesses a large linear viscoelastic region (LVR), suggesting consistency and stability of the bioink even under higher deformations (Figure 2.7C&D). Frequency sweeps (0.1 – 100 Hz) shows that the PLGMA bioink exhibited gel-like behaviour, as indicated by parallel G′ and G″ modulus not influenced by this frequency range (Figure 2.7E). The rotational steady-state flow shows the apparent viscosity of PLGMA decreases with increasing shear rate, indicating the PLGMA bioink is a shear-thinning fluid also referred to as a pseudoplastic fluid (Figure 2.7F).

Overall, the PLGMA bioink formulation demonstrated a significant improvement in rheological performance in comparison to PL itself, yet similar behaviour in comparison to GelMA, which enables extrudability and the capacity of forming self-supporting layer. Based on the rheology data, a nozzle head temperature of 19^{o}C was selected for the fabrication of 3D printed PLGMA constructs to allow appropriate filament deposition during extrusion and printing, and the platform was cooled down to 15 °C to support shape fidelity. The printing pressure and speed was 2.6 bar and 10 mm s^{-1}, respectively.

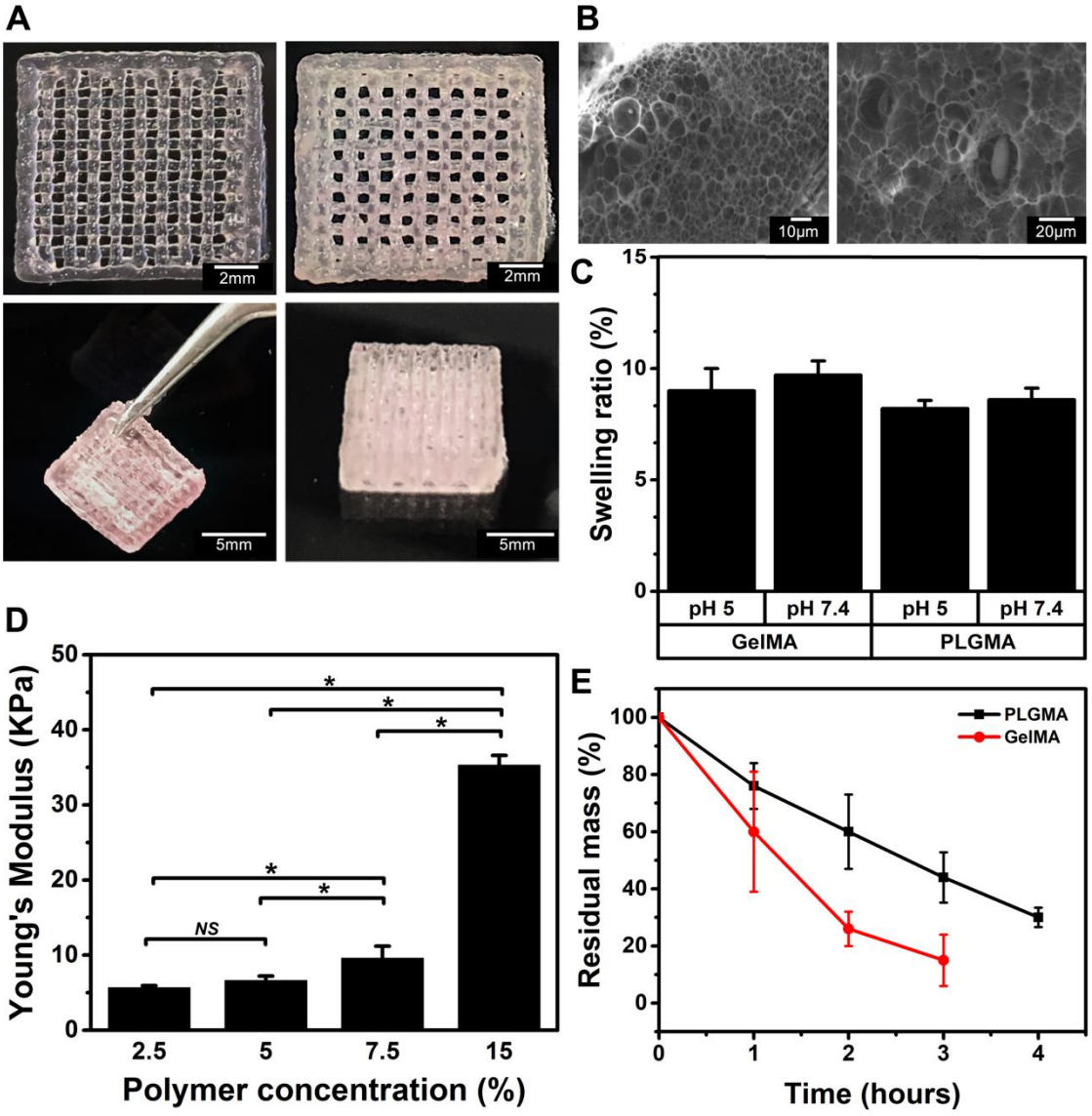

Figure 2.8 Physical and mechanical characteristics of the PLGMA printed construct. (A) Macroscopic view of the 3D printed lattice structure of the crosslinked PLGMA construct demonstrating good printability resolution and shape fidelity. (B) Cross-sectional SEM image of freeze-dried PLGMA construct at high magnifications showing heterogeneous microporous structure. (C) Swelling behaviour of cell-free PLGMA casted constructs after incubation in solutions solution pH 7.4 or pH 5. (D) Young's modulus of PLGMA construct as function of polymer concentration. (E) Accelerated enzymatic degradation of cell-free PLGMA constructs. (*) significant difference ($p < 0.05$), (NS) no statistically significant difference ($p \geq 0.05$).

Figure 2.8A shows a typical macroscopic view of the 3D printed cell-laden lattice structures using PLGMA, highlighting the successful stacking of multiple layers of PLGMA bioink along the z-direction with good shape fidelity. Printability index (*Pr*) of PLGMA constructs were found in the range of 0.9 - 1.1, demonstrating good shape fidelity and mechanical stability. The 3D printed constructs are easy to handle with retained structural integrity. Figure 2.8B illustrates the heterogeneous microporous structure of the freeze-dried PLGMA cross-section at high magnifications.

In order to investigate the effect of the environmental pH on the swelling behaviour of PLGMA constructs, swelling studies were performed by incubating PLGMA in PBS buffer with different pH (pH 5 and 7.4). PLGMA swelling ratio at pH 5 (8.2% ± 0.3) and pH 7.4 (8.6% ± 0.5) (Figure 2.8C). According to this data, PLGMA constructs showed swelling capacity which was not significantly influenced by environmental pH. Moreover, no significant difference between PLGMA and GelMA swelling behaviour was found, showing that the incorporation of PL into the bioink did not significantly change the mechanical properties of the PLGMA constructs when compared to the GelMA control group.

Figure 2.8D shows the Young's modulus of the cell-free PLGMA constructs (ranging from 5.6 ± 0.4 KPa to 35 ± 1.4 KPa), which can be modulated by varying the GelMA concentration (2.5%, 5%, 7.5% to 15% *w/v*). The PLGMA constructs were shown to be more resistant to enzymatic degradation in comparison to the GelMA control group (Figure 2.8E). PLGMA in PBS pH 7.4 without the presence of enzymes exhibited no significant degradation. PLGMA samples under the accelerated degradation conditions lost half of their mass at around 2.6 hours, while the GelMA control group lost half of

its mass at around 1.2 hours. The experiment was carried out for 4 hours as GelMA samples were extensively digested at that time point.

2.3.2 *In vitro* growth factor release

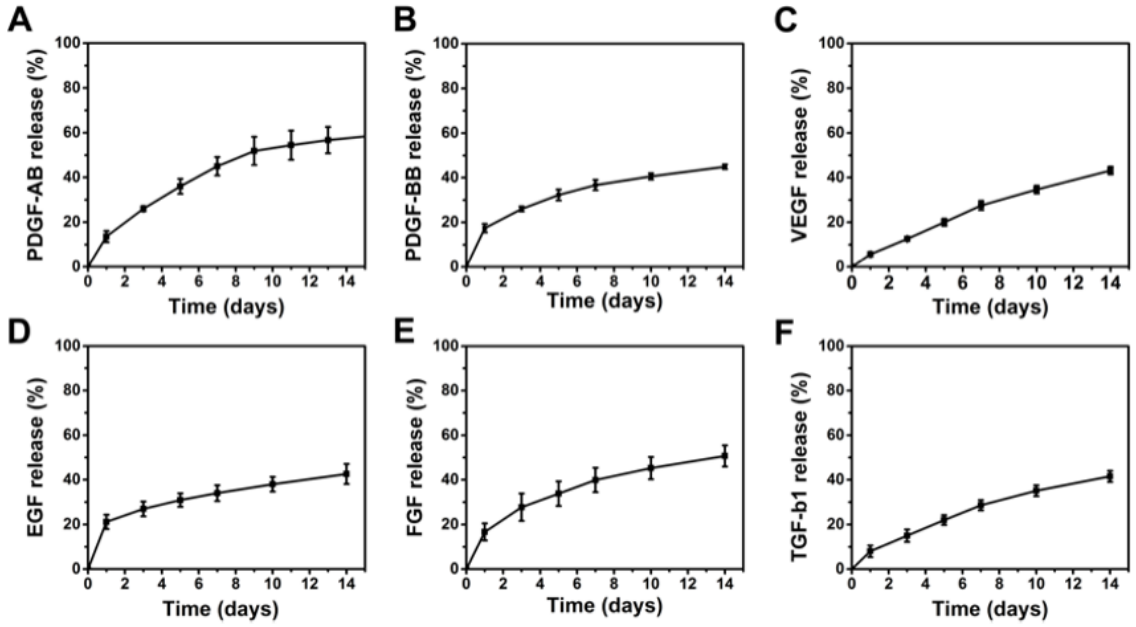

Figure 2.9 Growth factor release study from 3D printed cell-free PLGMA constructs. (A)-(F) Cumulative release profile of PDGF-αβ, PDGF-ββ, VEGF, EGF, FGF and TGF-β1 from the 3D printed PLGMA construct after 2 weeks of incubation. Mean ± SD; n >4. These growth factors were used as an indicator of the multiple factors and biologically relevant molecules released from 3D printed PLGMA.

Platelet lysate contains a large number of bioactive proteins, many of which have a fundamental role in haemostasis and tissue remodelling.[131] In this study, PDGF-αβ and -ββ, VEGF, EGF, FGF, and TGF were used as an indicator of the multiple factors and biologically relevant molecules present in the PL. The total concentration of PDGF-αβ and -ββ, VEGF, FGF, EGF and TGF-β1 in the PL used to fabricate PLGMA constructs measured approximately 34 ng/mL, 17 ng/mL, 0.9 ng/mL, 0.03 ng/mL, 1.5

ng/mL and 80 ng/mL, respectively. The overall encapsulation efficiency for each GF was approximately 85%. After crosslinking, samples were washed in PBS to remove non-crosslinked polymer and GFs, therefore non-crosslinked GFs lost in the first instance were not considered in the calculation of release studies.

Figure 2.9 (A-F) shows the cumulative release profiles of PDGF-αβ (56% ± 6), PDGF-ββ (45% ± 1), VEGF (43% ± 2), EGF (42% ± 4), FGF (51% ± 5) and TGF-β1(43% ± 3) from the 3D printed construct over a period of 2 weeks. The data indicates that after two weeks of incubation, GFs were still not exhausted from the constructs, with an average of 46% of the total GFs being released. This finding suggests this platform could be used to retain and deliver GFs and other relevant molecules in a sustainable manner for more than 2 weeks under cell-free, non-enzymatic conditions.

2.3.3 Biological characterization

The influence of the PLGMA matrix on the viability, proliferation, and morphology of encapsulated HDFs was determined *in vitro* using printed HDF-laden PLGMA (HDF-PLGMA) constructs. A preliminary experiment was conducted to establish the optimal concentration of PL in the ink formulation for best biological performance towards HDFs. Bioink formulations containing different concentrations of PL (10, 25, 50, 75, 100% *v/v*) with constant concentration of GelMA (15% *w/v*) and LAP (0.06% *w/v*) were used to encapsulate HDFs (at a cell density of 1×10^6 cells/mL) (Figure 2.S2). All five casted HDF-PLGMA groups (10, 25, 50, 75, 100% *v/v*) showed high cell viability (≥ 96%) with no significant difference between groups ($p > 0.05$) in the first week of culture. Moreover, casted HDF-PLGMA groups containing 100%, 75% and 50% of PL also showed high proliferation rate (average of 2.5-fold increase following a week of culture), 25% of PL showed proliferation rate around 1.7-fold increase following a week of culture. Lastly, the group containing 10% of PL showed proliferation rate around 1.2-fold increase following a week of culture. Based on this data, the ink formulation

containing 50% PL was selected for the fabrication of 3D printed HDF-PLGMA constructs.

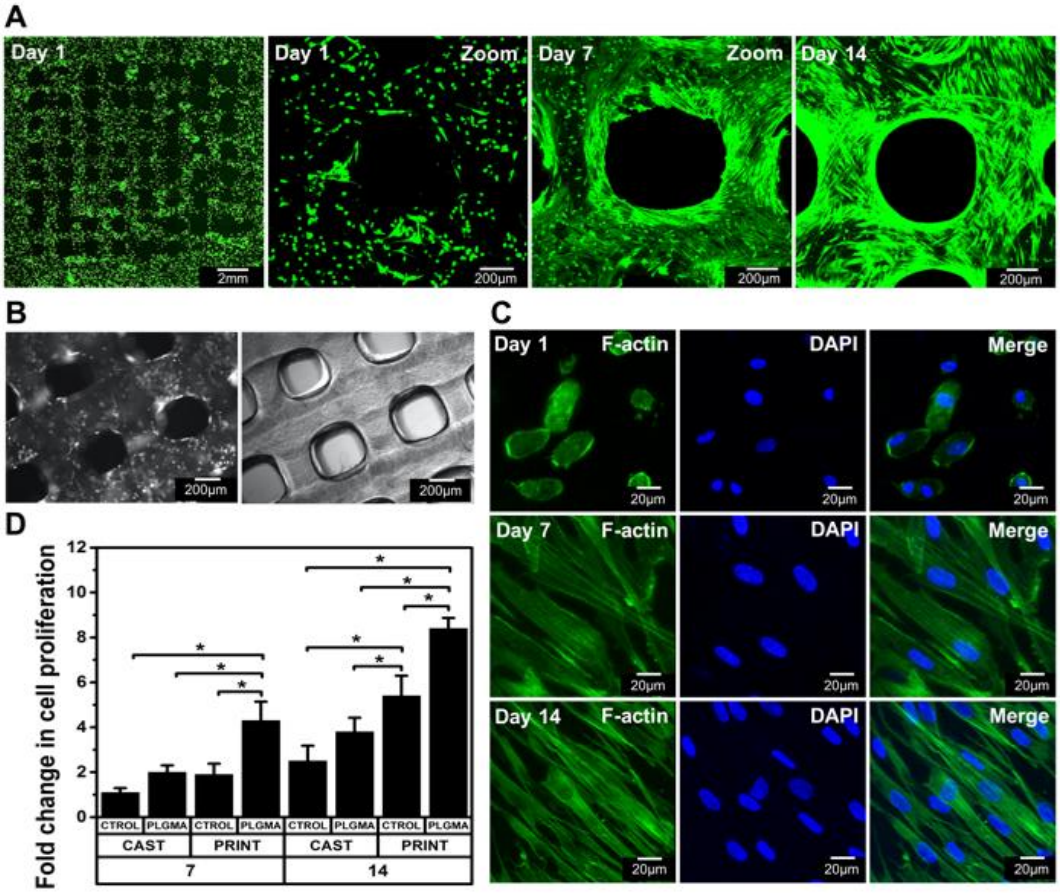

Figure 2.10 Assessment of 3D printed HDF-laden PLGMA viability, attachment and proliferation.

(A) Fluorescent Live/Dead staining images of 3D printed HDF-PLGMA construct at 3 time points. (B) Bright field image showing spatial arrangement and morphology of the 3D printed HDF-PLGMA cultured for 3 days. (C) Fluorescent images from actin filaments visualized with phalloidin staining of 3D printed HDF-PLGMA. (D) PrestoBlue assay showing fold change in cell proliferation of 3D printed HDF-PLGMA (Print-PLGMA) in comparison to casted HDF-PLGMA (Cast-PLGMA), casted HDF-GelMA control group (Cast-Ctrol) and printed HDF-GelMA control group (Print-Ctrol) after 7 and 14 days of culture. Scale bars as indicated.

2.3.4 ECM deposition by HDF

Printed and casted HDF-laden GelMA (HDF-GelMA) were used as a control since GelMA hydrogels have been widely used in 3D cell culture. Live/dead confocal imaging (Figure 2.10A) showed high viability (≥ 96%) of the 3D printed HDF-PLGMA after 24 hours of encapsulation (Figure 2. S5), which was then maintained for over 2 weeks of culture. The printed HDF-GelMA control group also showed high viability (≥ 93%). The cell distribution and morphology of the printed HDF-PLGMA after 3 days of culture is also demonstrated through bright field microscope images in Figure 2.10B. Moreover, high confluency of an elongated spindle-like shaped fibroblast sub-population (printed HDF-PLGMA) after just a week of culture demonstrates the cells were attaching and thriving well in the matrix. This was confirmed by F-actin staining (Figure 2.10C), which showed the change in cell cytoskeleton by the assembly and reorganization of actin filaments from a random orientated network of short filaments at day 1 to long parallel actin filaments that were arranged into tight bundles extending across the cell body from day 7 to 14. In accordance to these findings, a significantly higher level of HDF proliferation is observed in the printed HDF-PLGMA (Figure 2.10D) in comparison to the casted HDF-PLGMA group, as well as to the casted and printed HDF-GelMA control groups, with more than a 4-fold increase following one week of culture and an 8-fold increase following two weeks of culture. The ECM is a complex network consisting of structural proteins, collagens, laminins, elastin, fibronectins, proteoglycans and hyaluronan arranged in a highly organised manner, contributing to the strength and structural integrity of the tissue.[13] Here, some of the key ECM components – collagen I, collagen III, fibronectin and elastin – synthesised by fibroblasts during the wound healing process were studied to demonstrate the effect of

GFs present in the PLGMA constructs in supporting the deposition of ECM by HDF. Fluorescent immunohistochemistry staining and SYBR Green RT-PCR assay demonstrated that the GFs in the PLGMA matrix were bioactive and stimulated ECM protein synthesis. The fluorescent staining images (Figure 2.11A) shows immunohistochemical expression of fibrillar collagen type I and type III, elastin and fibronectin markers deposited by printed HDF-PLGMA after 14 days of culture. All our markers show organisation, especially collagen type I, which exhibited well defined fibres oriented in parallel. Figure 2.11B shows a comparison of the relative quantification of collagen type I and type III, elastin and fibronectin based on the expression of these macromolecules in 3D printed HDF-PLGMA and HDF-GelMA relative to 2D HDFs, normalised to the housekeeping gene GAPDH. Higher expression of collagen I, collagen III, fibronectin and elastin were found in 3D printed HDF-PLGMA in comparison with 3D printed HDF-GelMA control group, but only type I and type III collagen showed significant differences. Briefly, GFs present in the PLGMA

constructs showed a positive impact in the synthesis of ECM components by dermal fibroblasts cultured for 2 weeks.

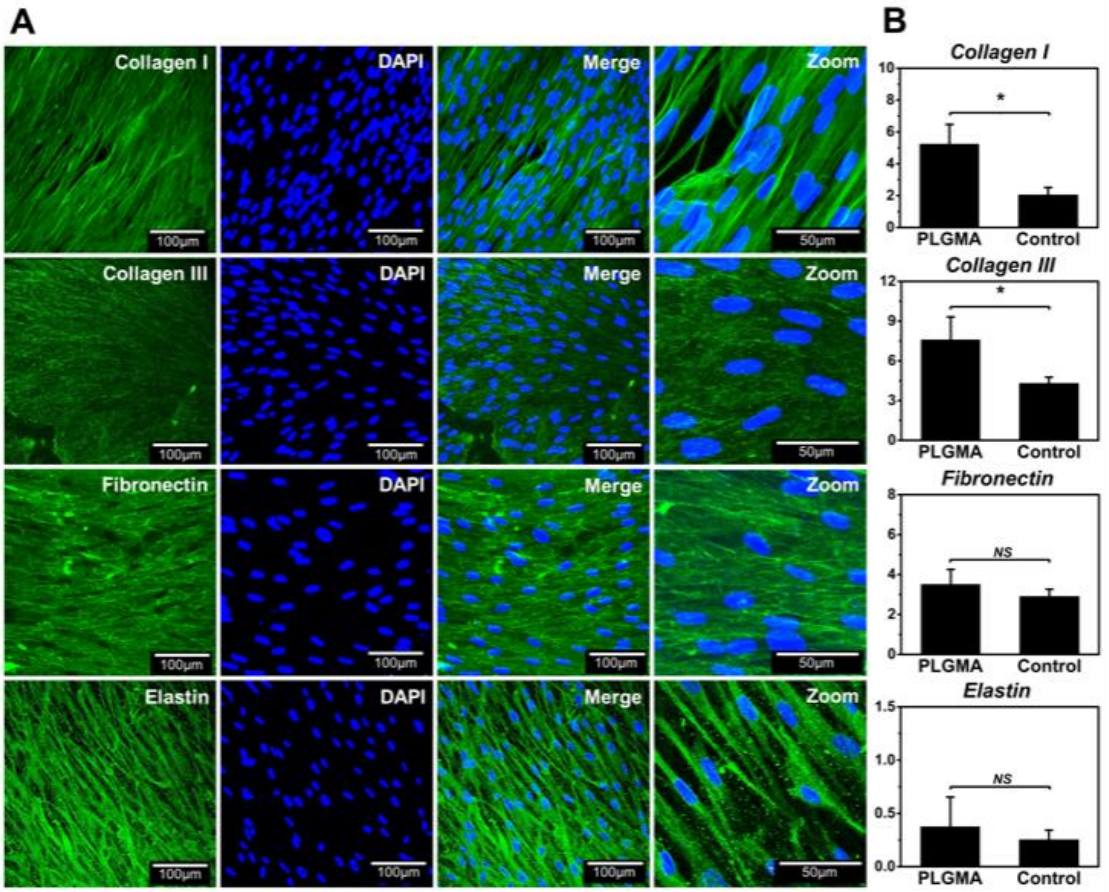

Figure 2.11 Assessment of ECM deposition by 3D printed HDF-PLGMA.
(A) Fluorescent images from immunohistochemical staining with polyclonal antibodies against type I collagen, type III collagen, fibronectin and elastin of 3D printed HDF-PLGMA constructs, respectively. Scale bars as indicated. (B) Relative gene expression of collagen I, collagen III, fibronectin and elastin from printed HDF-PLGMA construct in comparison with printed HDF-GelMA control group. Relative gene expression represents data normalized to GAPDH and expressed relative to 2D HDFs. Mean ± SD;

n >3. (*) significant difference ($p < 0.05$), (NS) no statistically significant difference ($p \geq 0.05$).

Cell and ECM organisation have a direct influence in the tissue remodelling capacity and healing potential. Random reorganisation of ECM during the healing process is linked to impaired tissue regeneration and abnormal scarring, which can lead to severe morbidity due to physical dysfunction and psychological stress.[13] Collagen type I, collagen type III, elastin and fibronectin fibres from 3D printed HDF-PLGMA constructs have shown a certain level of organization and alignment, which could have followed the cell alignment, influenced by the bioink shear and extensional flows during the extrusion process. Gene expression data further indicate the superior performance of 3D printed PLGMA in supporting the deposition of ECM components by the encapsulated HDFs compared to the GelMA control group, likely due to the presence of GFs and other relevant molecules in the PLGMA construct. Both GFs and the ECM have a dynamic interaction which is essential to all phases of the healing process. This interaction occurs in multiple ways and is bi-directional. The ECM regulates GF signalling dependent on ECM-GF binding, correspondingly, GFs modulate ECM deposition by stimulating cells to increase production of ECM components or regulating production of matrix-degrading proteases and their inhibitors.[165] Further research will enable better insight about the ECM and GF interaction and to answer if this particular ECM alignment would better assist the remodelling process and enhance tissue regeneration.

2.4 Discussion

The development of an extrusion-based bioink formulation derived from PL is described herein, which can be used to fabricate a 3D cell delivery system to simultaneously release GFs in a sustainable manner, while providing a supportive network that mimics the native ECM for skin cells to thrive. Ultimately, the PLGMA bioink's rheological behaviour was significantly improved in comparison to PL, whereupon the PLGMA constructs enabled sustained release of the GFs that are essential to wound healing, improved cell proliferation as well as ECM synthesis of the co-printed HDFs.

An ideal bioink should meet specific rheological characteristics appropriate to the printing method to be utilised. The printed structure should also provide optimal mechanical, chemical, and biological characteristics to support adequate cell networking, organization and function of the tissue.[166, 167] Platelet lysate is rich in fibrinogen and, in contact with thrombin and/or calcium, naturally forms a polymeric fibrin network.[168] This crosslinked fibrin network was previously shown to be unsuitable for an extrusion-based printing process due to a lack of robustness in the extruded structure.[169] Therefore, platelet derived products have been incorporated with other biomaterials to formulate a composite bioink which meet specific rheological characteristics appropriate to the printing method to be utilised. Faramarzi et al. [156] reported an alginate-based bioink incorporated with platelet-rich plasma (PRP) for application in musculo-skeletal and cardiovascular tissue engineering. Mendes et al. [157] reported a bioink composed of platelet lysate hydrogels reinforced by cellulose nanocrystals for development of xeno-free 3D tissue models.

In this study, GelMA was added to improve the bioink extrusion performance. GelMA is a denatured type of collagen that has been widely used as a versatile matrix for tissue engineering scaffolds.[121-124] GelMA hydrogels exhibit remarkable tunable mechanical, degradation and swelling properties, which makes them ideal candidates for skin tissue engineering.[124] GelMA's inherent thermo-responsive characteristics and pseudoplastic behaviour facilitate filament deposition during the extrusion process and reduce nozzle-clogging,[125] whilst protecting cells against excessive shear stress.[126] Moreover, its photo-crosslinkable methacryloyl groups enable irreversible shape fixation of the final printed construct.[127] LAP is a photoinitiator commonly used in bioprinting and it was also added to the ink formulation at a final concentration of 0.06% *w/v* because several studies have reported that low LAP concentration enabled high viability during direct encapsulation of cells.[170-172]

The study of the physico-mechanical properties of tissue engineered scaffolds is crucial to better mimic native tissue, thereby strengthening cell attachment and proliferation to achieve complete wound repair.[160] Figure 3A shows the macroscopic final 3D printed PLGMA construct demonstrating that the optimised formulation provided desirable extrudability, printing accuracy and shape fidelity. The stacking of multiple layers of PLGMA bioink was also demonstrated to show this system could be potentially used to fabricate a skin equivalent for various wound depth. The mechanical property of the PLGMA constructs are readily tuned to mirror the broad range of elasticity found in native skin (10^4 - 10^6 Pa).[173-176] For this project, PLGMA containing 15% *w/v* GelMA was chosen to fabricate fibroblast-laden constructs because its mechanical properties are equivalent to the skin dermal layer[177] (~35 KPa).

Here, accelerated enzymatic degradation assay was performed to investigate the differences in degradation profile of PLGMA and GelMA. Lima et al. previously described the incorporation of platelet lysate increased the resistance of collagen gel beads towards collagenase degradation. [178] In accordance with this report, our data revealed PLGMA constructs exhibited improved resistance to enzymatic breakdown in comparison to GelMA constructs. This improvement in stability could be attributed to the reinforcement of the GelMA structure by a fibrin mesh. An ideal biocompatible and biodegradable platform for wound healing application needs to follow the dynamics of the wound repair matching its degradability rate to the timeline of the healing process. Therefore, although improved stability was demonstrated in vitro, further investigation is needed to confirm PLGMA stability in vivo and its suitability as a skin tissue engineering substitute.

Upon injury, skin get exposed to internal fluids which have physiological pH (7.4) and the slightly acidic environment (pH 4–6) of a healthy skin then change to a more basic one (6.5–8.5).[179] Therefore, swelling studies were performed at pH 5 and 7.4 to model change in the pH of the wound environment. High water uptake ability is a desirable characteristic of a biosynthetic skin substitute. The ability to maintain a moist environment and adsorb wound exudate has been reported to promote fibroblast proliferation and keratinocyte migration, which is important for complete regeneration of the wound.[180] Hydrogel-based dressings, due to their water-soluble nature, have several reported advantages including maintaining optimal moist conditions, permeating oxygen, clearing debris, as well as protecting the wound from infection and contamination. [179] PLGMA constructs, which are a hydrogel-based system, were shown to have a good affinity toward the aqueous media and their swelling capability

was not significantly affected by the range of pH tested. Wound infection may influence the wound pH and result in delayed and even impaired healing. Platelet derived products have been reported to have antimicrobial properties against several pathogens commonly associated with wound infections [181, 182] Therefore, further studies demonstrating antimicrobial activity of PLGMA constructs against common airborne bacteria as well as in vivo swelling and degradation studies will also be performed

Human-recombinant GFs are available in a purified form; however, tissue regeneration cannot be effectively triggered by a single agent.[71] The additive and/or synergistic effect of a combination of GFs on the proliferation, migration and differentiation of various cell types both in vitro and in vivo, has been reported to lead to enhanced healing efficacy.[183] The use of multiple recombinant factors as therapeutic agents, on the other hand, has been hindered by their safety, high production cost, low stability and short half-life. For instance, FGF-1 has been shown to have low stability, with a short active half-life of 1h in serum at 37 °C, whereas the half-life of bFGF is 3 minutes and that of VEGF is about 50 minutes following intravenous injection.[184]

Platelet lysate is a suitable, abundant and cost-effective source of GFs.[185] The commercial PL used in this work was manufactured from platelet units obtained from healthy blood donors at European Medicines Agency (EMA)-licensed blood centres to minimize batch-to-batch variation, nevertheless PL can be obtained from an autologous source and implemented in a customisable and personalised approach.[131] We studied the cumulative release of PDGF, VEGF, FGF, EGF and TGF-β1 from 3D printed PLGMA over a 2-week period. The *in vitro* study confirmed that about 50% of the payload was released for each GF from the PLGMA construct after 14 days in cell-free conditions (without enzymatic degradation). The retention of growth factors in PLGMA

constructs was greater than that reported for a fibrin-based scaffold loaded with platelet lysate[186] or hydroxybutyl chitosan hydrogels loaded with platelet lysate growth factors.[186] Since PL was directly incorporated into the bioink formulation without any further modification, the retention of growth factors and other molecules could be potentially attributed to the mechanical and physical properties of the polymer in the bioink, and electrostatic interactions between growth factors and matrix.[187]

The effectiveness of GF therapy for regenerative medicine applications is largely dependent on preserving bioactivity during fabrication and application.[188] Therefore, the bioactivity of the GFs from 3D printed PLGMA construct were assessed in vitro using human dermal fibroblasts, the predominant cell line of the cutaneous dermal layer. In conventional tissue engineering approaches, cells are seeded into a cellular scaffold, which makes it difficult to control their spatial distribution throughout the matrix.[160]

Bioprinting allows spatially controlled distribution of biomaterials, biological molecules and living cells to generate complex 3D microenvironments. In addition, this technique also enables more flexibility with the design and introduction of macropores to the final construct.[189] Figure 2.10A and B show that by encapsulating HDF into the bioink formulation, it was possible to obtain a homogeneous distribution of cells throughout the printed matrix. Since the proposed platform should deliver fibroblasts and GFs, while supporting and guiding cell ingrowth, in vitro cytocompatibility against fibroblasts was demonstrated as well as the potential to be used as a 3D cell culture substrate for cell expansion, and ECM formation.

The stimulating effects of PL growth factors on cell growth and on the synthesis of ECM has been previously demonstrated in a 2D setting using pancreatic stellate cells

(PSC),[190] and more recently in a 3D printed setting using human adipose-derived stem cells (hASCs).[157] In accordance to these reports, immobilized GFs from the PLGMA constructs also promoted high cytocompatibility towards fibroblasts, supporting enhanced cell viability, adhesion, metabolic activity and stimulating the synthesis of new ECM by fibroblast. The improved proliferation of the 3D printed HDF-PLGMA compared to the ones in cast PLGMA could be attributed to its lattice structure. The increased interfacial surface area of the printed construct facilitates the diffusion of nutrients and exchange of gases,[191] improving cell proliferation and migration to the surface of the printed strands. Taken together, these data suggest that PLGMA bioink provides a strong foundation for the fabrication of multifunctional platform for wound management and tissue regeneration. Nevertheless, further investigation in vitro and in vivo are needed to determine the effectiveness of the system to co-deliver fibroblasts and GFs to the wound site, while protecting cells from acute inflammatory environments and GFs from excessive enzymatic degradation as well as its potential to guide the new tissue formation. Future studies will also involve the incorporation of other relevant cells for skin tissue regeneration.

Fibroblasts provides the physical integrity of connective tissue by producing and remodelling ECM components. During the healing process, fibroblast secrete structural ECM components, such as elastin, procollagen, proteoglycans, and hyaluronic acid (HA), involved in the formation of granulation tissue. The granulation tissue enables infiltration of inflammatory cells to the wound site and ingrowth of new blood vessels for nutrition and oxygen of the newly formed tissue. Fibronectin regulates the neovascularization of granulation tissue and mediates collagen I/III fibrillar network formation. Collagens are the main structural component of the ECM. [13] Collagen type

I and III are the dominant type of collagen in cutaneous wound repair. Collagen I/III proportion varies throughout different depths of the dermis and different stages of the healing process. [12] During the early stages of the granulation tissue formation, fibroblasts secrete primarily collagen type III leading to an increased expression of collagen type III compared to type I, the ratio decreases again to normal levels in late stages of the healing process. Abnormal changes of its normal expression is implicated in fibrosis or hypertrophic scarring.[13] Moreover, type III collagen has been reported to play a prominent role in cutaneous wound repair modulating scar tissue formation and preventing impaired healing.[192] Our data revealed the remarkable capacity of fibroblast cultured into PLGMA constructs to deposit ECM molecules. Additionally, higher expression of collagen type III than collagen I by HDF-PLGMA demonstrated the potential to emulate early stages of granulation tissue formation and provide support for future investigation of capacity of the HDF-PLGMA platform to improve tissue regeneration.

Cell and ECM organisation have a direct influence in the tissue remodelling capacity and healing potential. Random reorganisation of ECM during the healing process is linked to impaired tissue regeneration and abnormal scarring, which can lead to severe morbidity due to physical dysfunction and psychological stress.[13] Collagen type I, collagen type III, elastin and fibronectin fibres from 3D printed HDF-PLGMA constructs have shown a certain level of organization and alignment, which could have followed the cell alignment, influenced by the bioink shear and extensional flows during the extrusion process. Gene expression data further indicate the superior performance of 3D printed PLGMA in supporting the deposition of ECM components by the encapsulated HDFs compared to the GelMA control group, likely due to the presence of

GFs and other relevant molecules in the PLGMA construct. Both GFs and the ECM have a dynamic interaction which is essential to all phases of the healing process. This interaction occurs in multiple ways and is bi-directional. The ECM regulates GF signalling dependent on ECM-GF binding, correspondingly, GFs modulate ECM deposition by stimulating cells to increase production of ECM components or regulating production of matrix-degrading proteases and their inhibitors.[165] Further research will enable better insight about the ECM and GF interaction and to answer if this particular ECM alignment would better assist the remodelling process and enhance tissue regeneration.

2.5 Conclusion

Platelet lysate (PL) is an attractive source of GFs that play an important role orchestrating the healing cascade. Despite GFs inherent potential for regenerative medicine, the paucity of efficient delivery systems limits their use in the clinic. Herein, we have established a composite PL and GelMA bioink formulation (PLGMA) for the fabrication of multifunctional skin equivalent platforms, which shows promise in several aspects of skin tissue engineering, including high cytocompatibility towards HDF, as well as promoting cell attachment and proliferation. Further benefits of this system include increased synthesis and deposition of ECM molecules. By combining bioprinting technology with 'smart' functional bioinks, it is possible to offer superior customizable solutions for patients with complex wounds in the future, overcoming various limitations faced in tissue engineering and regenerative medicine. Although more in-depth assessment to proof the proposed PLGMA platform therapeutical efficacy in supporting skin tissue regeneration are currently underway, the present work aimed to establish a foundation towards the development of a more complex skin equivalent with complete functional performance.

Supporting Information

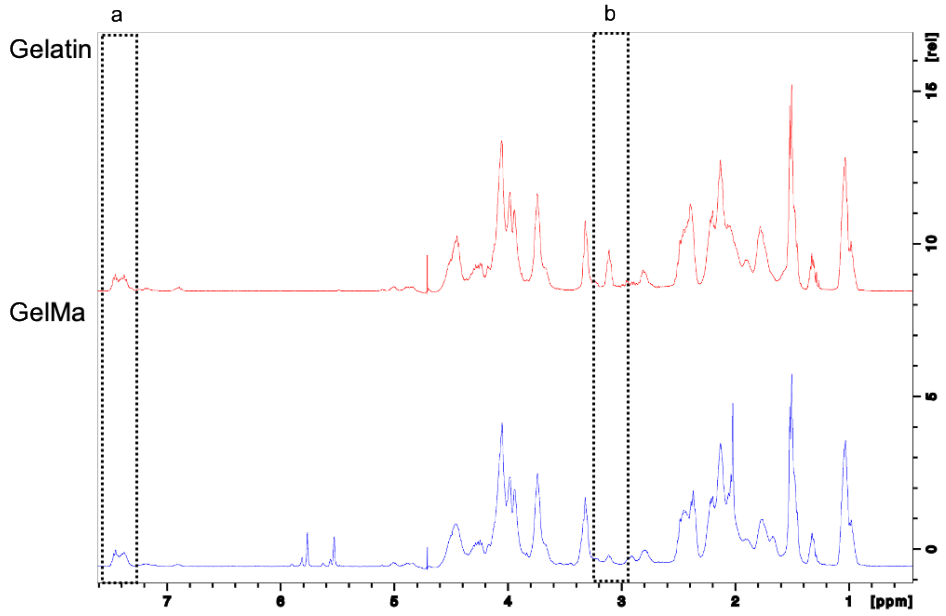

Figure 2.S 1^{1}H NMR spectra of GelMA and unmodified Gelatin.

The lysine methylene peak (2.8 – 3.0 ppm) (b) was used to confirm the methacrylation degree as lysine is the bonding site for methacryloyl conjugation, while the phenylalanine peak (7.3 – 7.5 ppm) (a) was used to normalize the intensity of the lysine peak. Therefore, the degree of functionalization was calculated by comparing the proton signal (2.8 – 3.0 ppm) of unmodified gelatin (red) and GelMA (blue spectra).

Table 2.S 1List of primers used for real time RT-PCR

Gene	**Primer sequence (5'-3')**
GAPDH	F: ATGGAAATCCCATCACCATCTT
	R: CGCCCCACTTGATTTTGG
Collagen I	F: GGGAACGCGTGTCAATCC
	R: CAGTTACACAAGGAACAGAACAGTCTCT
Collagen III	F: TGGTCAGTCCTATGCGGATAGA
	R: CGGATCCTGAGTCACAGACACA
Fibronectin	F: TCGCCATCAGTAGAAGGTAGCA
	R: TGTTATACTGAACACCAGGTTGCAA
Elastin	F: CTAAATACGGTGCTGCTGGC
	R: CATGGGATGGGGTTACAAAG

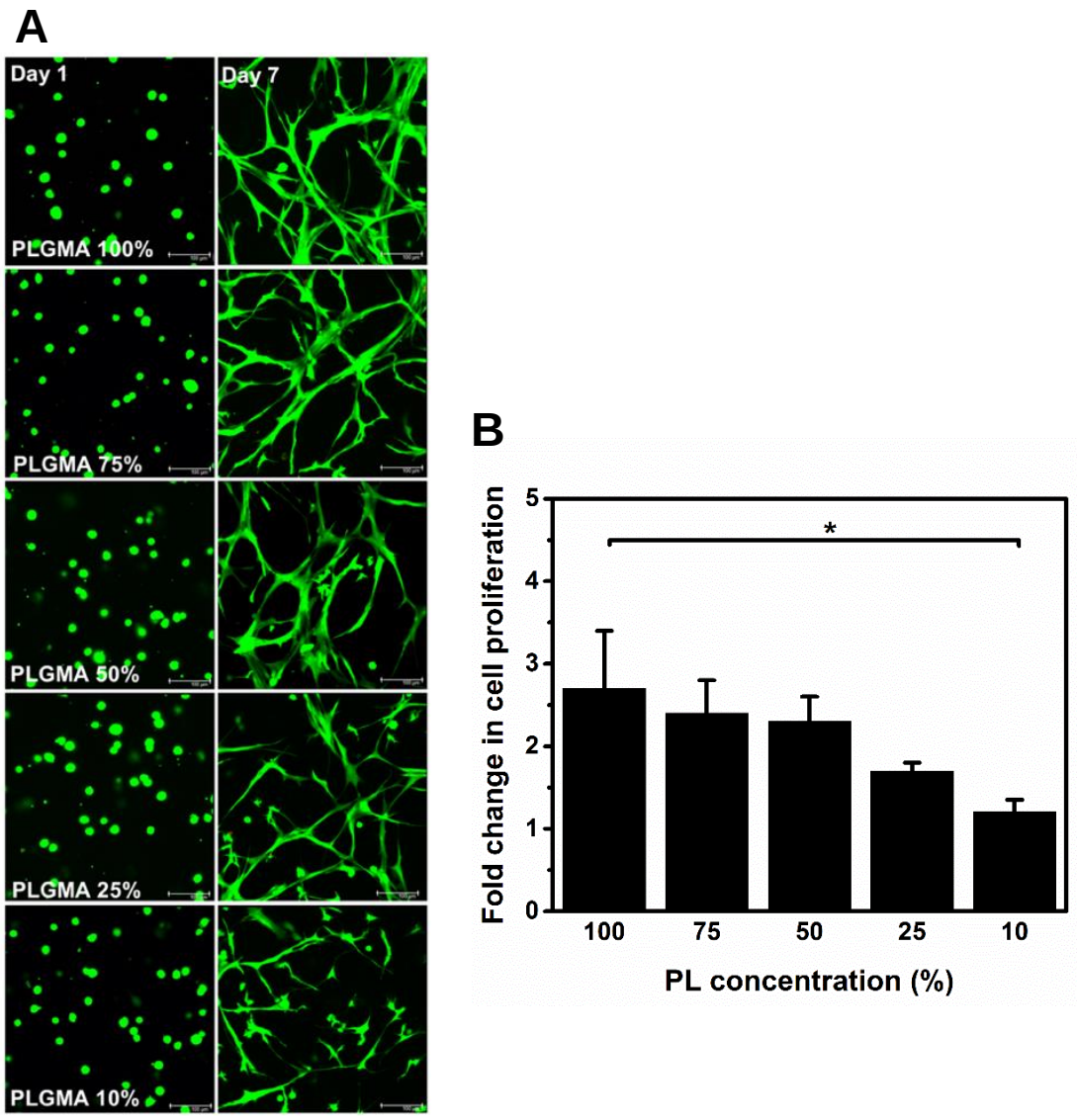

Figure 2.S 2 Preliminary assessment of viability and proliferation of HDF-PLGMA formulated with different concentrations of PL.

(A) Fluorescent Live/Dead staining images of HDF-PLGMA constructs at day 1 and day 7 of culture. Scale bars as indicated (100μm). (B) PrestoBlue assay showing fold change in cell proliferation of casted HDF-PLGMA containing different PL concentration cultured for a week.

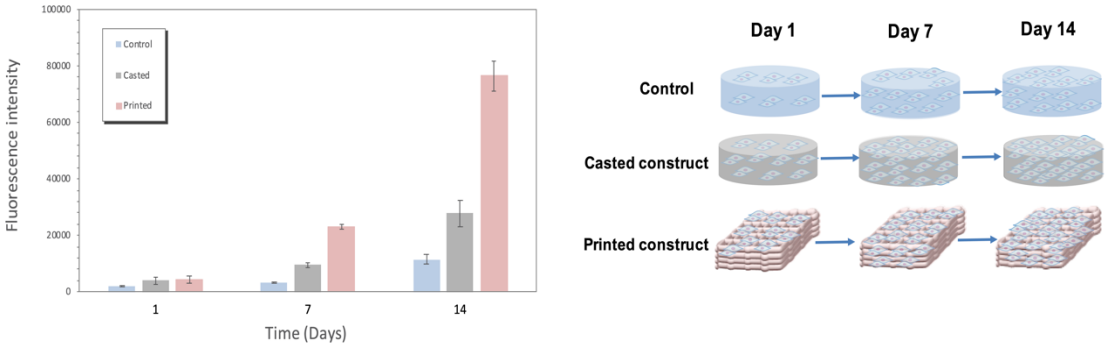

Figure 2.S 3 Preliminary assessment of proliferation – printed and casted PLGMA. PrestoBlue assay showing proliferation of HDF encapsulated in three experimental groups: casted PLGMA, printed PLGMA and GelMA control after cultured for up to two weeks. Data was collected at 3 time points (day 1, 7 and 14) and read at fluorescence intensity at 544/590nm. The rich microenvironment of the PLGMA casted and printed groups promoted significantly higher proliferation in comparison to the GelMa control group. Moreover, the porous 3D printed PLGMA structure leaded to the highest cell proliferation among the groups tested.

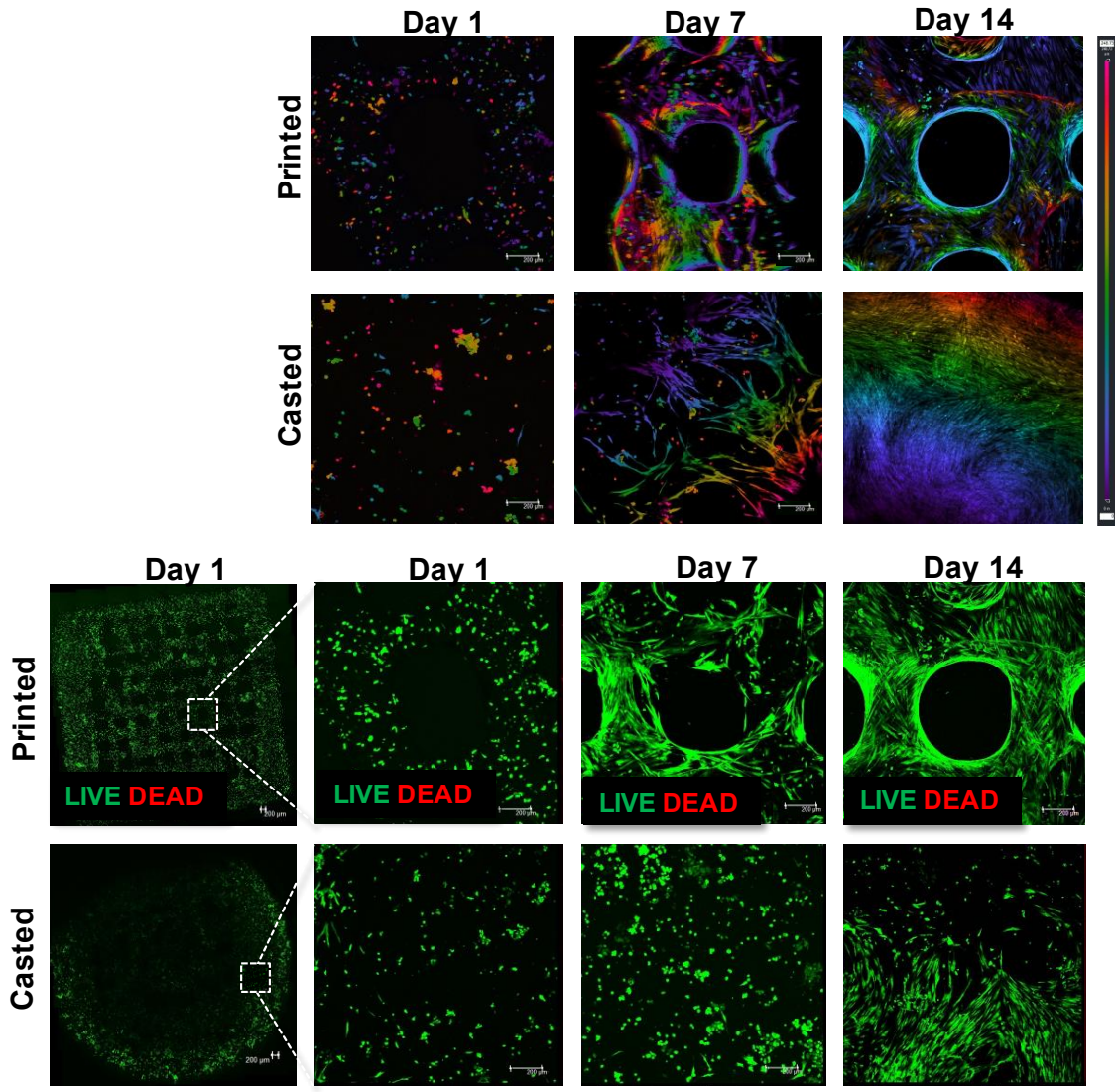

Figure 2.S 4 Preliminary assessment of viability - printed and casted PLGMA.

Fluorescent Live/Dead staining images shows viability of HDF encapsulated into printed and casted PLGMA constructs after cultured for up to two weeks. Images were acquired using laser confocal fluorescence microscopy (Leica TSC SP5 II). Color-coded depth images show the distribution of HDF in a 3D space (purple 0μm to pink 248μm)

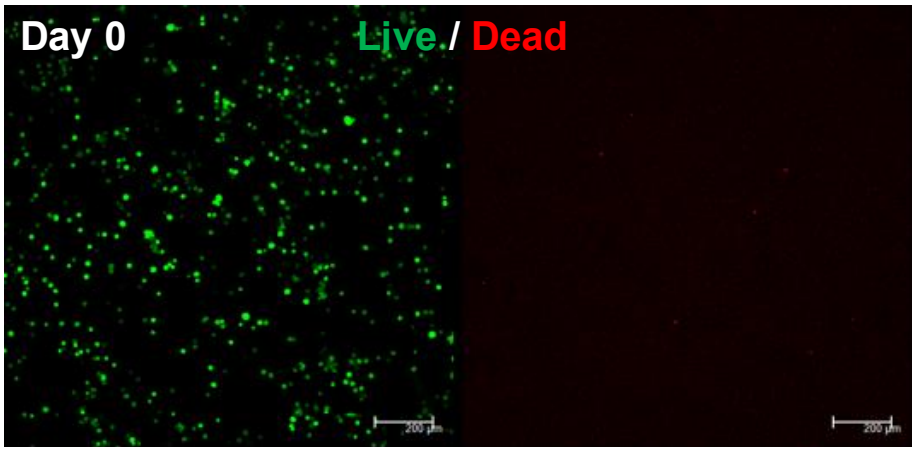

Figure 2.S 5 Live/Dead staining images of 3D printed HDF-PLGMA construct at day 0 (3 hours after printing). Scale bars as indicated (200µm).

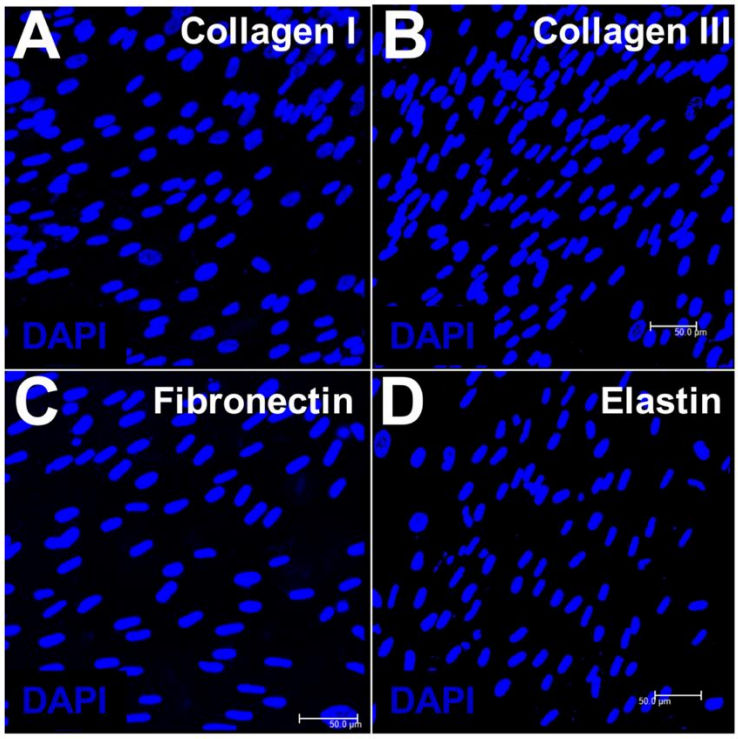

Figure 2.S 6 Images of the negative controls from the immunohistochemical staining of polyclonal antibodies against type I collagen, type III collagen, fibronectin and elastin of 3D printed HDF-PLGMA constructs. Figure shows only DAPI staining. Scale bars as indicated (50µm).

2.6 References

[12] L.E. Tracy, R.A. Minasian, E.J. Caterson, Extracellular Matrix and Dermal Fibroblast Function in the Healing Wound, Adv Wound Care (New Rochelle) 5(3) (2016) 119-136.

[13] M. Xue, C.J. Jackson, Extracellular Matrix Reorganization During Wound Healing and Its Impact on Abnormal Scarring, Adv Wound Care (New Rochelle) 4(3) (2015) 119-136.

[61] J.W. Park, S.R. Hwang, I.S. Yoon, advanced growth factor delivery systems in wound management and skin regeneration, Molecules 22(8) (2017).

[71] G. Sandri, M.C. Bonferoni, S. Rossi, F. Ferrari, M. Mori, C. Del Fante, C. Perotti, C. Caramella, Thermosensitive eyedrops containing platelet lysate for the treatment of corneal ulcers, Int J Pharm 426(1-2) (2012) 1-6.

[121] K. Yue, G. Trujillo-de Santiago, M.M. Alvarez, A. Tamayol, N. Annabi, A. Khademhosseini, Synthesis, properties, and biomedical applications of gelatin methacryloyl (GelMA) hydrogels, Biomaterials 73 (2015) 254-71.

[122] L. Kessler, S. Gehrke, M. Winnefeld, B. Huber, E. Hoch, T. Walter, R. Wyrwa, M. Schnabelrauch, M. Schmidt, M. Kückelhaus, M. Lehnhardt, T. Hirsch, F. Jacobsen, Methacrylated gelatin/hyaluronan-based hydrogels for soft tissue engineering, J Tissue Eng 8 (2017) 2041731417744157-2041731417744157.

[123] S. Xiao, T. Zhao, J. Wang, C. Wang, J. Du, L. Ying, J. Lin, C. Zhang, W. Hu, L. Wang, K. Xu, Gelatin Methacrylate (GelMA)-Based Hydrogels for Cell Transplantation: an Effective Strategy for Tissue Engineering, Stem Cell Reviews and Reports 15(5) (2019) 664-679.

[124] X. Zhao, Q. Lang, L. Yildirimer, Z.Y. Lin, W. Cui, N. Annabi, K.W. Ng, M.R. Dokmeci, A.M. Ghaemmaghami, A. Khademhosseini, Photocrosslinkable Gelatin Hydrogel for Epidermal Tissue Engineering, Advanced healthcare materials 5(1) (2016) 108-118.

[125] J.K. Carrow, P. Kerativitayanan, M.K. Jaiswal, G. Lokhande, A.K. Gaharwar, Chapter 13 - Polymers for Bioprinting, in: A. Atala, J.J. Yoo (Eds.), Essentials of 3D Biofabrication and Translation, Academic Press, Boston, 2015, pp. 229-248.

[126] N.E. Fedorovich, W. Schuurman, H.M. Wijnberg, H.J. Prins, P.R. van Weeren, J. Malda, J. Alblas, W.J. Dhert, Biofabrication of osteochondral tissue equivalents by

printing topologically defined, cell-laden hydrogel scaffolds, Tissue Eng Part C Methods 18(1) (2012) 33-44.

[127] I. Pepelanova, K. Kruppa, T. Scheper, A. Lavrentieva, Gelatin-Methacryloyl (GelMA) Hydrogels with Defined Degree of Functionalization as a Versatile Toolkit for 3D Cell Culture and Extrusion Bioprinting, Bioengineering 5(3) (2018) 55.

[131] K. Plöderl, C. Strasser, S. Hennerbichler, A. Peterbauer-Scherb, C. Gabriel, Development and validation of a production process of platelet lysate for autologous use, Platelets 22(3) (2011) 204-209.

[147] L. Mazzucco, D. Medici, M. Serra, R. Panizza, G. Rivara, S. Orecchia, R. Libener, E. Cattana, A. Levis, P.G. Betta, P. Borzini, The use of autologous platelet gel to treat difficult-to-heal wounds: a pilot study, Transfusion 44(7) (2004) 1013-1018.

[148] R.E. Backly, V. Ulivi, L. Tonachini, R. Cancedda, F. Descalzi, M. Mastrogiacomo, Platelet Lysate Induces In Vitro Wound Healing of Human Keratinocytes Associated with a Strong Proinflammatory Response, Tissue Engineering Part A 17(13-14) (2011) 1787-1800.

[149] S. Rossi, A. Faccendini, M.C. Bonferoni, F. Ferrari, G. Sandri, C. Del Fante, C. Perotti, C.M. Caramella, “Sponge-like” dressings based on biopolymers for the delivery of platelet lysate to skin chronic wounds, International Journal of Pharmaceutics 440(2) (2013) 207-215.

[150] D. Badis, B. Omar, The effectiveness of platelet-rich plasma on the skin wound healing process: A comparative experimental study in sheep, Vet World 11(6) (2018) 800-808.

[151] A. Oryan, S. Alidadi, A. Moshiri, Platelet-rich plasma for bone healing and regeneration, Expert Opinion on Biological Therapy 16(2) (2016) 213-232.

[152] M.I. Kennedy, K. Whitney, T. Evans, R.F. LaPrade, Platelet-Rich Plasma and Cartilage Repair, Curr Rev Musculoskelet Med 11(4) (2018) 573-582.

[153] F. Arnalich, A.E. Rodriguez, A. Luque-Rio, J.L. Alio, Solid Platelet Rich Plasma in Corneal Surgery, Ophthalmol Ther 5(1) (2016) 31-45.

[154] M.M. Murray, K.P. Spindler, E. Abreu, J.A. Muller, A. Nedder, M. Kelly, J. Frino, D. Zurakowski, M. Valenza, B.D. Snyder, S.A. Connolly, Collagen-platelet rich plasma hydrogel enhances primary repair of the porcine anterior cruciate ligament, Journal of Orthopaedic Research 25(1) (2007) 81-91.

[155] A.C. Lima, J.F. Mano, A. Concheiro, C. Alvarez-Lorenzo, Fast and Mild

Strategy, Using Superhydrophobic Surfaces, to Produce Collagen/Platelet Lysate Gel Beads for Skin Regeneration, Stem Cell Reviews and Reports 11(1) (2015) 161-179.
[156] N. Faramarzi, I.K. Yazdi, M. Nabavinia, A. Gemma, A. Fanelli, A. Caizzone, L.M. Ptaszek, I. Sinha, A. Khademhosseini, J.N. Ruskin, A. Tamayol, Patient-Specific Bioinks for 3D Bioprinting of Tissue Engineering Scaffolds, Adv Healthc Mater 7(11) (2018) e1701347.
[157] B.B. Mendes, M. Gomez-Florit, A.G. Hamilton, M.S. Detamore, R.M.A. Domingues, R.L. Reis, M.E. Gomes, Human platelet lysate-based nanocomposite bioink for bioprinting hierarchical fibrillar structures, Biofabrication 12(1) (2019) 015012.
[158] S.M. Oliveira, R.L. Reis, J.F. Mano, Assembling Human Platelet Lysate into Multiscale 3D Scaffolds for Bone Tissue Engineering, ACS Biomaterials Science & Engineering 1(1) (2015) 2-6.
[159] M. Albanna, K.W. Binder, S.V. Murphy, J. Kim, S.A. Qasem, W. Zhao, J. Tan, I.B. El-Amin, D.D. Dice, J. Marco, J. Green, T. Xu, A. Skardal, J.H. Holmes, J.D. Jackson, A. Atala, J.J. Yoo, In Situ Bioprinting of Autologous Skin Cells Accelerates Wound Healing of Extensive Excisional Full-Thickness Wounds, Sci Rep 9(1) (2019) 1856.
[160] W.L. Ng, S. Wang, W.Y. Yeong, M.W. Naing, Skin Bioprinting: Impending Reality or Fantasy?, Trends Biotechnol 34(9) (2016) 689-699.
[161] N. Cubo, M. Garcia, J.F. Del Canizo, D. Velasco, J.L. Jorcano, 3D bioprinting of functional human skin: production and in vivo analysis, Biofabrication 9(1) (2016) 015006.
[162] L. Ouyang, R. Yao, Y. Zhao, W. Sun, Effect of bioink properties on printability and cell viability for 3D bioplotting of embryonic stem cells, Biofabrication 8(3) (2016) 035020.
[163] H.J. Yoon, S.R. Shin, J.M. Cha, S.H. Lee, J.H. Kim, J.T. Do, H. Song, H. Bae, Cold Water Fish Gelatin Methacryloyl Hydrogel for Tissue Engineering Application, PLoS One 11(10) (2016) e0163902.
[164] L. Kang, X. Liu, Z. Yue, Z. Chen, C. Baker, P.C. Winberg, G.G. Wallace, Fabrication and In Vitro Characterization of Electrochemically Compacted Collagen/Sulfated Xylorhamnoglycuronan Matrix for Wound Healing Applications, Polymers (Basel) 10(4) (2018).
[165] G.S. Schultz, A. Wysocki, Interactions between extracellular matrix and growth

factors in wound healing, Wound Repair Regen 17(2) (2009) 153-62.
[166] L.J. Pourchet, A. Thepot, M. Albouy, E.J. Courtial, A. Boher, L.J. Blum, C.A. Marquette, Human Skin 3D Bioprinting Using Scaffold-Free Approach, Adv Healthc Mater 6(4) (2017).
[167] J. Gopinathan, I. Noh, Recent trends in bioinks for 3D printing, Biomaterials Research 22(1) (2018) 11.
[168] S.T. Robinson, A.M. Douglas, T. Chadid, K. Kuo, A. Rajabalan, H. Li, I.B. Copland, T.H. Barker, J. Galipeau, L.P. Brewster, A novel platelet lysate hydrogel for endothelial cell and mesenchymal stem cell-directed neovascularization, Acta Biomater 36 (2016) 86-98.
[169] S.P. Tarassoli, Z.M. Jessop, S. Kyle, I.S. Whitaker, 8 - Candidate bioinks for 3D bioprinting soft tissue, in: D.J. Thomas, Z.M. Jessop, I.S. Whitaker (Eds.), 3D Bioprinting for Reconstructive Surgery, Woodhead Publishing2018, pp. 145-172.
[170] B.D. Fairbanks, M.P. Schwartz, C.N. Bowman, K.S. Anseth, Photoinitiated polymerization of PEG-diacrylate with lithium phenyl-2,4,6-trimethylbenzoylphosphinate: polymerization rate and cytocompatibility, Biomaterials 30(35) (2009) 6702-7.
[171] X. Chen, Z. Yue, P.C. Winberg, J.N. Dinoro, P. Hayes, S. Beirne, G.G. Wallace, Development of rhamnose-rich hydrogels based on sulfated xylorhamno-uronic acid toward wound healing applications, Biomater Sci 7(8) (2019) 3497-3509.
[172] N. Monteiro, G. Thrivikraman, A. Athirasala, A. Tahayeri, C.M. Franca, J.L. Ferracane, L.E. Bertassoni, Photopolymerization of cell-laden gelatin methacryloyl hydrogels using a dental curing light for regenerative dentistry, Dent Mater 34(3) (2018) 389-399.
[173] M. Pawlaczyk, M. Lelonkiewicz, M. Wieczorowski, Age-dependent biomechanical properties of the skin, Postepy Dermatol Alergol 30(5) (2013) 302-306.
[174] H. Joodaki, M.B. Panzer, Skin mechanical properties and modeling: A review, Proceedings of the Institution of Mechanical Engineers, Part H: Journal of Engineering in Medicine 232(4) (2018) 323-343.
[175] X. Liang, S.A. Boppart, Biomechanical properties of in vivo human skin from dynamic optical coherence elastography, IEEE transactions on bio-medical engineering 57(4) (2010) 953-959.
[176] A. Kalra, A. Lowe, Mechanical Behaviour of Skin: A Review, Journal of Material

Science & Engineering 5 (2016).
[177] C. Pailler-Mattei, S. Bec, H. Zahouani, In vivo measurements of the elastic mechanical properties of human skin by indentation tests, Medical Engineering & Physics 30(5) (2008) 599-606.
[178] A.C. Lima, J.F. Mano, A. Concheiro, C. Alvarez-Lorenzo, Fast and mild strategy, using superhydrophobic surfaces, to produce collagen/platelet lysate gel beads for skin regeneration, Stem Cell Rev Rep 11(1) (2015) 161-79.
[179] A. Hendi, M. Umair Hassan, M. Elsherif, B. Alqattan, S. Park, A.K. Yetisen, H. Butt, Healthcare Applications of pH-Sensitive Hydrogel-Based Devices: A Review, International journal of nanomedicine 15 (2020) 3887-3901.
[180] E.A. Kamoun, E.S. Kenawy, X. Chen, A review on polymeric hydrogel membranes for wound dressing applications: PVA-based hydrogel dressings, J Adv Res 8(3) (2017) 217-233.
[181] A. Shariati, A. Moradabadi, T. Azimi, E. Ghaznavi-Rad, Wound healing properties and antimicrobial activity of platelet-derived biomaterials, Sci Rep 10(1) (2020) 1032.
[182] H.A. Farghali, N.A. AbdElKader, H.O. AbuBakr, S.H. Aljuaydi, M.S. Khattab, R. Elhelw, M. Elhariri, Antimicrobial action of autologous platelet-rich plasma on MRSA-infected skin wounds in dogs, Scientific Reports 9(1) (2019) 12722.
[183] F.M. Chen, M. Zhang, Z.F. Wu, Toward delivery of multiple growth factors in tissue engineering, Biomaterials 31(24) (2010) 6279-308.
[184] Z. Wang, Z. Wang, W.W. Lu, W. Zhen, D. Yang, S. Peng, Novel biomaterial strategies for controlled growth factor delivery for biomedical applications, NPG Asia Materials 9(10) (2017) e435-e435.
[185] E. Jooybar, M.J. Abdekhodaie, M. Karperien, A. Mousavi, M. Alvi, P.J. Dijkstra, Developing hyaluronic acid microgels for sustained delivery of platelet lysate for tissue engineering applications, Int J Biol Macromol 144 (2020) 837-846.
[186] P. Losi, E. Briganti, E. Sanguinetti, S. Burchielli, T. Al Kayal, G. Soldani, Healing effect of a fibrin-based scaffold loaded with platelet lysate in full-thickness skin wounds, Journal of Bioactive and Compatible Polymers 30(2) (2015) 222-237.
[187] T. Buie, J. McCune, E. Cosgriff-Hernandez, Gelatin Matrices for Growth Factor Sequestration, Trends in Biotechnology 38(5) (2020) 546-557.
[188] T. Buie, J. McCune, E. Cosgriff-Hernandez, Gelatin Matrices for Growth Factor

Sequestration, Trends Biotechnol 38(5) (2020) 546-557.
[189] W.C. Yan, P. Davoodi, S. Vijayavenkataraman, Y. Tian, W.C. Ng, J.Y.H. Fuh, K.S. Robinson, C.H. Wang, 3D bioprinting of skin tissue: From pre-processing to final product evaluation, Adv Drug Deliv Rev 132 (2018) 270-295.
[190] T. Luttenberger, A. Schmid-Kotsas, A. Menke, M. Siech, H. Beger, G. Adler, A. Grünert, M.G. Bachem, Platelet-Derived Growth Factors Stimulate Proliferation and Extracellular Matrix Synthesis of Pancreatic Stellate Cells: Implications in Pathogenesis of Pancreas Fibrosis, Laboratory Investigation 80(1) (2000) 47-55.
[191] Q.L. Loh, C. Choong, Three-dimensional scaffolds for tissue engineering applications: role of porosity and pore size, Tissue Eng Part B Rev 19(6) (2013) 485-502.
[192] S.W. Volk, Y. Wang, E.A. Mauldin, K.W. Liechty, S.L. Adams, Diminished type III collagen promotes myofibroblast differentiation and increases scar deposition in cutaneous wound healing, Cells Tissues Organs 194(1) (2011) 25-37.

3 Chapter

Fabrication of 3D skin models

Table of Contents

3.1 Introduction

Bioprinting technology has been emerging as a fabrication tool for the development of complex compartmentalized structures to support skin tissue regeneration. The selection of an appropriate combination of cells, alongside the selection of suitable extracellular functional biomaterials for skin tissue printing plays a critical role in the success of the final construct. Several cells (individually encapsulated in the matrix or as cell aggregates) from autologous or allogenic nature have been exploited for skin bioprinting. A simplified approach is often used to produce skin equivalents which includes only dermal fibroblasts and/or epidermal keratinocytes without recreation of skin appendices. The most exploited cells for fabrication of the dermal and epidermal compartments of 3D skin constructs are fibroblasts and keratinocytes, respectively.[58, 91, 94, 95, 97, 106, 107, 114-117] Cubo et al., for example, used an extrusion-based bioprinting system to develop a bilayer skin construct composed of plasma-derived fibrin matrix populated with fibroblasts, topped by seeded keratinocytes. The bioprinted skin-like structure could emulate specific skin structure/functions in terms of epidermal terminal differentiation *in vitro* and *in vivo*.[101]

The skin is also a densely innervated organ. Upon skin injury, skin nerves may also get damaged and if nerve regeneration is imperfect, it can lead to abnormal sensations, chronic pain, or even permanent sensory deficits. Therefore, restauration of not only the aesthetic aspect but also the skin sensation and perceptions could have a major impact in a patient's quality of life.[193] Delayed wound healing of denervated tissue further highlight the importance of cutaneous nerves during the healing response. For example, peripheral neuropathy is one of the possible causes of delayed wound healing in

diabetes.[193] Electrical stimulation was proposed to improve nerve[194] and wound healing,[195] however, its therapeutic setting is still limited.

Tissue-engineered skin alternatives combining relevant cells, biomolecules, and biomaterials have been extensively used to establish a functional nerve network and induce tissue regeneration.[196] Choi et al., for example, used a coaxial nozzle printing to mimic the muscle structure, by fabricating a pre-vascularized muscle model with human umbilical vein endothelial cells (HUVECs) and vascular decellularized ECM (vdECM) in the outer shell and human muscle cells and skeletal muscle decellularized ECM (mdECM) in the inner core. The coaxial nozzle printed structure demonstrated to improve muscle fiber formation, vascularization, and innervation as well as 85% of functional recovery in volumetric muscle loss injuries.[197]

Despite recent advances in the biofabrication field, the incorporation of skin cells together with nerve cells into 3D printed constructs to generate an innervated skin-like macrostructure that mimic physiological functions of the skin has yet to be explored. Therefore, the aim of this work was to fabricate a more complex skin equivalent using the platform (HDF-PLGMA) established in the previous chapter as a base. First, a dermal-epidermal compartment was fabricated by seeding immortalized human keratinocytes (HaCaT) in an HDF-PLGMA printed structure and initial characterisation of the HaCaT/HDF-PLGMA construct was carried by expression of general keratinocyte differentiation markers, and histological analysis. Then, to fabricate an innervated dermal compartment, embryonic stem cell (ESC)-derived human NSCs (hNSC-H9) neurospheres were incorporated in the HDF-PLGMA printed construct and initial characterisation was performed to assess the ability of the HDF-PLGMA platform to support neurite outgrowth and neuron maturation.

3.2 Experimental Section

3.2.1 Materials

Key materials used in this chapter are introduced in detail as follow.

Materials	Source	Cat Number
Human dermal fibroblasts (HDF)	Cell Applications	
Immortalized human keratinocytes (HaCaT)		
human embryonic stem cell (hESC), WA09	WiCell	
DMEM, high glucose, HEPES	Sigma-Aldrich	D1152
Fetal Bovine Serum	Interpath	SFBSN2
Penicillin/Streptomycin	Gibco	15140122
Ham's F12	Life Technologies	21041025
Hydrocortisone	Sigma-Aldrich	
Triiodothyronine	Sigma-Aldrich	
Human transferrin	Sigma-Aldrich	
Insulin	Sigma-Aldrich	
Cholera toxin	Sigma-Aldrich	
Ascorbic acid	Sigma-Aldrich	
Epidermal Growth Factor (EGF-1)	Lonza	
Neural media		
Y27		
Brain-derived neurotrophic factor (BDNF)		
Nerve growth factor (B-NGF)		
Neurotrophin-3 (NT-3)		
Glial cell line-derived neurotrophic factor (GDNF)		
Human platelet lysate (PL)	PL BioScience	
Heparin	Sigma-Aldrich	H3149
Gelatin (porcine skin, Type A, 300 Bloom)	Sigma-Aldrich	G2500
Methacrylic anhydride	Sigma-Aldrich	P5927
Lithium phenyl-2,4,6-trimethylbenzoylphosphinate (LAP)	Sigma-Aldrich	900889
Antibodies		
Rabbit polyclonal anti-cytokeratin 10	ABCAM	ab111447
Rabbit polyclonal anti-involucrin	ABCAM	ab53112
Rabbit polyclonal anti-collagen III	ABCAM	ab7778
Rabbit polyclonal anti-collagen IV	ABCAM	ab235296

Rabbit polyclonal anti-cytokeratin	ABCAM	ab111447
Mouse monoclonal anti-Ki67(SOlA15) efluor 570	Life Technologies	41-5698-82
Chicken polyclonal anti-β tubulin III	Merk Millipore	AB9354
S-100B		
Goat polyclonal anti-trkA	R&D Systems	AF175
Mouse anti-trKB	R&D Systems	NOVNBP14789
Rabbit monoclonal anti-trKC	Invitrogen	7H3L20
Mouse monoclonal anti-MAP2	Sigma-Aldrich	M4403
Mouse monoclonal anti-BRN3A	Merk Millipore	MAB1585
Rabbit polyclonal anti-collagen I	ab21286	ABCAM
Mouse anti-neurofilament 200		
DAPI	Invitrogen	D1306
PCR		
AurumTM Total RNA 96 Kit	Bio-rad	7326800
iScript RT Supermix, 100 rxns	Bio-rad	1708841
SYBR® Select Master Mix	Life Technologies	4472897
Trichrome Masson		
Weigert's Iron Hematoxylin Solution	Sigma-Aldrich	HT1079
Bouin's solution	Sigma-Aldrich	HT10132
Biebrich Scarlet-Acid Fucshin solution	Sigma-Aldrich	HT151
Phosphotungstic Acid Solution	Sigma-Aldrich	HT152
Phosphomolybdic Acid Solution	Sigma-Aldrich	HT153
Aniline Blue Solution	Sigma-Aldrich	HT154

3.2.2 Cell culture

Human dermal fibroblasts (HDFs) were cultured as previously described on chapter 2.

Immortalized human keratinocytes (HaCaT) were cultured in growth media comprising DMEM/Ham's F12 (1:1) supplemented with 10% *v/v* FBS and 1% *v/v* P/S under standard culture conditions in a humidified atmosphere with 5% CO2 at 37°C. Differentiation media for HaCaT comprises of DMEM/Ham's F12 (1:1) supplemented with 10% *v/v* FBS and 1% *v/v* P/S, 0.4 μg/mL hydrocortisone, 5μg/mL triiodothyronine, 5 μg/mL human transferrin, 5 μg/mL insulin, 10 ng/mL cholera toxin, 10 ng/mL EGF-1

and 50 μg/mL ascorbic acid. Culture media was changed every three days. The cells were routinely passaged in tissue culture flasks when they reached 80% confluence and were discarded after 20 passages to ensure reproducibility of key characteristics.

Embryonic stem cell (ESC)-derived human NSCs (hNSC H9) neurospheres used in this work were kindly provided by S. Miellet and A/P M. Dottori, Illawarra Health and Medical Research Institute, University of Wollongong (Human Ethics committee approval #2017 375). hNSC H9 neurospheres are 3D aggregates of neural progenitors produced by conventional neuronal generation protocol. Briefly, undifferentiated human embryonic stem cell (hESC), WA09 (H9, WiCell), were maintained in feeder-free conditions on a laminin (LAM) coated dish (Corning) using E8 basal medium (Life Technologies). For neural induction, Neurobasal™ Medium (NB) (Life Technologies), freshly supplemented with 10 μM SB431524 (SB) and 3 μM CHIR99021 was added and maintained for five days. The media was changed every third day. Neural progenitor cells were then pelleted in a 50 mL tube at 200 g for 3 minutes. Cells were resuspended in NB medium supplemented with 10 ng/mL BMP-2 and 20 ng/mL FGF2. Cells were plated in U-bottom ultra-low attachment 96-multiwell plates (Corning), plates are spun at 200 g for 4 minutes. On the third day, media is top up with 50 μL of freshly supplemented media. For neuronal differentiation, whole spheres are manually disaggregated and plated onto PDL/LAM coated 24 well plate. Neural media is freshly supplemented with 10 μg/mL of small molecule Y27 and 10 ng/mL brain-derived neurotrophic factor (BDNF), nerve growth factor (B-NGF), neurotrophin-3 (NT-3) and glial cell line-derived neurotrophic factor (GDNF), changing media every third day.

3.2.3 Fabrication of epidermal-dermal constructs

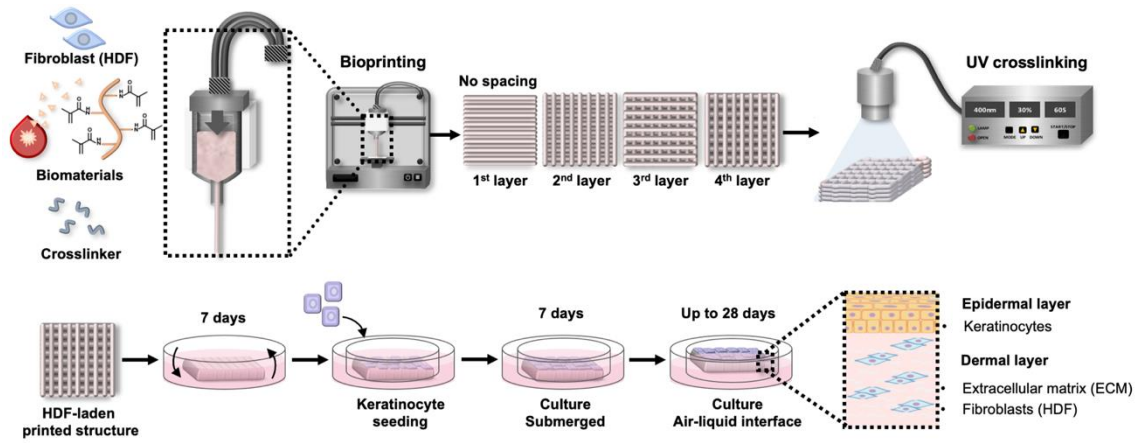

Figure 3.1 Schematic representation of the HaCaT/HDF-PLGMA fabrication.
Showing the HDF-PLGMA bioprinting process from material selection/ink formulation, printing and shape fixation though UV light, then the HaCat seeding and culture.

Bilayer models (HaCaT/HDF-PLGMA) were fabricated by pneumatic extrusion printing (Envision TEC) the dermal component (HDF-laden PLGMA) and epidermal component (keratinocytes HaCaT) was seeded on the top of the 3D printed HDF-laden PLGMA construct (Figure 3.1). Briefly, three layers of HDF-PLGMA were printed as previously described (0°/90° a crosshatch pattern, slicing thickness 200 µm and strand spacing of 1.0 mm), then the fourth layer was printed at spacing of 0.4 mm. After crosslinking, HDF-laden PLGMA was placed in 12 well plates containing HDF growth medium and cultured for a week under standard culture conditions 5% CO_2 at 37°C. Samples were then transferred to a permeable membrane of a cell culture insert (air-liquid interface setting - ALI), which can be air-lifted so the apical surface is exposed to air, whereas the basal surface of the construct is in contact with the cell culture medium.

Keratinocytes HaCaT (about 2 × 10^5 cells/cm^2 density) were then seeded on top of HDF-PLGMA and cultured submerged in HaCaT growth medium for a week to reach confluency. Then, the construct was subjected to air exposure and cultured in differentiation media under 5% CO_2 at 37°C. Culture media was changed every day after air exposure as media volume was low and cell density was high. HaCaT/HDF-PLGMA samples were collected at specific time points for the following experiments.

3.2.4 Fabrication of innervated-dermal constructs

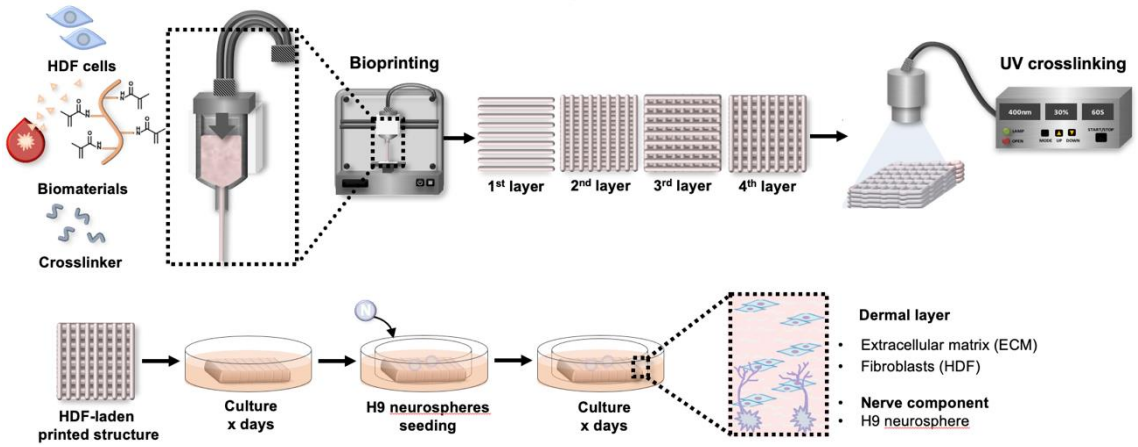

Figure 3.2 Schematic representation of the H9/HDF-PLGMA fabrication.
Showing the HDF-PLGMA bioprinting process from material selection/ink formulation to shape fixation though UV light induced crosslinking, then the hNSC H9 sphere seeding and culture.

Innervated dermal model (H9/HDF-PLGMA) were fabricated by printing (Envision TEC) the dermal component (HDF-laden PLGMA) and then seeding the nerve compartment (two weeks old hNSC H9 neurospheres of ~200µm diameter) on 3D printed HDF-laden PLGMA (Figure 3.2). Briefly, HDF-PLGMA was bioprinted, as previously reported in chapter 2, cultured in DMEM (10% *v/v* FBS, 1% *v/v* P/S) under

5% CO_2 at 37°C. Then, two weeks old hNSC H9 spheres were seeded on top of the printed dermal construct, construct was flipped so hNSC H9 spheres would be on the bottom. Co-cultured was maintained in supplemented neural differentiation media under 5% CO_2 at 37°C, and collected for analysis at specific time points. H9/HDF-PLGMA represents printed HDF-PLGMA and seeded H9.

3.2.5 Immunohistochemistry assay – keratinocyte differentiation

As previously reported, immunohistochemical analysis as performed as follow samples were collected at specific time points, fixed in 3.7% *v/v* paraformaldehyde (PFA) solution for 30 minutes, kept at 5°C or embedded in optimal cutting temperature (OCT) compound, snap-frozen using dry ice and stored at -20°C. OCT embedded samples blocks were cryo-sectioned into 10 - 20μm sections and mounted on glass slides. The unspecific binding of the antibody was blocked by 5% donkey serum in PBS for 1 hour at room temperature followed by overnight incubation with primary antibodies diluted in blocking solution.

The expression of proteins associated with keratinocyte proliferation and differentiation was analysed in 3D culture of HaCaT in 3D printed HDF-PLGMA constructs. The primary antibodies used were rabbit polyclonal anti-cytokeratin 10, mouse monoclonal anti-Ki67 (SOlA15) efluor 570, rabbit polyclonal anti-involucrin. ECM component was analysed using goat polyclonal anti-collagen IV, and rabbit polyclonal anti-collagen III. After 3 washes with PBS, the respective secondary antibodies were applied in blocking solution for 1 h at room temperature, rinsed in PBS for 3 changes. Lastly, cell nuclei were counterstained with DAPI, substrate solution at room temperature for 5 minutes,

rinsed and mounted. The staining was then observed and imaged using confocal microscope (Leica TSC SP5 II).

3.2.6 Immunohistochemistry assay – neuronal differentiation

The expression of proteins associated with neuronal proliferation and differentiation was analysed in hNSC H9 neurospheres cultured in 3D printed HDF-PLGMA constructs. Immunohistochemical analysis as performed as previously described. The primary antibodies used were chicken anti-β tubulin III, S-100B, tropomyosin receptor kinase (Trk): goat anti-TrkA, mouse anti-TrKB and rabbit anti-TrKC, mouse anti-MAP2, mouse anti-BRN3A and mouse anti-neurofilament 200. ECM component was stained using rabbit anti-collagen I. Cell nuclei were counterstained with DAPI, substrate solution at room temperature for 5 minutes, rinsed and mounted. The staining was then observed and imaged using confocal microscope.

3.2.7 RNA isolation and RT-qPCR analysis

As previously reported, total RNA was extracted from cells using Aurum^{TM} Total RNA Mini Kit following the supplier's instructions. Reverse transcription to convert RNA sequence into cDNA was performed according to the manufacturer's protocol using C1000 Touch^{TM} Thermal Cycler. The resultant cDNA was then subjected to qRT-PCR using CFX96 Real-Time System (Applied Biosystems) with SsoAdvanced Universal SYBR Green RT- PCR Kit according to the manufacturer's protocol. All reactions were performed in triplicate. Corresponding gene expression levels were normalized to *GAPDH*. The fold-change of the target genes was calculated by using the $2^{-\Delta\Delta CT}$ method as previously reported.

Table 3.1 List of primers used for real time RT-PCR

Gene	Primer sequence (5'-3')
GAPDH	F: ATGGAAATCCCATCACCATCTT
	R: CGCCCCACTTGATTTTGG
KGF-1	F: CTTCTGTCGAACACAGTGGTACCT
	R: TCATCTCTTGGGTCCCTTTTACTT
MMP-1	F: CAGATGTGGACCATGCCATTGAG
	R: CATCAATGTCATCCTGAGCTAGC

3.2.8 Masson trichrome staining

Histological analysis was performed to confirm the stratification for the epidermal layer in the 3D culture of HaCaT in 3D printed HDF-PLGMA constructs. Masson trichrome staining was performed according to the manufacturer's protocol. Briefly, frozen sections were mordanted in preheated Bouin's solution at 56°C for 15 minutes, rinsed in running tap water, treated with Weigert's iron Hematoxylin solution for 5 minutes. After removing the Hematoxylin solution, the sections were treated with Biebrich Scarlet-acid Fucshin for 5 minutes. After rinsed with distilled water, slides were treated with working phosphotungsten/phosphomolybdic acid solution for 5 minutes. Subsequently, slides were treated with aniline blue solution for 5 minutes and, acetic acid, 1%, for 2 minutes. Finally, the sections were rinsed with distilled water, dehydrated, mounted, and observed.

3.2.9 CellTiter-Glo® 3D viability assay

CellTiter-Glo® 3D cell viability assay was used to determine the viability of hNSC H9 neurospheres encapsulated in crosslinked bioinks (cell-free PLGMA), according to the manufacturer's protocol. Samples were prepared by embedding H9 cells (spheres and single cells) in 30 μL of bioink and crosslinking directly into opaque-walled multi-well plates for 45 seconds (13.2mW). Samples were cultured under 5% CO2 at 37°C; culture

media was added to each well and changed every other day. After four days of culture, CellTiter-Glo® 3D reagent was added to each well, mixed for 5 minutes and allowed to incubate for 25 minutes. Lastly, luminescent was recorded using a microplate reader (POLAR star Omega, BMG Labtech).

3.2.10 Statistical analysis

One-way analysis of variance (ANOVA) test followed by Tukey's post-hoc test was used to assess the statistical significance of results between groups. The statistical analysis was performed with the software OriginPro at a confidence level of 95%. Differences were considered statistically significant at $p < 0.05$. Data are expressed as the mean ± standard deviation (SD) for $n > 3$.

3.3 Results

3.3.1 HDF-PLGMA influence on HaCaT

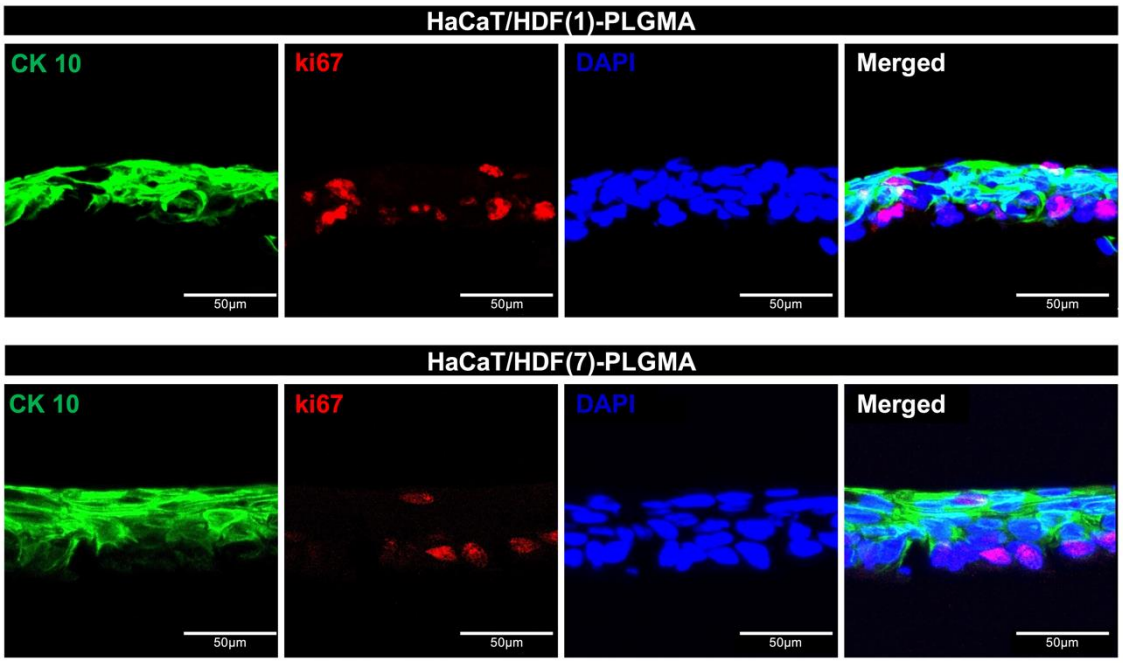

Figure 3.3 Preliminary assessment of HaCaT differentiation and proliferation in 3D printed HDF-PLGMA constructs.
HaCaT/HDF(1)-PLGMA refers to sample printed a day prior to HaCaT seeding, and HaCaT/HDF(7)-PLGMA refers to samples printed a week prior to HaCaT seeding. Fluorescent images from immunohistochemical staining with antibodies against CK10 = cytokeratin 10, and Ki67. Scale bars as indicated.

In this study, the human immortalized cell line HaCaT was used as a proxy model for keratinocytes in human skin. Although primary cells are frequently used for 2D-3D *in vitro* culture systems, HaCaT cell line has been successfully used to fabricate the epidermal compartment of 3D skin model with typical epithelial morphology, demonstrating to be reproducible and reliable.[105, 106, 135]

Preliminary experiment was performed to study the influence of HDF on HaCaT differentiation and stratification. Two groups were used on this experiment, HDF printed one day prior to HaCaT seeding (HaCaT/HDF(1)-PLGMA) and HDF printed a week prior to HaCaT seeding (HaCaT/HDF(7)-PLGMA). After a week of culture under ALI conditions, the expression of keratinocytes differentiation marker, such as cytokeratin 10 (CK10), and proliferation marker, Ki67, were assessed. Ki67 and CK10 markers were expressed in both HaCaT/HDF(1)-PLGMA and HaCaT/HDF(7)-PLGMA constructs after culture for a week, however, HaCaT/HDF(7)-PLGMA showed better structural organisation with significant change of nuclei shape in the most outer HaCaT layer in comparison to HaCaT/HDF(1)-PLGMA (Figure 3.3). HDF printed a week prior to HaCaT seeding (HaCaT/HDF-PLGMA) was then selected for the following experiments.

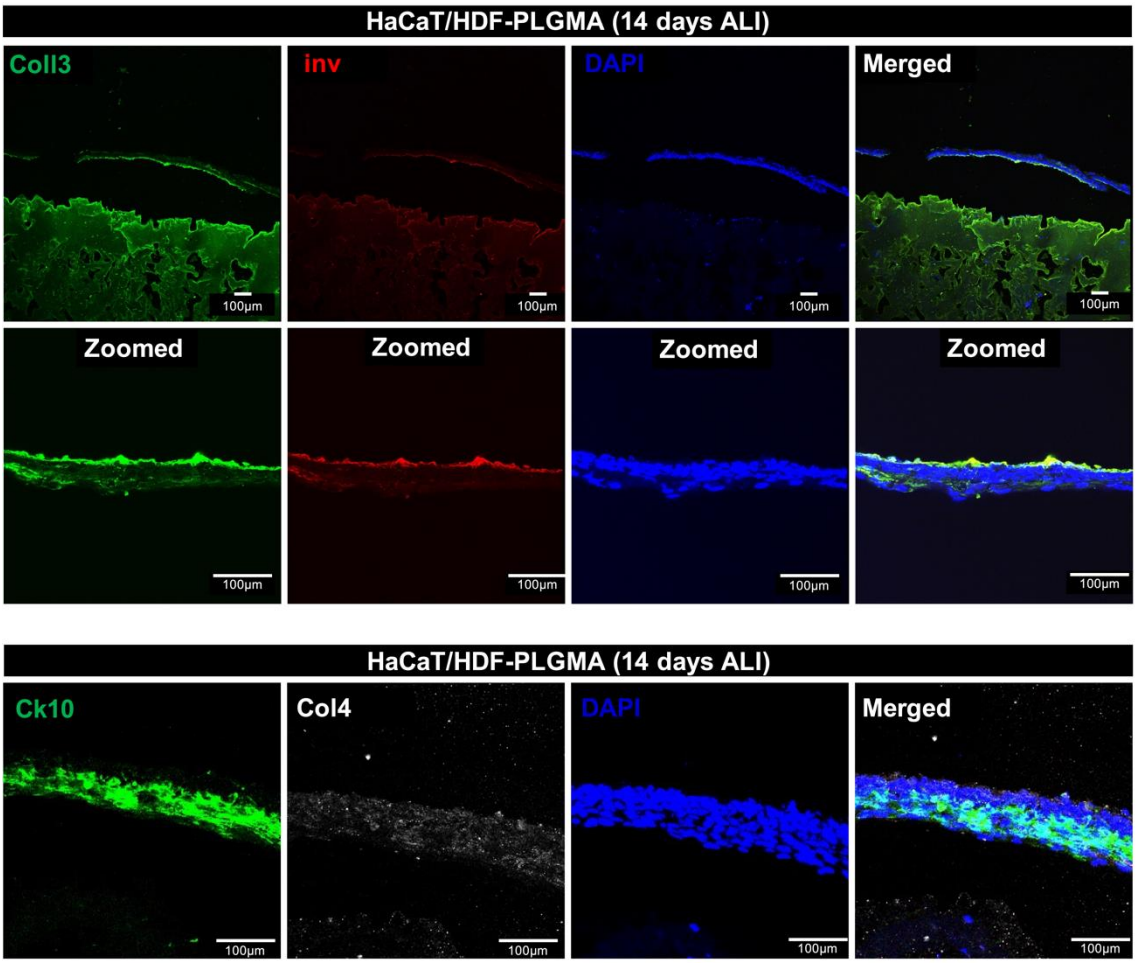

Figure 3.4 Assessment of HaCaT differentiation in 3D printed HDF-PLGMA cultured in ALI for 2 weeks.

Fluorescent images from immunohistochemical staining with antibodies against CK10, involucrin and collagen IV. Coll3 = collagen III, col4 = collagen IV, and inv = involucrin. Scale bars as indicated.

The expression of cytokeratin 10 and involucrin was detected in the superficial HaCaT layer of the HaCaT/HDF-PLGMA epidermal compartment after two weeks of culture under ALI conditions (Figure 3.4). Expression of collagen III was observed in the dermal compartment of HaCaT/HDF-PLGMA samples cultured under ALI conditions for two weeks. The separation of epidermal layer from dermal layer observed in the zoomed-out staining images (Figure 3.4) is due to the cryosectioning method which disintegrated these structures during sectioning process.

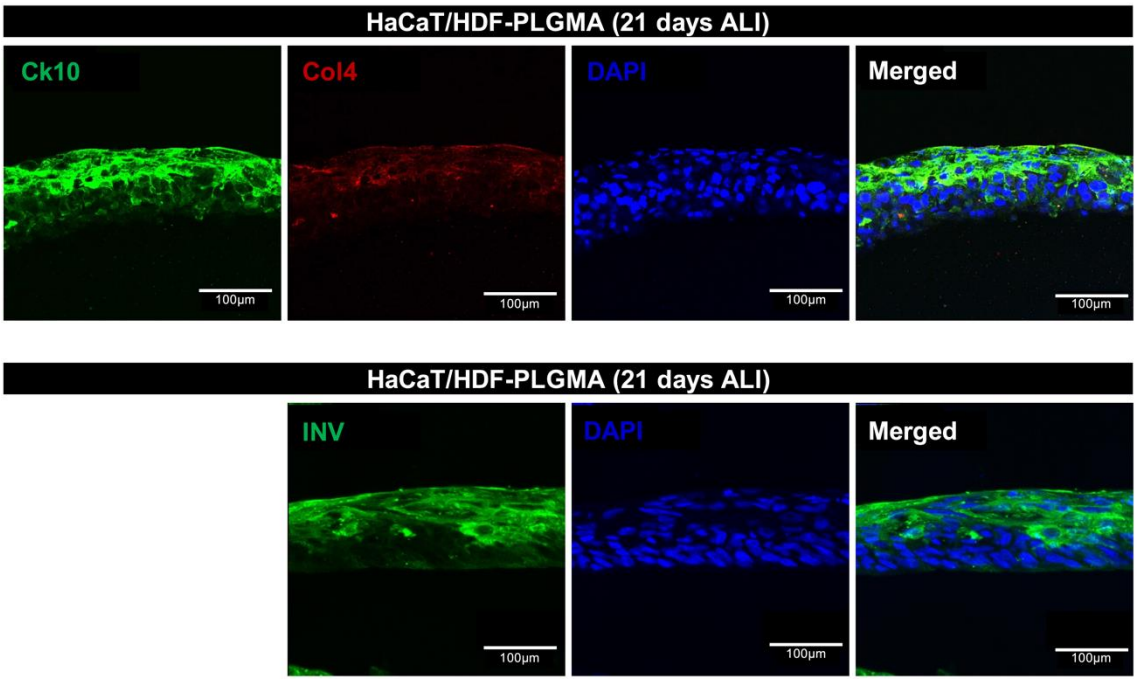

Figure 3.5 Assessment of HaCaT differentiation in 3D printed HDF-PLGMA cultured in ALI for three weeks.

Fluorescent images from immunohistochemical staining with antibodies against cytokeratin CK10, involucrin and collagen IV. Scale bars as indicated.

The expression of cytokeratin 10 and involucrin was strongly observed on HaCaT/HDF-PLGMA samples cultured for three weeks under ALI conditions, as shown in Figure 3.5. Low expression of collagen IV (Figure 3.4 and 3.5) was also observed in the epidermal component of the HaCaT/HDF-PLGMA samples. The staining of collagen IV in the epidermal compartment, instead of the basement membrane could indicate that collagen IV just started to be secreted by keratinocytes, and eventually would be accumulated on the cell surface to form junction structures to anchor the epidermis to the dermis. Taken all together, the expression of involucrin, cytokeratin, collagen III and collagen IV confirmed the capacity of HaCaT/HDF-PLGMA platform to promote normal epithelial morphogenesis and differentiation of keratinocytes.

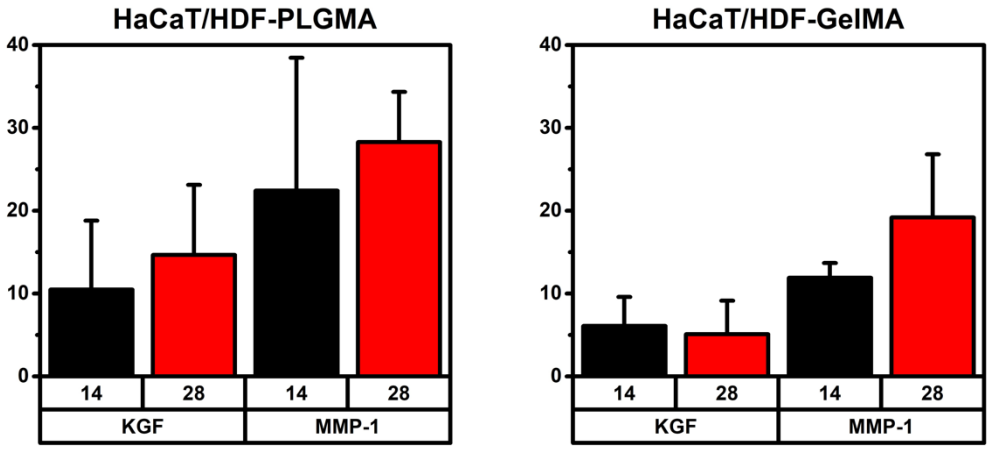

Figure 3.6 Relative gene expression of KGF and MMP-1
after 2-3 weeks of culture from HaCaT/HDF-PLGMA and HaCaT/HDF-GelMA control group.

Keratinocytes stimulate fibroblasts to synthesize and secrete growth factors including keratinocyte growth factor (KGF), which plays a critical role in supporting epidermal proliferation.[198, 199] Higher expression of metalloproteinases (MMPs) is also observed in fibroblast under the influence of keratinocytes [200] Therefore, expression of KGF-1, MMP-1 were quantified to confirm keratinocyte-fibroblasts interaction and assess the PLGMA matrix effect on the expression of those markers in HaCaT/HDF-PLGMA cultured for 2-3 weeks. Data was compared to HaCaT/HDF cultured in GelMA control group. qPCR data indicates higher expression of KGF-1, MMP-1 by cells cultured in PLGMA possibly because of the PL growth factors, yet difference between groups was not statistically significant ($p \geq 0.05$).

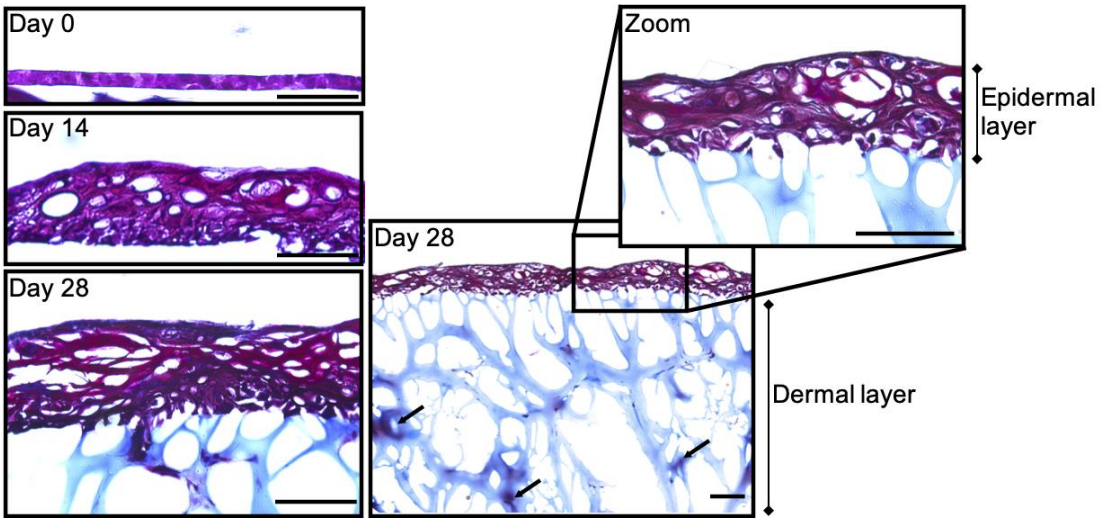

Figure 3.7 Histological assessment of HaCaT differentiation in 3D printed HDF-PLGMA.

Bright field images from Masson's trichrome staining showing epidermal compartment (keratin stained in red), dermal compartment (collagen stained in blue), cell cytoplasm stained in pink and cell nuclei in dark brown.

The histological analysis of HaCaT/HDF-PLGMA samples, cultured for up to four weeks under ALI conditions, was performed using Masson's trichrome staining. This three-colour staining protocol used in histology stains keratin in red, collagen in blue, cell cytoplasm in light red or pink and cell nuclei in dark brown to black. Bright field microscope images show stratification evolution of the epidermal compartment of HaCaT/HDF-PLGMA samples from day-0 to day-28 of culture under ALI conditions. At day-0, HaCaT/HDF-PLGMA epidermal compartment shown to be thin and only HaCaT cytoplasm and cell nuclei was stained. Figure 3.7 confirms stratification of the HaCaT/HDF-PLGMA epidermal compartment after 2-3 weeks of culture under ALI conditions, HaCaT/HDF-PLGMA epidermal compartment showed stratification with high deposition of keratin and obvious change in epidermal structure. Moreover, HaCaT/HDF-PLGMA dermal compartment demonstrated a remarkably porous collagen-rich matrix with staining of some fibroblasts. The matrix morphology shown

after three weeks of culture, could be due to keratinocyte and fibroblast secretion of multiple enzymes that were degrading the matrix, as well as morphology distortion due to artifacts/ice crystals formed during slow freezing. Paraffin-embedded samples should be investigated, and protocol should be optimized in order to confirm the histological morphology of the HaCaT/HDF-PLGMA samples.

3.3.2 HDF-PLGMA influence on hNSC H9

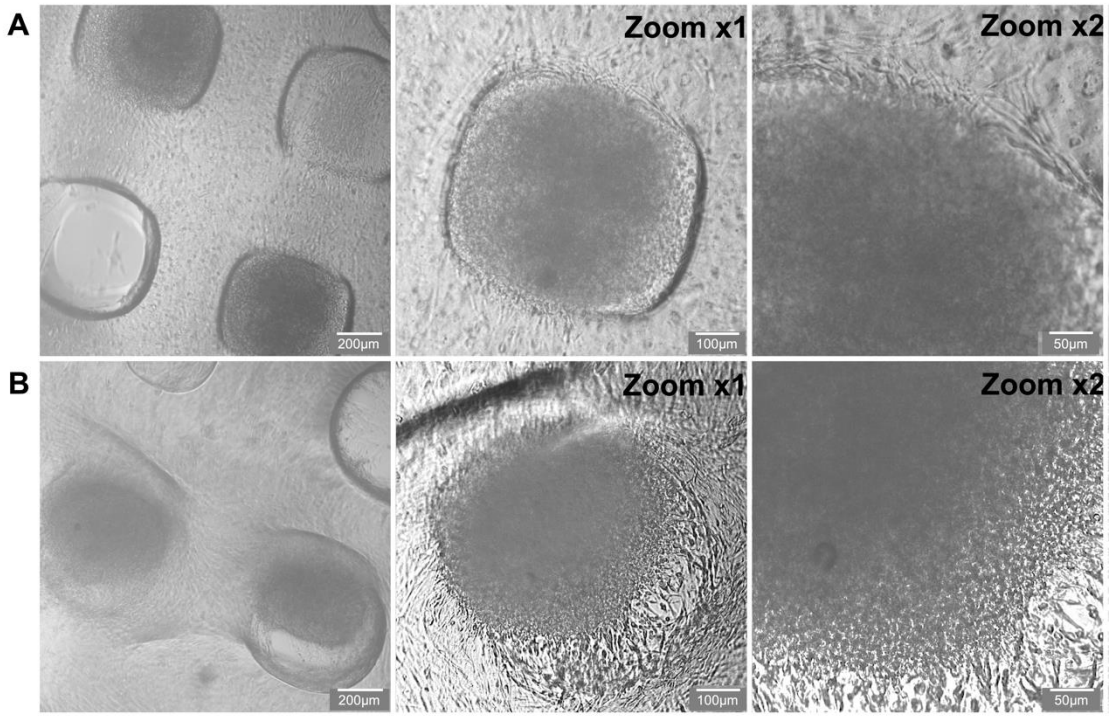

Figure 3.8 Bright field macroscope images of H9/HDF-PLGMA (day-1).
(A) day-1 culture of H9/HDF(1)-PLGMA – H9 neurospheres seeded in HDF-PLGMA (printed 1-day prior H9 seeding). (B) day-1 culture of H9/HDF(7)-PLGMA – H9 neurospheres seeded in HDF-PLGMA (printed 7-days prior H9 seeding). Scale bar as indicated.

Two groups were assessed in this section to study the influence of HDF on hNSC H9 neurospheres behaviour. H9/HDF(1)-PLGMA - HDF-PLGMA printed one day prior to hNSC H9 seeding, and H9/HDF(7)-PLGMA - HDF-PLGMA printed a week prior to

hNSC H9 seeding, as it was hypothesised that culturing HDF for days before introducing the hNSC H9 would allow HDF to secrete signalling molecules and ECM components, and therefore, provide a better environment for hNSC H9 to thrive. Bright field macroscope images shows day-1 after the H9 neurosphere were seeded in both experimental groups: Figure 3.8A shows the H9/HDF(1)-PLGMA; and Figure 3.8B shows the H9/HDF(7)-PLGMA. Figure 3.8 also highlight the structure of the 3D printed HDF-laden lattice construct, with HDF homogenously distributed throughout the matrix and hNSC H9 spheres seeded in between strands. hNSC H9 were cultured as free-floating proliferating neurospheres, which embody heterogeneous populations of neural progenitor cells and neural stem cells.

The aggregation of stem cells into 3D environment is mediated by intrinsic cell–cell interaction as well as cell–ECM interactions.[201] Migration of cell out of spheres is often initiated by plating neurospheres in a treated substrate and enriched medium containing growth factors.[202-204] This data suggests that at a day after seeding, hNSC H9 were already well integrated with the matrix and cells started to migrate out of the sphere in both experimental groups, but more evident on H9/HDF(7)-PLGMA samples (Figure 3.8B), where interaction of migrating cells with HDF filopodia were also observed.

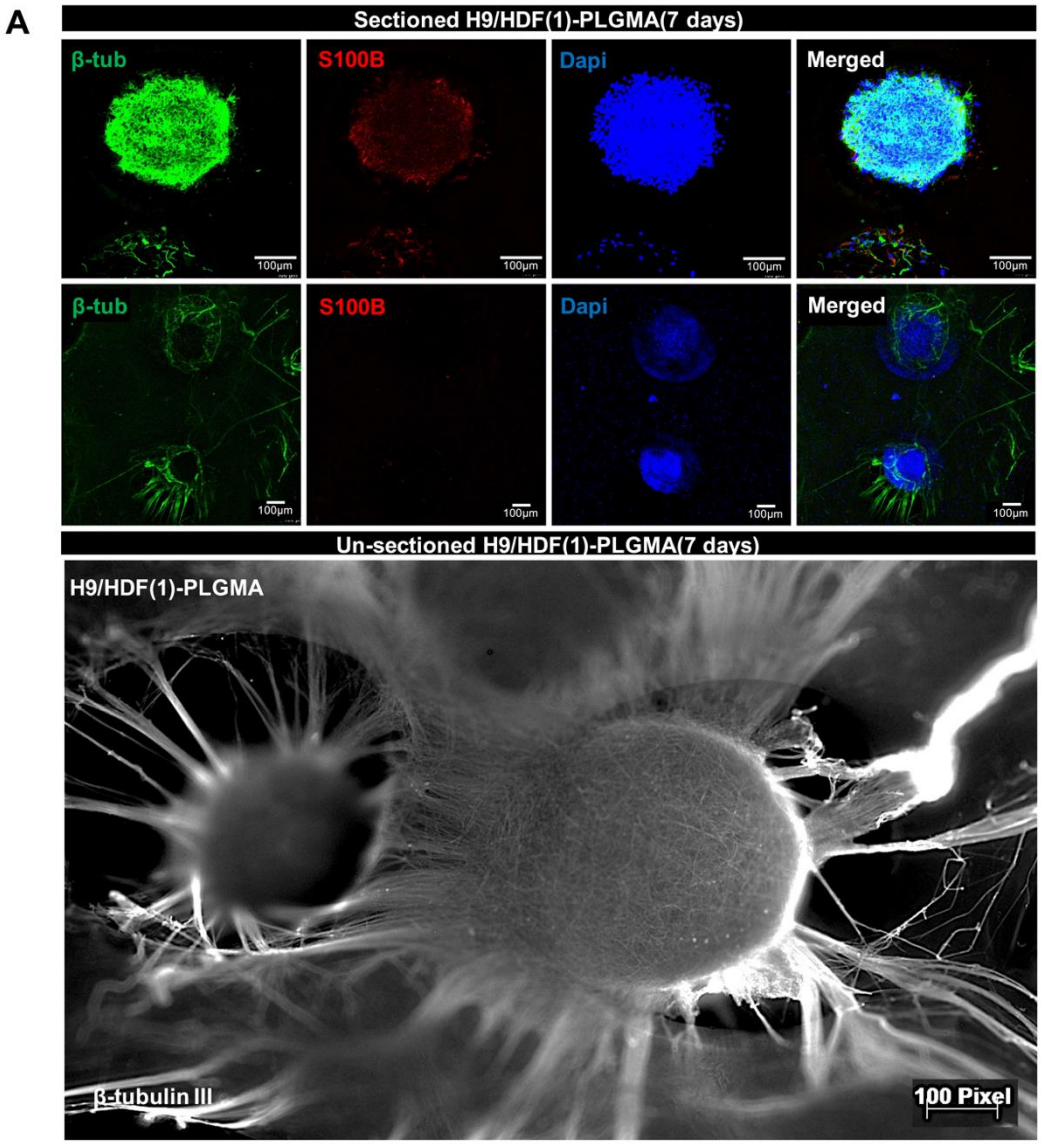
A
Sectioned H9/HDF(1)-PLGMA(7 days)
β-tub
S100B
Dapi
Merged
100μm
Un-sectioned H9/HDF(1)-PLGMA(7 days)
H9/HDF(1)-PLGMA
β-tubulin III
100 Pixel

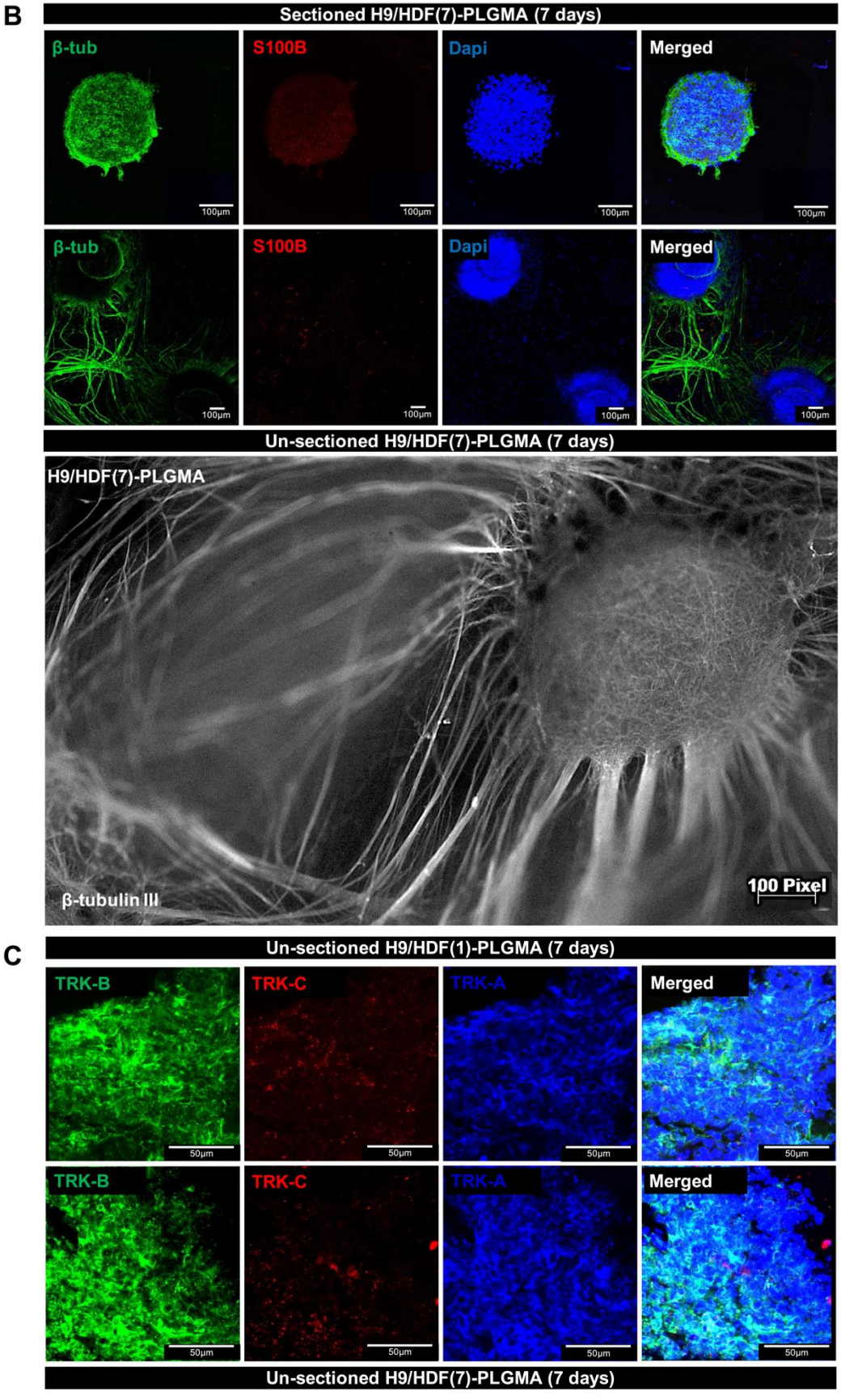
B
Sectioned H9/HDF(7)-PLGMA (7 days)
β-tub
S100B
Dapi
Merged
100μm
Un-sectioned H9/HDF(7)-PLGMA (7 days)
H9/HDF(7)-PLGMA
β-tubulin III
100 Pixel
C
Un-sectioned H9/HDF(1)-PLGMA (7 days)
TRK-B
TRK-C
TRK-A
Merged
50μm
Un-sectioned H9/HDF(7)-PLGMA (7 days)

Figure 3.9 Immunohistochemistry images of general neuronal markers in H9 cultured for a week in HDF-PLGMA.
(A) Expression of β-tubulin III and S100B in H9/HDF(1)-PLGMA - H9 neurospheres seeded in HDF-PLGMA (printed 1-day prior to H9 seeding). (B) Expression of β-tubulin III and S100B in H9/HDF(7)-PLGMA - H9 neurospheres seeded in HDF-PLGMA (printed a week prior to H9 seeding) (C) Staining images of trk receptors in sectioned samples. Scale bar as indicated.

Figure 3.9A shows neurons stained with β-tubulin III and S-100B antibodies in sectioned and un-sectioned H9/HDF(1)-PLGMA samples after a week of culture. Figure 3.9B shows neurons stained with β-tubulin III and S-100B antibodies in sectioned and un-sectioned H9/HDF(7)-PLGMA samples after a week of culture. Lastly, Figure 3.9C shows the expression of trk receptors in sectioned samples after a week of culture. Both experimental groups demonstrated to support extensive neurite outgrowth, which was confirmed by β-tubulin III staining. β-Tubulin III staining (black/white) images taken with Leica inverted axiovert microscope better represent the overall 3D neurite network in comparison to z-stacked confocal images (coloured images). Images of samples stained with β-tubulin III antibody taken with the inverted microscope were processed with ImageJ software to measure the average length of neurite outgrowth from neurospheres. The length of 15 neurites branches were measured, then average and standard deviation was calculated. Although measurement of neurite outgrowth was not very accurate, neurite outgrowth from H9/HDF(7)-PLGMA samples (1904μm ± 386) demonstrated to be about 2 times longer than H9/HDF(1)-PLGMA (926μm ± 218). By that, we can conclude that fibroblast cultured for a week prior to the H9 seeding secreted certain growth factors and other ECM components that promoted faster neurite outgrowth from hNSC H9 neurospheres.

Low expression of S100B marker was also observed on hNSC H9 neurospheres cultured in both experimental groups H9/HDF(1)-PLGMA and H9/HDF(7)-PLGMA. Immunohistochemistry images indicates the expression of Trk-A, -B and -C were stained in sectioned samples of both groups. H9/HDF(1)-PLGMA and H9/HDF(7)-PLGMA samples showed expression of all 3 tropomyosin receptors. These data all together confirm neuronal differentiation of hNSC H9 cultured for a week in both sets of HDF-PLGMA/H9 samples. Since H9/HDF(7)-PLGMA shown to support higher β-tubulin III expression, next experiments were performed using HDF-PLGMA printed a week prior H9 seeding.

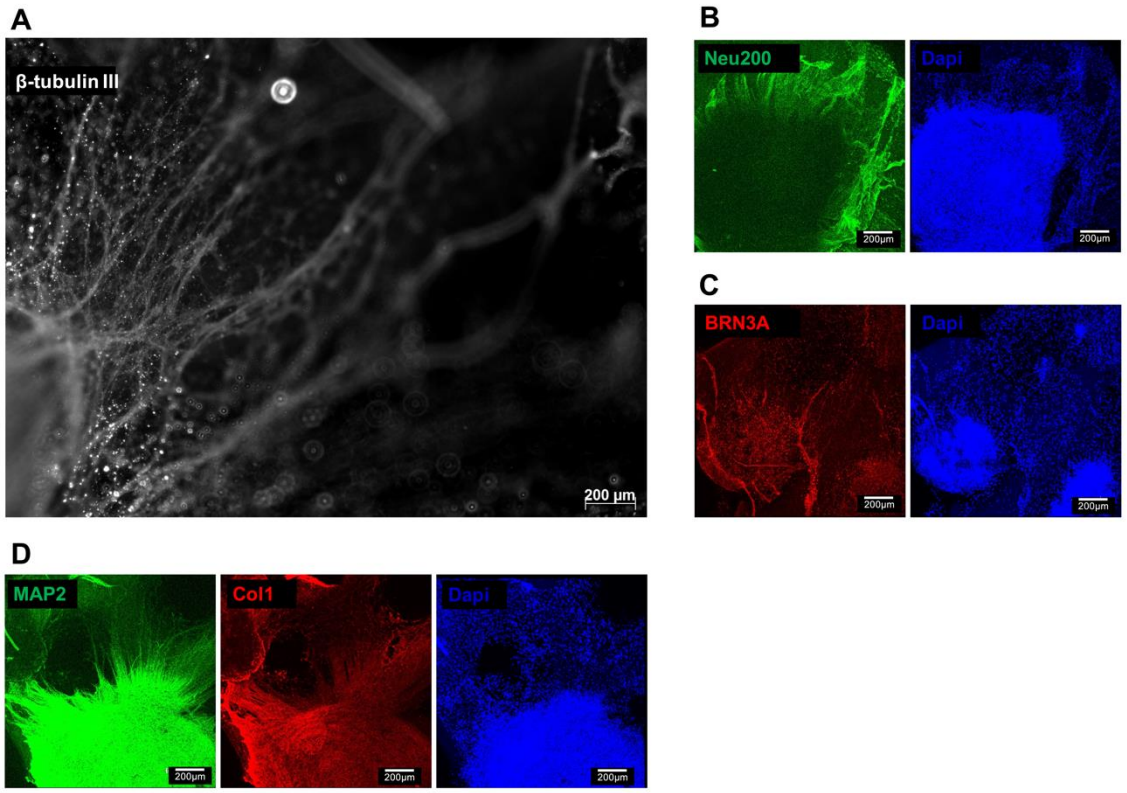

Figure 3.10 Expression of mature/general neuronal markers in H9 cultured for 3 weeks in HDF-PLGMA.

Immunohistochemistry images of β-tubulin III, MAP2, BRN3A, Neurofilament-200 and collagen I in H9/HDF-PLGMA– 21-days culture of H9 neurospheres seeded in HDF-PLGMA (printed 7-day prior H9 seeding). Scale bar as indicated.

After three weeks of culture of hNSC H9 spheres in 3D printed HDF-PLGMA samples, mature neuronal markers such as BRN3A, MAP2 and Neurofilament 200 were expressed successfully (Figure 3.10). Images of H9/HDF-PLGMA cultured for three weeks were stained with β-tubulin III antibody and processed with ImageJ software to measure the average length of neurite outgrowth from neurospheres. Neurite outgrowth from H9/HDF-PLGMA samples (2912μm ± 436) after cultured for three weeks, about 1.5 times longer than the neurites measured after two weeks of culture. Although the measurement is not precise, this information reinforces the hypothesis that strong cell-matrix interactions support neurite outgrowth. Combining these data, it can be concluded that neurospheres were maturing well in the dermal 3D printed HDF-PLGMA construct after three weeks of culture.

Table 3.2 Bioink composition

Bioink ID	**PL (*v*/*v*)**	**GelMA (*v*/*v*)**	**LAP (*v*/*v*)**	**LAM (μl/mL)**
A	50%	7.5%	0.03%	
Ai	50%	7.5%	0.03%	10
B	50%	5%	0.06%	
Bi	50%	5%	0.06%	10
C	50%	6.25%	0.025%	
Ci	50%	6.25%	0.025%	10
D	50%	6.25%	0.045%	
Di	50%	6.25%	0.045%	10

Preliminary experiments were carried to assess the cytocompatibility of hNSC H9 cells encapsulated in different PLGMA ink formulations. hNSC H9 cells were encapsulated into eight different ink formulations containing different GelMA and LAP concentrations (Table 3.2). The impact of matrix stiffness on cell behaviour was assessed by qualitative screening of neurospheres morphology from bright field macroscope images. Laminin is commonly used in neural stem cells (NSCs) monolayered culture to support cell attachment, proliferation, and differentiation. Here,

laminin was added to the ink formulation to study its ability to improve cell-matrix interaction.

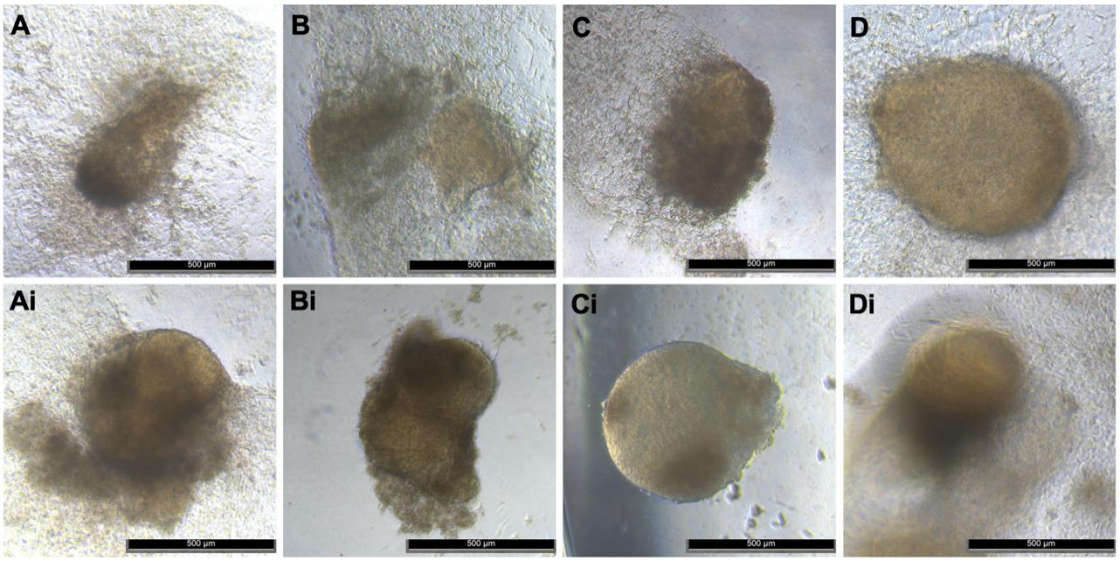

Figure 3.11 H9 spheres encapsulated in different inks after 4 days of culture. Scale bar as indicated.

Bright field macroscope images displayed the morphology of hNSC H9 neurospheres encapsulated in 8 different ink formulations after four days of culture. Most samples (Figure 3.11 A, B, C, D, Ai and Di) showed neurite outgrowth hNSC H9 neurospheres after the fourth day of culture, indicating general good cytocompatibility with the ink formulations. Interestingly, bioinks without laminin showed slightly better neurite outgrowth compared to the formulations containing laminin. Blank sample, free-floating aggregates, cultured in matrix-free culture media, showed no neurite outgrowth.

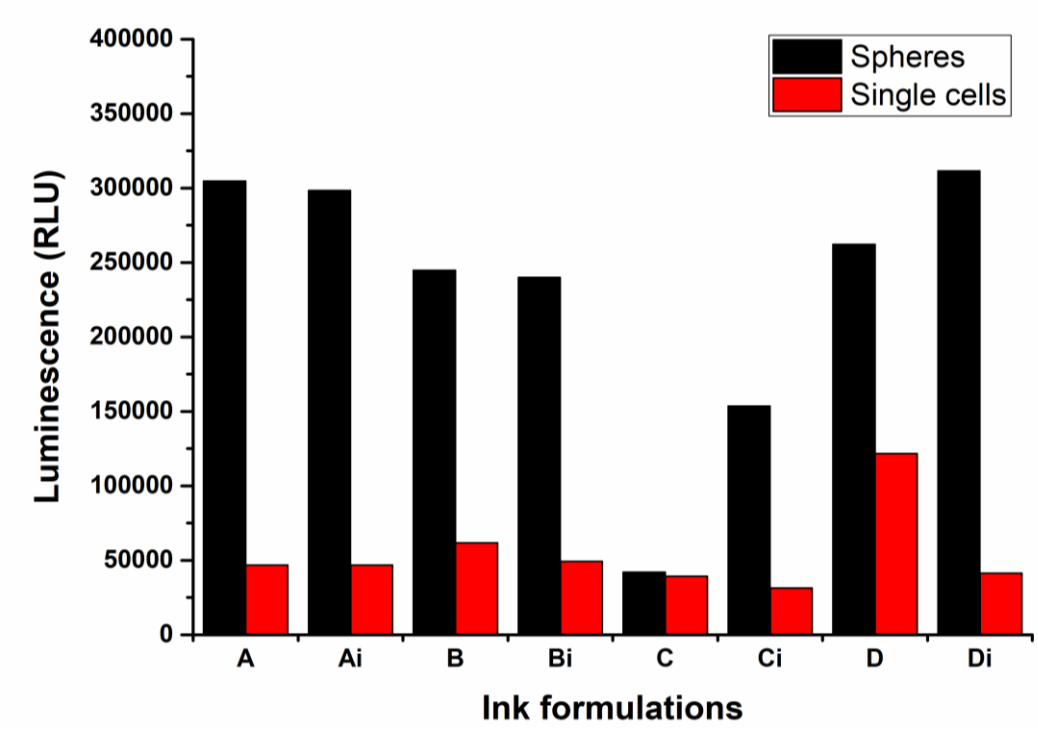

Figure 3.12 Viability of H9 (spheres and single cells) encapsulated in different inks

CellTiter-Glo® 3D viability assay was performed to determine the number of viable hNSC H9 cells in neurospheres and dissociated neurospheres after four days of culture. This method is based on quantitation of the ATP, which is a marker for the presence of metabolically active cells. 16 samples plus three controls and one blankwere used for this assay. Dissociated neurospheres, or 'single cell', were produced by mechanically breaking spheres. *In vitro* cellular viability was performed to confirm cytocompatibility towards hNSC H9 cells (Figure 3.12). All other formulations, except C and Ci, showed high viability of hNSC H9 neurospheres. Dissociated hNSC H9 spheres (single cells) showed low viability in all bioink formulations due to poor cell survival after mechanical stress generated during the dissociation process. This could be due to embryonic stem cell (ESC)-derived human NSCs own nature, as stem cells are known to be a sensitive cell line that can be easily disrupted by mechanical stress.[205] In summary, bioink formulations supported neurite outgrowth from neurospheres. No

significant difference among the bioink tested were noted; yet sample ‘D’ (Figure 3.11D) showed a more uniform neurite outgrowth distribution throughout the sphere.

3.4 Discussion

It is well known that the tissue microenvironment plays an important role in a cell’s fate. Human dermal fibroblast-derived matrix has been reported to support formation of an optimal microenvironment for keratinocyte culture by depositing and rearranging the ECM, as well as secreting many cytokines and growth factors required for keratinocyte attachment and growth.[206] In accordance to that, our data showed that longer period of culture of HDF-PLGMA prior to HaCaT seeding allowed HDF to attach to the matrix, and initiate secretion of signalling molecules and ECM components, which demonstrated to influence the keratinocyte fate and organisation.

The crosstalk between keratinocytes and fibroblasts are well known to be critical for a successful healing process, as keratinocytes stimulate fibroblasts phenotype change and synthesis of growth factors, and fibroblast stimulate keratinocyte proliferation in a double paracrine manner.[207] Therefore, dermal-epidermal skin substitutes containing keratinocytes and fibroblasts incorporated into constructs have the potential to promote the regeneration of dermal and epidermal layers as well as accelerate wound closure, [4] as cultured cells secrete ECM components, cytokines and growth factors to the wound bed, managing wound healing and reducing pain.[207]

In normal skin, expression of proliferation marker Ki67 is observed in the basal layer and immediate suprabasal layers,[208] while cytokeratin is expressed in suprabasal and superficial keratinocytes layers.[209] Cytokeratins are cytoskeleton proteins expressed by keratinocytes during differentiation. Involucrin is considered an early marker of

keratinocyte terminal differentiation[210] expressed in the upper layers of the skin and indicates the signalling between keratinocytes and fibroblasts.[211] The predominant collagen subtype on the skin dermis is collagen type I and III with small amounts of type V and IV in the basement membrane. Collagen IV, along with laminin, plays an important role in cell adhesion, migration, differentiation, and growth. It promotes keratinocyte migration, which is essential for the re-epithelialization of cutaneous wounds. The expression of collagen IV is stronger in the co-culture of keratinocytes and fibroblasts than in the mono-culture of keratinocyte alone, as fibroblasts secrete TGF-β, which induce the synthesis of collagen IV by keratinocytes.[211] Although more in-depth assessment *in vitro* and *in vivo* are needed to prove the therapeutic efficacy of the proposed HaCaT/HDF-PLGMA platform in supporting new tissue formation and epithelial maturation. This proof-of-concept study demonstrated that co-culture of keratinocytes and fibroblasts-PLGMA expressed key epidermal differentiation protein markers of cytokeratin 10, Ki67 and involucrin, indicating successful epidermal stratification. HaCaT keratinocytes were used in this study to fabricate the epidermal compartment of 3D skin model for its reproducibility capability, however, for future *in vivo* studies patient-derived primary cells will be preferred as a biologically relevant option.

There are seven β-tubulin isotypes expressed in human tissue,[212] which participate in the formation of microtubule network. β-tubulin III, class III member of the β-tubulin family specifically localized to neurons, plays an important role in neural differentiation and neurite outgrowth. Therefore, β-tubulin III antibodies has been widely used as a neuron-specific biomarker in developmental neurobiology and stem cell research.[213] S100B is a cytosolic calcium-binding protein that belongs to the S100 protein

family[214] expressed in astrocytes, specific neuronal populations, Schwann cells, and others.[215] hNSC H9 cells also reported to express low level of this glial marker. Study revealed the expression levels of glial markers (~ 1×10^6) was about 50 times lower compared to β-tubulin III (> 50×10^6).[216] Tropomyosin receptor kinase (TrkA, TrkB, and TrkC) are a transmembrane receptors family with tyrosine kinase activity that plays an important role in the development of the mammalian nervous system.[217] Trk receptors are primarily expressed in neuronal lineage of the dorsal root ganglia (DRG). TrkA is a nerve growth factor (NGF) receptor; TrkB is a brain-derived neurotrophic factor (BDNF) receptor; TrkC is a neurotrophin-3 (NT-3) primary receptor.[218]

Neuronal differentiation is characterised by an increase in the expression of several neuron-specific markers including β-tubulin III, MAP2, neurofilaments and doublecortin. [216] MAP2 is a neuron specific protein expressed in immature neural stem cells and neuronal cells. Reports suggest that mice expressed MAP2 shortly after that of βIII-Tubulin. which stabilises the microtubule network in the dendrites of post-mitotic neurons. [219] Expression of homeodomain transcription factor ISLET1 and BRN3A protein has also been reported to indicate differentiation of stem cell lineages into a neurosensory-like lineage.[220] Moreover, the expression of a cytoplasmatic marker, 200 kD Neurofilament (NF200), is associated with large diameter mechanoreceptor and proprioceptor neurons.[221]

It has been demonstrated in the literature that platelet lysate support angiogenesis, neurogenesis and neuroprotection of endogenous neural stem cells (eNSC).[222] HDF secrete multiple signalling molecules, such as PDGF, IGF-1, TGF-β, VEGF, HGF, keratinocyte growth factor (KGF), interleukin (IL-6 and -8), tumour necrosis factor α (TN-α)[223] and ECM components[13] that could influence this process as well.

Although more in-depth assessment *in vitro* and *in vivo* are needed to understand how these cells interact and if this interaction would lead to re-innervation of the wounded skin. The proof-of-concept study here presented demonstrated that co-culture of neuronal spheres and fibroblatsts-PLGMA supported the formation of a 3D nerve networks *in vitro*. Direct contact of fibrobasts and hNSC promoted neurite migration and neuronal maturation.

3.5 Conclusion

Herein, we have demonstrated that the HDF-PLGMA platform established in the previous chapter supported HaCaT differentiation, as well as hNSC-H9 neurosphere neurite outgrowth and neuronal differentiation. HaCaT/HDF-PLGMA expressed involucrin, cytokeratin, collagen III and collagen IV after cultured for two weeks under ALI conditions, confirming the capacity of the platform to promote normal epithelial morphogenesis and differentiation of keratinocytes. Stratification of keratinocytes were also demonstrated my histological analysis. H9/HDF-PLGMA expressed development neuronal markers including MAP2, BRN3A, neurofilament-200, as well as general marker β-tubulin III after three weeks of culture, demonstrating the platform support hNSC-H9 neurosphere neurite outgrowth and neuronal differentiation. Although the co-culture of HaCaT and hNSC-H9 neurosphere together in an HDF-PLGMA construct could not be demonstrated, important findings and challenges that need to be considered in order to progress with this research were reported. Further standardization of the system and characterisation techniques are required in order to incorporate other relevant cells to fabricate more complex structures. Future work will also involve *in vivo* studies to assess the ability of this system to improve re-epithelisation and re-innervation.

3.6 References

[4] R.F. Pereira, C.C. Barrias, P.L. Granja, P.J. Bartolo, Advanced biofabrication strategies for skin regeneration and repair, Nanomedicine (Lond) 8(4) (2013) 603-21.

[13] M. Xue, C.J. Jackson, Extracellular Matrix Reorganization During Wound Healing and Its Impact on Abnormal Scarring, Adv Wound Care (New Rochelle) 4(3) (2015) 119-136.

[58] M. Albanna, K.W. Binder, S.V. Murphy, J. Kim, S.A. Qasem, W. Zhao, J. Tan, I.B. El-Amin, D.D. Dice, J. Marco, J. Green, T. Xu, A. Skardal, J.H. Holmes, J.D. Jackson, A. Atala, J.J. Yoo, *In situ* bioprinting of autologous skin cells accelerates wound healing of extensive excisional full-thickness wounds, Scientific Reports 9(1) (2019) 1-15.

[91] W.L. Ng, J.T.Z. Qi, W.Y. Yeong, M.W. Naing, Proof-of-concept: 3D bioprinting of pigmented human skin constructs, Biofabrication 10(2) (2018) 025005.

[94] W. Lee, J.C. Debasitis, V.K. Lee, J.-H. Lee, K. Fischer, K. Edminster, J.-K. Park, S.-S. Yoo, Multi-layered culture of human skin fibroblasts and keratinocytes through three-dimensional freeform fabrication, Biomaterials 30(8) (2009) 1587-1595.

[95] V. Lee, G. Singh, J.P. Trasatti, C. Bjornsson, X. Xu, T.N. Tran, S.-S. Yoo, G. Dai, P. Karande, Design and fabrication of human skin by three-dimensional bioprinting, Tissue Engineering, Part C: Methods 20(6) (2014) 473-484.

[97] D. Min, W. Lee, I.H. Bae, T.R. Lee, P. Croce, S.S. Yoo, Bioprinting of biomimetic skin containing melanocytes, Experimental Dermatology 27(5) (2018) 453-459.

[101] N. Cubo, M. Garcia, J.F. del Cañizo, D. Velasco, J.L. Jorcano, 3D bioprinting of functional human skin: production and *in vivo* analysis, Biofabrication 9(1) (2016) 015006.

[105] C. Intini, L. Elviri, J. Cabral, S. Mros, C. Bergonzi, A. Bianchera, L. Flammini, P. Govoni, E. Barocelli, R. Bettini, M. McConnell, 3D-printed chitosan-based scaffolds: An *in vitro* study of human skin cell growth and an *in-vivo* wound healing evaluation in experimental diabetes in rats, Carbohydrate Polymers 199 (2018) 593-602.

[106] Y. Shi, T.L. Xing, H.B. Zhang, R.X. Yin, S.M. Yang, J. Wei, W.J. Zhang, Tyrosinase-doped bioink for 3D bioprinting of living skin constructs, Biomedical Materials 13(3) (2018) 035008.

[107] P. Admane, A.C. Gupta, P. Jois, S. Roy, C.C. Lakshmanan, G. Kalsi, B.

Bandyopadhyay, S. Ghosh, Direct 3D bioprinted full-thickness skin constructs recapitulate regulatory signaling pathways and physiology of human skin, Bioprinting 15 (2019) e00051.

[114] B.S. Kim, J.-S. Lee, G. Gao, D.-W. Cho, Direct 3D cell-printing of human skin with functional transwell system, Biofabrication 9(2) (2017) 025034.

[115] B.S. Kim, G. Gao, J.Y. Kim, D.W. Cho, 3D cell printing of perfusable vascularized human skin equivalent composed of epidermis, dermis, and hypodermis for better structural recapitulation of native skin, Advanced Healthcare Materials 8(7) (2019) 1801019.

[116] B.S. Kim, Y.W. Kwon, J.-S. Kong, G.T. Park, G. Gao, W. Han, M.-B. Kim, H. Lee, J.H. Kim, D.-W. Cho, 3D cell printing of *in vitro* stabilized skin model and in *vivo* pre-vascularized skin patch using tissue-specific extracellular matrix bioink: a step towards advanced skin tissue engineering, Biomaterials 168 (2018) 38-53.

[117] K. Derr, J. Zou, K. Luo, M.J. Song, G.S. Sittampalam, C. Zhou, S. Michael, M. Ferrer, P. Derr, Fully three-dimensional bioprinted skin equivalent constructs with validated morphology and barrier function, Tissue Engineering, Part C: Methods 25(6) (2019) 334-343.

[135] W. Wan, F. Cai, J. Huang, S. Chen, Q. Liao, A skin-inspired 3D bilayer scaffold enhances granulation tissue formation and anti-infection for diabetic wound healing, Journal of Materials Chemistry B 7(18) (2019) 2954-2961.

[193] B. Laverdet, A. Danigo, D. Girard, L. Magy, C. Demiot, A. Desmoulière, Skin innervation: important roles during normal and pathological cutaneous repair, Histol Histopathol 30(8) (2015) 875-92.

[194] A. Sebastian, S.W. Volk, P. Halai, J. Colthurst, R. Paus, A. Bayat, Enhanced Neurogenic Biomarker Expression and Reinnervation in Human Acute Skin Wounds Treated by Electrical Stimulation, Journal of Investigative Dermatology 137(3) (2017) 737-747.

[195] S.G. Gürgen, O. Sayın, F. Cetin, A. Tuç Yücel, Transcutaneous electrical nerve stimulation (TENS) accelerates cutaneous wound healing and inhibits pro-inflammatory cytokines, Inflammation 37(3) (2014) 775-84.

[196] T. Weng, P. Wu, W. Zhang, Y. Zheng, Q. Li, R. Jin, H. Chen, C. You, S. Guo, C. Han, X. Wang, Regeneration of skin appendages and nerves: current status and further challenges, Journal of Translational Medicine 18(1) (2020) 53.

[197] Y.J. Choi, Y.J. Jun, D.Y. Kim, H.G. Yi, S.H. Chae, J. Kang, J. Lee, G. Gao, J.S. Kong, J. Jang, W.K. Chung, J.W. Rhie, D.W. Cho, A 3D cell printed muscle construct with tissue-derived bioink for the treatment of volumetric muscle loss, Biomaterials 206 (2019) 160-169.
[198] S. Werner, T. Krieg, H. Smola, Keratinocyte–Fibroblast Interactions in Wound Healing, Journal of Investigative Dermatology 127(5) (2007) 998-1008.
[199] S.N. Menon, J.A. Flegg, S.W. McCue, R.C. Schugart, R.A. Dawson, D.L.S. McElwain, Modelling the interaction of keratinocytes and fibroblasts during normal and abnormal wound healing processes, Proceedings. Biological sciences 279(1741) (2012) 3329-3338.
[200] B. Russo, N.C. Brembilla, C. Chizzolini, Interplay Between Keratinocytes and Fibroblasts: A Systematic Review Providing a New Angle for Understanding Skin Fibrotic Disorders, Frontiers in immunology 11 (2020) 648-648.
[201] S. Sart, A.-C. Tsai, Y. Li, T. Ma, Three-dimensional aggregates of mesenchymal stem cells: cellular mechanisms, biological properties, and applications, Tissue engineering. Part B, Reviews 20(5) (2014) 365-380.
[202] J. Imitola, K. Raddassi, K.I. Park, F.J. Mueller, M. Nieto, Y.D. Teng, D. Frenkel, J. Li, R.L. Sidman, C.A. Walsh, E.Y. Snyder, S.J. Khoury, Directed migration of neural stem cells to sites of CNS injury by the stromal cell-derived factor 1 /CXC chemokine receptor 4 pathway, Proceedings of the National Academy of Sciences 101(52) (2004) 18117-18122.
[203] M. Moors, J.E. Cline, J. Abel, E. Fritsche, ERK-dependent and -independent pathways trigger human neural progenitor cell migration, Toxicol Appl Pharmacol 221(1) (2007) 57-67.
[204] H.J. Kim, M.R. Shaker, B. Cho, H.M. Cho, H. Kim, J.Y. Kim, W. Sun, Dynamin-related protein 1 controls the migration and neuronal differentiation of subventricular zone-derived neural progenitor cells, Scientific Reports 5(1) (2015) 15962.
[205] J. Tower, Stress and stem cells, Wiley interdisciplinary reviews. Developmental biology 1(6) (2012) 789-802.
[206] C.-W. Wong, C.F. LeGrand, B.F. Kinnear, R.M. Sobota, R. Ramalingam, D.E. Dye, M. Raghunath, E.B. Lane, D.R. Coombe, In Vitro Expansion of Keratinocytes on Human Dermal Fibroblast-Derived Matrix Retains Their Stem-Like Characteristics, Scientific Reports 9(1) (2019) 18561.

[207] H. Savoji, B. Godau, M.S. Hassani, M. Akbari, Skin Tissue Substitutes and Biomaterial Risk Assessment and Testing, Frontiers in Bioengineering and Biotechnology 6(86) (2018).
[208] G.K. Patel, C.H. Wilson, K.G. Harding, A.Y. Finlay, P.E. Bowden, Numerous Keratinocyte Subtypes Involved in Wound Re-Epithelialization, Journal of Investigative Dermatology 126(2) (2006) 497-502.
[209] G.N. Van Muijen, S.O. Warnaar, M. Ponec, Differentiation-related changes of cytokeratin expression in cultured keratinocytes and in fetal, newborn, and adult epidermis, Exp Cell Res 171(2) (1987) 331-45.
[210] H. Vala, T. Carvalho, C. Pinto, M.A. Pereira, J.R. Mesquita, C.P. M, L. Ferrer, D. Fondevila, Immunohistochemical Studies of Cytokeratins and Differentiation Markers in Bovine Ocular Squamous Cell Carcinoma, Vet Sci 7(2) (2020).
[211] S. Nayak, S. Dey, S.C. Kundu, Skin Equivalent Tissue-Engineered Construct: Co-Cultured Fibroblasts/ Keratinocytes on 3D Matrices of Sericin Hope Cocoons, PLoS ONE 8(9) (2013) e74779.
[212] E.-M. Jouhilahti, S. Peltonen, J. Peltonen, Class III beta-tubulin is a component of the mitotic spindle in multiple cell types, The journal of histochemistry and cytochemistry : official journal of the Histochemistry Society 56(12) (2008) 1113-1119.
[213] M.K. Lee, J.B. Tuttle, L.I. Rebhun, D.W. Cleveland, A. Frankfurter, The expression and posttranslational modification of a neuron-specific beta-tubulin isotype during chick embryogenesis, Cell Motil Cytoskeleton 17(2) (1990) 118-32.
[214] D.M. Murray, Chapter 13 - Biomarkers in neonatal hypoxic–ischemic encephalopathy—Review of the literature to date and future directions for research, in: L.S. de Vries, H.C. Glass (Eds.), Handbook of Clinical Neurology, Elsevier2019, pp. 281-293.
[215] J. Kato, C.I. Svensson, Chapter Nine - Role of Extracellular Damage-Associated Molecular Pattern Molecules (DAMPs) as Mediators of Persistent Pain, in: T.J. Price, G. Dussor (Eds.), Progress in Molecular Biology and Translational Science, Academic Press2015, pp. 251-279.
[216] L.E. Oikari, R.K. Okolicsanyi, A. Qin, C. Yu, L.R. Griffiths, L.M. Haupt, Cell surface heparan sulfate proteoglycans as novel markers of human neural stem cell fate determination, Stem Cell Research 16(1) (2016) 92-104.
[217] B. Stoleru, A.M. Popescu, D.E. Tache, O.M. Neamtu, G. Emami, L.G. Tataranu,

A.S. Buteica, A. Dricu, S.O. Purcaru, Tropomyosin-receptor-kinases signaling in the nervous system, Maedica 8(1) (2013) 43-48.
[218] A.M. Fagan, H. Zhang, S. Landis, R.J. Smeyne, I. Silos-Santiago, M. Barbacid, TrkA, but not TrkC, receptors are essential for survival of sympathetic neurons in vivo, The Journal of neuroscience : the official journal of the Society for Neuroscience 16(19) (1996) 6208-6218.
[219] A.R. Murphy, J.M. Haynes, A.L. Laslett, N.R. Cameron, C.M. O'Brien, Three-dimensional differentiation of human pluripotent stem cell-derived neural precursor cells using tailored porous polymer scaffolds, Acta Biomaterialia 101 (2020) 102-116.
[220] N. Gunewardene, N.V. Bergen, D. Crombie, K. Needham, M. Dottori, B.A. Nayagam, Directing human induced pluripotent stem cells into a neurosensory lineage for auditory neuron replacement, Biores Open Access 3(4) (2014) 162-75.
[221] A.J. Alshawaf, S. Viventi, W. Qiu, G. D'Abaco, B. Nayagam, M. Erlichster, G. Chana, I. Everall, J. Ivanusic, E. Skafidas, M. Dottori, Phenotypic and Functional Characterization of Peripheral Sensory Neurons derived from Human Embryonic Stem Cells, Scientific Reports 8(1) (2018) 603.
[222] Y. Hayon, O. Dashevsky, E. Shai, D. Varon, R.R. Leker, Platelet lysates stimulate angiogenesis, neurogenesis and neuroprotection after stroke, Thromb Haemost 110(2) (2013) 323-30.
[223] J.N. Mansbridge, K. Liu, R.E. Pinney, R. Patch, A. Ratcliffe, G.K. Naughton, Growth factors secreted by fibroblasts: role in healing diabetic foot ulcers, Diabetes Obes Metab 1(5) (1999) 265-79.

4 Chapter

Electrofluidic control of bioactive molecule delivery into soft tissue models based on gelatin methacryloyl hydrogels using threads and surgical sutures

The work presented in this chapter was adapted from the manuscript published in the Journal Scientific Reports 10, 7120 (2020). https://doi.org/10.1038/s41598-020-63785-z by Cabot, J.M., Daikuara, L.Y., Yue, Z. et al. Electrofluidic control of bioactive molecule delivery into soft tissue models based on gelatin methacryloyl hydrogels using threads and surgical sutures. (The authors Cabot, J.M., Daikuara, L.Y. equally contributed to this published work)

Table of Contents

4.1 Introduction

Thread and textiles have recently gained considerable attention as low-cost substrates for microfluidics and biosensor applications, based upon their mechanical strength and the ability to facilitate and direct fluid movement. Fluid flow in threads arise from wicking processes as a result of capillary forces generated within the gaps between directionally aligned fibres. This capillary action subsequently drives the fluid along the thread, and it is directly related to the material hydrophilicity on the surface.[136] For instance, the presence of waxes such as those composed of long fatty acid chains found on some natural fibres like cotton as well as contamination on synthetic fibres such as polyester have been observed to interfere with wicking in threads[142, 143] Threads have been used in this way within a variety of applications, including bioanalysis,[137-143] and embedded in a hydrogel as a network for chemotaxis studies[144] or multilayer feeding of cell cultures.[145]

Hydrogels can be produced to simulate the characteristics of native extracellular matrices and provide a 3D support for cellular growth and tissue formation.[224, 225] The ability of hydrogels to mimic the mechanical properties of soft tissue has seen them extensively applied in biomedical applications,[226] particularly presenting as an attractive substrate for biomedical implants[227, 228] tissue engineering,[225, 229] and as a therapeutic delivery platform.[230] Among the natural polymers, gelatin methacryloyl (GelMA) presents several interesting advantages, as it is in fact denatured collagen and is a photopolymerizable hydrogel.[231-235] The mechanical properties of a variety of soft tissues, including neural tissue, vascularization, cartilage, bone, skin,

skeletal muscle, cardio, liver, and kidney can be reproduced through use of appropriate GelMA concentrations and the photo-crosslinking conditions.[124, 235-238] Moreover, GelMA's mechanical properties and application can be further expended by incorporating additional materials.[239] Here we use GelMA based hydrogels as tissue models to demonstrate an effective way to control the delivery and spatial distribution of biomolecules.

Threads can be readily integrated into the gel, and they provide for an easy and robust way to transport liquid in or out of a gel. Direct application of biomolecules onto a thread or yarn is trivial and enables dispatch at a targeted location.[138] Herein, we demonstrated the use of electrofluidics – precise control and manipulation of fluids at the microscale by the use of an external electric field – on threads/suture to deliver biomolecules into and throughout a gel, via control of an applied electric field, to provide a simple approach involving no moving parts or pumps.

This project was part of a collaboration between ARC Centre of Excellence for Electromaterials Science (ACES) University of Tasmania (UTAS) and University of Wollongong (UOW) nodes, where Dr Joan Marc Cabot and I, Luciana Yumiko Daikuara, contributed equally to the published work. I was responsible for the selection of sutures, synthesise / preparation of the hydrogel and the experimental work, while Dr Joan Marc Cabot was responsible for the system design and data analysis. Despite being peripherally related to the overall PhD theme; this system could be potentially integrated to the PLGMA matrix by printing the 3D skin cells-PLGMA on top of the suture for precise delivery of growth factors and cells to the sutured wound.

4.2 Experimental Section

4.2.1 Materials and reagents

Key materials used in this chapter are introduced in detail as follow.

Materials	Source	Cat no
Hydrogel		
Gelatin (porcine skin, Type A, 300 Bloom)	Sigma-Aldrich	G2500
Methacrylic anhydride	Sigma-Aldrich	P5927
Lithium phenyl-2,4,6-trimethylbenzoylphosphinate (LAP)	Sigma-Aldrich	900889
Biomolecules		
Dexamethasone 21-phosphate disodium salt (DSP)	Sigma-Aldrich	D9184
Fluorescein	Sigma-Aldrich	F6377
Riboflavin	Sigma-Aldrich	F6750
Rhodamine B	Sigma-Aldrich	R6626
Fluorescein isothiocyanate - bovine serum albumin (FITC-BSA)	Sigma-Aldrich	
Fluorescein isothiocyanate - dextran (FITC-dextran)	Sigma-Aldrich	
General reagents		
4-(2-hydroxyethyl)piperazine-1-ethanesulfonic acid (HEPES)	Sigma-Aldrich	H4034
Phosphate buffered saline (PBS)	Life Technologies	14190136
Tris(hydroxymethyl)aminomethane (TRIS)	Sigma-Aldrich	252859
Acetonitrile	Sigma-Aldrich	271004
Ammonium acetate	Ajax FineChem	631-61-8
Milli-Q water with a resistivity of 18.2 MΩ cm		
Thread / Surgical suture		
Acrylic (diameter (Ø) 671 ± 58 µm, 4 ply, Marvel Soft Baby)	Bella Baby	
Polyester surgical suture (USP 4/0)	KeeboMed Inc	
Lactomer surgical suture (USP 3/0 Polysorb)	Covidien	
Poliglecaprone 25 surgical suture (USP 3/0 Monocryl)	Ethicon	
Polypropylene surgical suture (USP 3/0 Prolene)	Ethicon	
Nylon surgical suture (USP 3/0 Ethilon)	Ethicon	
Silk surgical suture (USP 3/0)	Ethicon	
Polyglactin 910 surgical suture (USP 3/0 Vicryl)	Ethicon	
Polyamide surgical suture (USP 0 Supramid)	SMI AG	
Polyglycolic acid surgical suture (USP 0 Surgicryl PGA)	SMI AG	

4.2.2 Preparation of GelMA hydrogels

GelMA hydrogels were prepared by dissolving various amounts of GelMA (2.5-7.5%) in two buffer solutions, PBS (5.0%) and TRIS/HEPES (5 mM), respectively. For each solution, LAP was then added to the solution with a final concentration of 0.06%, loaded into a customized hydrogel chamber and crosslinked upon UV light (400 nm) exposure for 45 seconds, unless specified otherwise. GelMA volume was kept constant at 15 mm^3 (2.5 × 2.5 × 2.4 mm, length × width × height).

4.2.3 Mechanical properties of GelMA hydrogels

The mechanical properties of hydrogels were measured by indentation (EZ-S mechanical tester, Shimadzu) using a compression mode. Each sample was prepared by casting a polymer solution (15μl) in a 2.5×2.5×2.5 mm custom mold. A cylindrical flat-ended stainless-steel indenter (990 μm in diameter) was attached to a 10 N load cell and programmed to apply force to the hydrogel surface at a controlled displacement rate of 0.5 mm/min. The Young's modulus of the hydrogel was calculated through the slope of the applied force against indentation depth (0-100 μm) plot. The radius of the indenter tip was 0.495 mm. The slope of the linear fit was then used to calculate the hydrogel modulus (E). Young's modulus was calculated for 2 different GelMA concentration (5.0, 7.5%) and 3 cross-linking times (30, 45, and 60 s). 5 replicates were carried for each determination.

4.2.4 Nuclear Magnetic Resonance (NMR)

NMR was performed to verify the degree of functionalization of gelatin methacryloyl (GelMA). NMR spectra were acquired at 30 ^{o}C using a Bruker Avance III HD 400 MHz NMR spectrometer (Bruker BioSpin Corp.), and the data were analyzed using Bruker Topspin software 3.7.5. For NMR analysis, GelMA samples (10 mg/mL) and gelatin samples (4 mg/mL) were prepared in deuterium oxide (Sigma-Aldrich, Australia). The lysine peak (2.8–3.0 ppm) was used to confirm the methacrylation degree. The phenylalanine peak (7.1–7.4 ppm) was chosen to normalize the intensity of the lysine peak. The lysine peak shown in Figure 4.S1 confirmed a high methacrylation degree of 87 ± 5%, calculated according to the ratio of the relative peak integrations of the lysine protons in GelMa and gelatin.

4.2.5 Platform and experiment setup

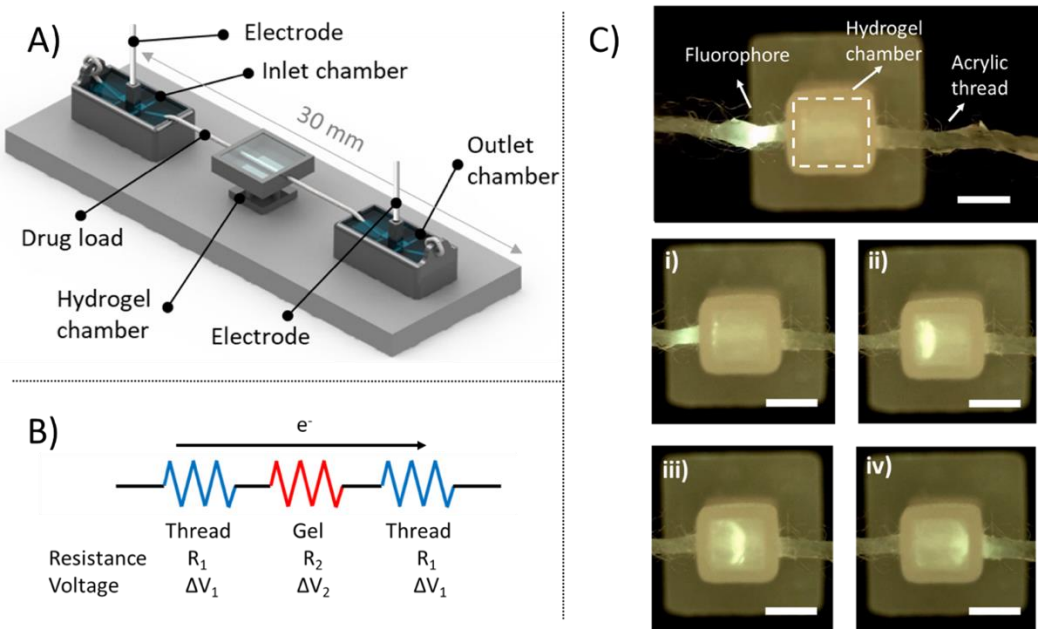

Figure 4.1 Schematic of the suture-GelMA hydrogel delivery platform.
(A) consisting of two buffer chambers with hydrogel chamber sitting in the middle, and a suture/thread wetted with preferred buffer to connect both liquid and hydrogel.

Fluorophore (fluorescein) was loaded at 5 mm before the hydrogel chamber. Electric field was applied between inlet and outlet chambers. (B) A simple circuit diagram representing the contribution of each electrical component of the platform when electric field is applied. (C) Sequence of images depicting the parts and delivery process of fluorescein (a model compound) in GelMA at (i) 0.00, (ii) 2.30, (iii) 4.30 and (iv) 7.40 min. Images were picked from the top of the platform at 510 nm emission filter. Conditions: 5% GelMA and 45s cross-linking (stiffness of 4.3 kPa), sample loading: 2 μL fluorescein drop at 1.0 μg/mL, current of 100 μA. 5 mM Tris/HEPES buffer was used for both inlet/outlet chambers and GelMA. Scale bar is 2 mm. Data presented here are based on 6 replicates.

As illustrated in Figure 4.1A, experiments were conducted in a suture-GelMA hydrogel-based device designed by Joan Marc Cabot. The platform consisted of two 3D printed inlet and outlet chamber at each end filled with 500 μL of 5 mM Tris/HEPES, a 3D printed hydrogel chamber sitting in the middle with 15 μL of 5% GelMA cross-linked for 45 s, and a 3D printed base to allow good alignment and support of these features. GelMA Inlet and outlet chambers had a tubular guide to introduce the electrode, ring to tie in the thread, and a basin. The total length of the thread from the inlet to the outlet chamber was 30 mm, with 2.5mm embedded into the hydrogel. The hydrogel chamber was 2.5 × 2.5 × 2.5 mm (xyz), had two holes in each side allowing the thread to go in and out of the hydrogel. Features were designed using SolidWorks CAD software (SolidWorks Corp., Dassault Systemes). Designs were 3D printed using an Eden 260VS (Stratasys) with VeroClear or VeroWhite build material, and SUP707 water soluble support. SUP707 support material was removed by agitation in 2 % NaOH for 2 hours using a benchtop orbital shaker, followed by 4-6 hours in water. Finally, printed parts were rinsed with Milli-Q water. To interconnect the system, a plasma-treated acrylic or surgical suture was placed at the front part of the inlet chamber, along the hydrogel

chamber up to the outlet chamber. Prior to analysis, all threads and sutures were plasma treated for 1 min at 18 W in 0.2 Torr using Harrick Plasma Cleaner PDC-32G (Harrick Plasma) connected to a PlasmaFlo Gas Flow Mixer PDC-FMG. A power supply, HVS448 High Voltage Sequencer 3000D-LC (LabSmith) in conjunction with a voltage modulator were used to generate an electric field between the electrodes immersed in the inlet and outlet reservoirs. The output of the sequencer (voltage, current and conductivity) was controlled and measured by a computer through the Sequence Software (Labsmith).

4.2.6 Bioactive molecule delivery in suture-GelMA hydrogel

Fluorescein velocities were measured at 3 GelMA concentrations (2.5, 5.0, 7.5%) and 6 crosslinking time (0, 10, 20, 30, 45 and 60 seconds). Fluorescein was prepared in the same buffer solution as the GelMA hydrogel and reservoirs (5 mM Tris/HEPES). A drop (2 μL) of fluorescein compound was placed in the acrylic thread (shown as 'drug load' in Figure 4.1A). An electric field was applied at a constant current of 100 μA unless specified otherwise. 5% GelMA with 45 s cross-linking and the same electrofluidic conditions and buffer conditions were carried out for the flow delivery control.

To test bioactive delivery, the same experiment was repeated using rhodamine B, riboflavin, FITC-BSA, FITC-dextran. Resistance comparation was carried out using 4 different buffers (5 mM Tris/HEPES, 50 mM Tris/HEPES, 2.5 % PBS, and 5% PBS). Drug delivery of fluorescein in several 9 suture threads were measured at 250 μA of current, 5% PBS buffer and 5% GelMA with 45 s cross-linking. Results are presented as the average of 6 replicates. Temperature was monitored using an infrared camera (Ex

series with MSX, FLIR Systems) and kept at 25 ± 1ºC. A USB microscope AM4113T-GFBW (Dino-Lite Premier, Clarkson) fitted with a blue light-emitting diode for excitation and a 510 nm emission filter was used to take fluorescence images and videos (resolution of 1.3M pixels and 30fps). ImageJ (National Institutes of Health) was used to analyse the region of interest (ROI) and then monitor the mean fluorescence intensity value of the ROI versus time. The data was acquired from the moment the fluorescent compound band entered the hydrogel. This software was also used to determine the band position at each time, and velocity was calculated using division of band displacement by time. In all cases, position was referenced to the front part of the band.

A similar experiment was performed to study the delivery of dexamethasone 21-phosphate disodium salt (DSP) using 5% GelMA with 45 s cross-linking and 5% PBS as buffer. A drop (2 µL) of DSP (1.0 mg/mL) was placed on medical surgicryl PGA suture, and an electric field was applied at a constant current of 250 µA. Buffered solutions from the inlet and outlet chambers were collected from three experiments performed at two different running times (1 and 2 hours). Triplicates of the same experiment without electric field were carried out for the blank. Then the buffer solution from the chambers were collected. DSP content in all samples collected were measured by high pressure liquid chromatography (HPLC).

4.2.7 HPLC analysis of drug-released samples

An Agilent 1260 Infinity HPLC system equipped with an Atlantis T3 5 µm 4.6 × 250 mm C18 Column (Waters) was employed for the study. A gradient HPLC method was used for the analysis of DSP using a UV detector at 242 nm. The mobile phase comprised A (20 mM ammonium acetate) and B (acetonitrile) with a flow rate of 1

mL/min. The initial mobile phase was maintained at 23% B for 5 min, and then changed linearly to 100% B in 1 min (5-6 min), maintained at 100% B for 4 min (6-10 min), and finally, reduced linearly to 23% B in 2 min (10-12 min) and maintained at 23% B for 4 min (12-16 min). The injection volume is 10 µL, and each sample was filtered through a 0.22 µm regenerated cellulose syringe filter (Phenomenex Australia Pty Ltd). DSP concentration within the chambers were determined using the parameters obtained from the calibration curve (70 - 1500 ppb).

4.3 Results

4.3.1 Mechanical properties of soft biological tissues

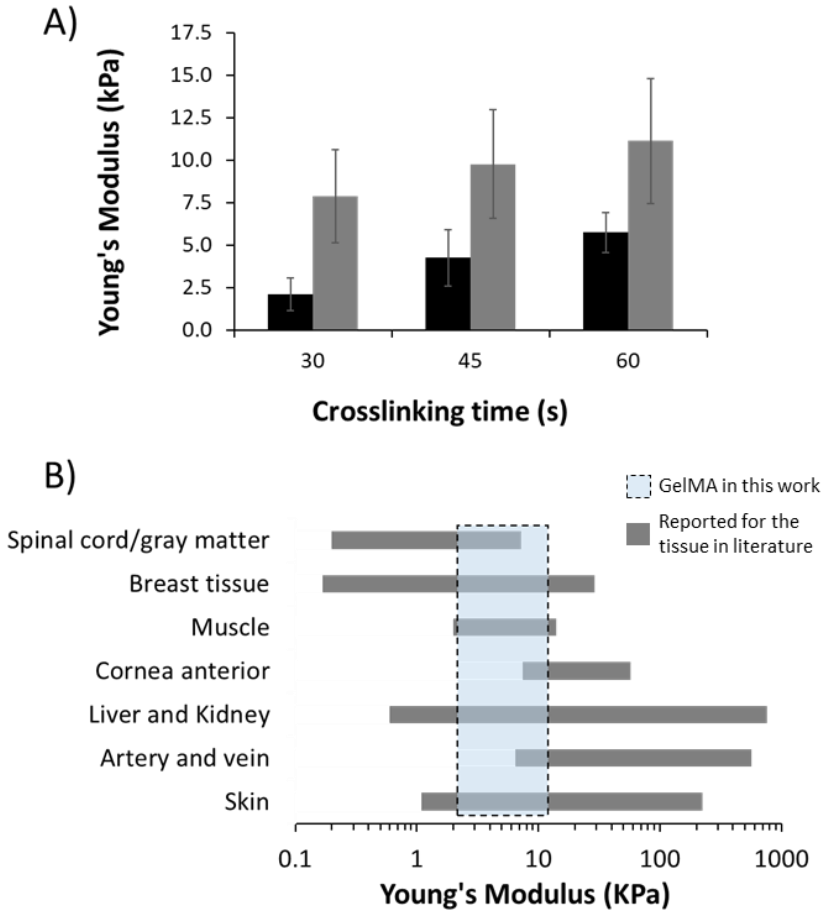

Figure 4.2 Tailoring mechanical properties of gelatin methacryloyl (GelMA) hydrogels to match soft tissues.

(A) Young's modulus for the hydrogels prepared from 5.0 (black) and 7.5 % GelMA (grey). Error bars are based on the standard deviation of 5 replicates. (B) Comparison of Young's modulus developed in this work (dashed box) with the soft biological tissues (grey bars). Dashed box represents the region for 5.0-7.5% GelMA. The Young's modulus values obtained for the GelMA hydrogels were compared with the values reported within the literature for 7 soft biological tissues[240, 241].

The mechanical properties of the GelMA hydrogel affect the diffusion and delivery of bioactive species.[242] GelMA is often described as mechanically tunable.[232, 243,

244] Changes in degree of modification and photo-crosslinking conditions cause different rates and extent of reaction, thus altering the mechanical properties of GelMA.[245] In this work, the Young's modulus was determined for 2 GelMA concentrations. Figure 4.2A shows a Young's modulus of 2.1 ± 1.0, 4.3 ± 1.7, 5.7 ± 1.2 kPa for the 5.0% GelMA hydrogel photo-crosslinked for 30, 45 and 60s, respectively, and 7.9 ± 2.7, 9.8 ± 3.2, 11.1 ± 3.7 kPa for the 7.5% GelMA hydrogel photo-crosslinked for 30, 45 and 60s, respectively. As seen in Figure 4.2B, values obtained matched those of several soft tissues, particularly normal skin, liver and kidney. The use of lower concentration GelMA (5%) provides gels that more closely mimic softer tissues such as spinal cord, grey matter or muscle, with the highest concentration gels (7.5%) being closer to cornea anterior, artery and vein.

4.3.2 Biomolecule delivery in GelMA hydrogels

4.3.2.1 Transport process

To achieve an effective flow and controlled biomolecule migration within hydrogels, plasma-treated (hydrophilic) acrylic thread (diameter to 670 μm) was used. As described in the Theory section available within the supplementary information, biomolecule transport is directly proportional to the voltage. Nevertheless, the rise in voltage must be compensated with a reduction in current, otherwise the power (product of voltage and current) can generate Joule heating. Therefore, in order to reduce the generated current and minimize Joule heating effects, a low conductivity buffer (5 mM Tris/HEPES, 62.72 Ω m, pH 7.8, ionic strength 3.38 mM) was used. The temperature in each set-up was monitored using an infrared camera and was shown to be 25 ± 1ºC. This suggests the absence of any significant Joule effects during delivery.

Figure 4.1C shows a schematic representation of the hydrogel chamber before solute delivery (in this example fluorescein (FL), a negatively charged fluorophore), with FL shown dropped directly onto the inlet acrylic thread. As soon as a current of 100 μA was applied, the FL band migrated towards the anode (+) along the thread. When the band entered the hydrogel, the velocity decreased as a result of the increased viscosity and the dissipation of the field within the gel. FL then spreads radially from the thread, to form a semi-sphere. Finally, as the band exits the gel the FL band becomes refocused onto the outlet thread. This can be viewed as a Movie in the Supplementary Information, which shows the delivery process. Less than 8 minutes was needed to transfer the FL band along the thread through the hydrogel, and then exit on the thread. FL travelled through the hydrogel at a constant velocity of 7.17 ± 0.50 μm s^{-1} (n = 6).

4.3.2.2 Delivery of bioactive species

A range of exposure times and GelMA concentrations were tested in order to evaluate delivery with respect to gel stiffness. Shown in Figure 4.S3 are the data for FL velocity within 2.5, 5.0, and 7.5 % GelMA, as a function of crosslinking time from 0, 10, 20, 30, 45 and 60 seconds. The velocities for GelMA 5% and 7.5% were compared with the respective Young's moduli and are shown in Figure 4.2A. To compare results, all experiments were carried out using a 100 μA current. The velocity decreased linearly with increasing the hydrogel stiffness as characterized by respective Young's modulus. A velocity of 9.3 ± 0.4 μm s^{-1} at a Young's modulus of 2.1 kPa was found, compared with 11.2 ± 0.4 μm s^{-1} at zero crosslinking (Figure 4.3A).

In contrast, for a tougher hydrogel with Young's modulus of 11.1 kPa, velocity was much slower (3.6 ± 0.6 μm s^{-1}). Increasing the concentration of a macromer, as is the

case with GelMA, results in formation of more densely crosslinked polymer network that is responsible for an increase in stiffness and therefore a reduction in ion mobility[233, 235] – similar to the influence of agarose concentration in gel electrophoresis, commonly known as sieving matrix. A resultant reduction in the ion mobility produced sharper solute bands within the gel (Figure 4.3Bi-ii). An increase of cross-linking caused an increase in stiffness within the hydrogel, hindering the delivery. This phenomenon was observed within hydrogels of stiffness > 15 kPa.

Under the same conditions, a higher electric field provides faster solute delivery, up to a point, when if the electric field is too high, the infusion of biomolecules into the hydrogel cannot keep up with electrolyte movement and so accumulates at the thread-gel interface. This could cause a localized increase in ion concentration and therefore increase Joule heating and posterior hydrogel swelling. This was the case for a hydrogel with stiffness of 11.1 kPa at a current of 150 μA. Normal delivery was observed for the first two minutes, at which point the hydrogel began to swell, causing disruption of the band (Figure 4.3Biii).

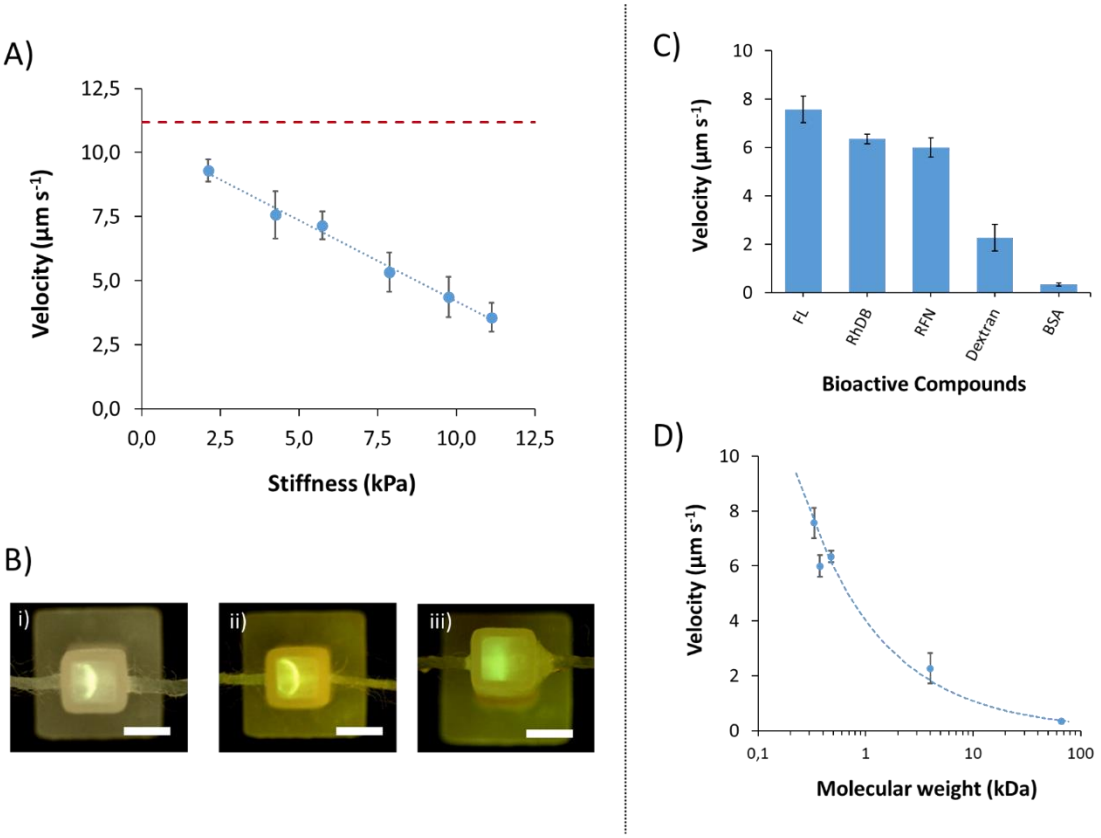

Figure 4.3 Delivery in soft tissue models based on GelMA hydrogels.

In all cases 0.5 pg of sample was dropped on acrylic thread and 100 µA was applied for electric field (unless specified otherwise). 5 mM Tris/HEPES buffer was used for both inlet/outlet chambers and GelMA. Error bars are based on the standard deviation of 3 replicates. (A) Speed of fluorescein (FL, a model compound) as a function of the stiffness (Young's modulus). Trend line was y = - 0.63x + 10.52, R-squared = 0.9912. Red dashed line represents the velocity at 0 crosslinking (11.2 ± 0.4 µm s^{-1}). (B) Representative pictures were taken for (i) 5% GelMA (45s cross-link, stiffness of 4.3 kPa) at 100 µA, (ii) 7.5% GelMA (30 s cross-link, 7.9 kPa) at 100 µA, and (iii) 7.5% GelMA (60 s cross-link, 11.1 kPa) at 150 µA. Scale bar is 2.5 mm (C) Velocity of 5 different compounds and bioactive components: fluorescein (FL), rhodamine B (RhDB), riboflavin (RFN), BSA, dextran) in a GelMA hydrogel with a stiffness of 4.3 kPa, conditions were the same as Figure 4.1. (D) Velocity as a function of the molecular weight of the compound. Speed in hydrogel declines with molecular weight following a trend of y = 4.02x-0.57, R-squared = 0.9879.

Figure 4.3C-D show the velocities of several bioactive molecules within the GelMA hydrogel, ranging from small metabolites to polysaccharides, to proteins, each with different charge and functionality. While migration was relatively rapid along the acrylic thread, each slowed rapidly as they entered the hydrogel. Small molecules such as FL, Rhodamine B (RhDB), and Riboflavin (RFN) migrated faster, with velocities of 7.57 ± 0.55, 6.34 ± 0.20, 5.99 ± 0.40 $\mu m\ s^{-1}$, respectively. Different migration directions were observed depending on the solute charge. For instance, FL (-) migrated to the anode, whereas the polarity needed to be switched for delivery of RhDB (+). Velocities for larger molecules such as dextran (4kDa, 2.26 ± 0.55 $\mu m\ s^{-1}$) and BSA (66.5 kDa, 0.33 ± 0.07 $\mu m\ s^{-1}$) were substantially slower. This was caused by the hydrogel matrix, where smaller molecules moved and migrated more rapidly, as they could move freely through the polymer networks. Compared with small molecules, polysaccharides and proteins migrated slowly, being BSA the slowest.

4.3.2.3 Flow delivery control

Figure 4.4 shows a plot for 4-step controlled delivery of a solute band into the GelMA hydrogel: (I) band delivery from thread to the hydrogel (field on); (II) diffusion through the gel (field off); (III) equilibration (field off); and (IV) removal (field on). The spatial distribution of FL fluorescence was monitored versus time to determine the amount of FL in the hydrogel for each step of the process.

This light was monitored using a microscope and images/videos were treated through ImageJ. Light threshold was kept constant, and the FL distribution area was determined by selecting the ROI (region of interest) area. In this case, 0.5 pg of FL loaded upon the thread inlet segment was delivered as a band towards the hydrogel, when a current of 50

μA was applied. In step (I), the radial distribution increased as the band entered in the hydrogel at a constant velocity of 3.53 μm s^{-1}. A slight increase in area was observed due to band broadening of the solute zone. Once the band reached the middle of the gel, the voltage was turned off (at 4.5 min). Then, as shown in step (II), FL diffused into the 3D hydrogel space – as area per unit time (with an average of 0.45 mm^2/min), described by Fick's law. Approximately 11 min were needed to cover the entire 3D space of the hydrogel with FL. Although 100% of the area was occupied, a concentration gradient from the thread source to the gel walls was observed. Therefore, in step (III) and with voltage still off, the system was left for an extra 9 minutes to equilibrate and achieve a uniform concentration throughout the hydrogel.

Line-scanning mode of ImageJ was used to determine the light intensity vs. single pixel-wide to recreate a plot of intensity profile along the delivery axis. Uniform concentration throughout the hydrogel was set when peak height was < 10 a.u. (pixel intensity), less than 3 times the standard deviation of noise level. No loss of FL out of the hydrogel was observed during the 20 minutes without any applied electric field. Finally, in step (IV), the electric field was again activated at 100 μA to remove the FL. The removal rate was constant over time, taking 6.03 min to eliminate FL completely from the platform. Removal velocity of the FL was measured to be 6.90 μm s^{-1}. Note that at 100 μA the speed of the FL was almost doubled compared with step (I) where the current was only 50 μA.

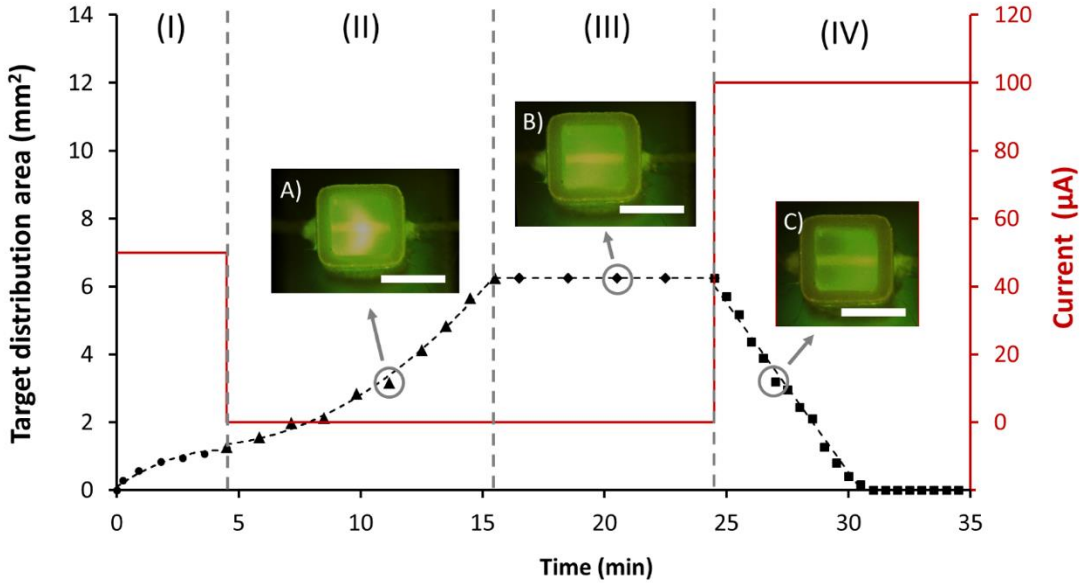

Figure 4.4 Controlled delivery via electric field into 3D GelMA hydrogel supports. Distribution area of fluorescein (FL, a model compound) within hydrogel with stiffness of 4.3 kPa as a function of time in 4 different steps. Buffer used w(I) band delivery, 50 µA, 4.5 min (●); (II) molecular diffusion, 11 min (▲); (III) equilibration, 9 min (♦); and (IV) excess removal, 100 µA, 10 min (■). Solid line represents the current applied. Representative images were taken at minutes 11.17 (insert A), 20.50 (insert B), and 27.00 (insert C). Trend line for excess removal was y = -0.9973x + 0.445, R-squared = 0.9887. Scale bars is 2.5 mm. Conditions were the same as for Figure 4.1.

4.3.3 Drug delivery using sutures

The performance of several commercially available sutures was investigated using several electrolytes with increasing conductivity. Figure 4.5A shows the total resistance (R_T) for the electrolytes within acrylic thread with polyglicolic acid (PGA) suture using 4 different biological buffers with conductivities ranging from 0.0159 to 0.585 S/m. The resistance is uniquely determined by the amount and conductivity of liquid that the thread is holding. Reducing the suture diameter (PGA with low USP size) and using a braided structure saw the total resistance being increased, allowing higher buffer concentrations to be used, typically more compatible for cell viability. Using 5% PBS

(0.585 S/m) at a constant current of 250 µA, voltage was reduced to only 5.42 V between each extreme of a 15 mm^3 hydrogel (2.5 mm long, 2.17 V/mm). This voltage was considered acceptable although it could be lowered further by increasing the length of the hydrogel chamber. Using the previous buffers (0.0159 S/m), a current of 250 µA would increase too much the voltage in the hydrogel, causing Joule heating effects and swelling.

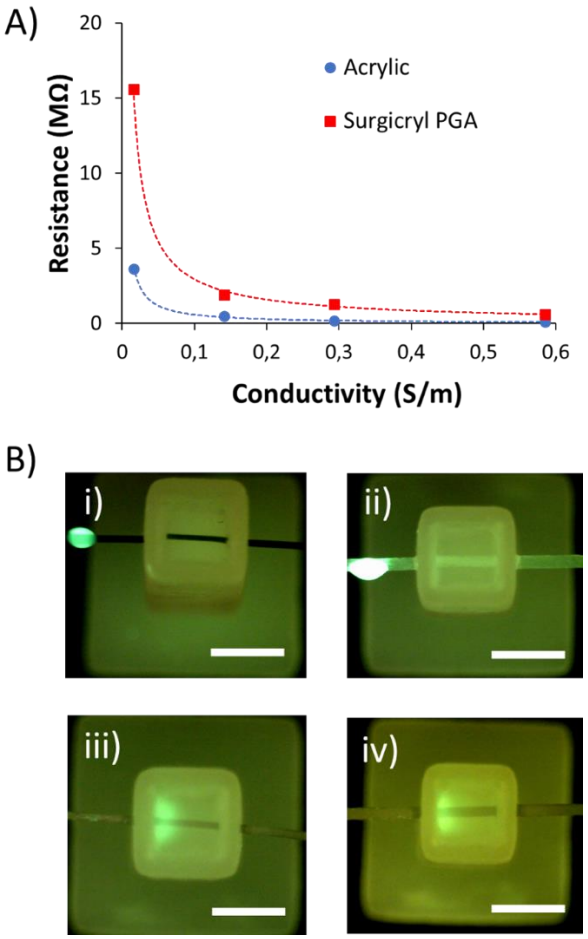

Figure 4.5 Thread conductivity

(A) Electrolyte resistance versus conductivity comparison between acrylic thread (diameter 670 µm) and surgicryl PGA (USP 0). Electrolytes were 5 mM Tris/HEPES (0.0159 S/m), 50 mM Tris/HEPES (0.141 S/m), 2.5 % PBS (0.293 S/m), and 5% PBS (0.585 S/m) (B) Representative pictures depicting the parts and delivery process of

fluorescein (FL, a model compound) taken after 4 minutes of applied current for 4 sutures: i) Nylon (Ethilon, monofilament); ii) Polyamide (Supramid, twisted and coated); iii) Polyglactin 910 (Vycril, braided and coated); iv) Polyglicolic acid (Surgicryl, braided and coated). Stiffness of the hydrogel was 4.3 kPa. Sample was loaded upon thread inlet segment with a 2 μL drop of a 1.0 μg/mL solution of FL. Scale bar is 2.5 mm.

Nine commercially available sutures produced from different materials, structures, sizes, and water absorption characteristics were tested (Table 4.1). From these materials, polyester, polyglactin 910, glycolide/lactide copolymer, and polyglycolic acid created adequate fluid connection between the electrodes and the hydrogel (Figure 4.5B). Initial delivery speeds ranged from 2.3 to 3.4 μm s^{-1}. However, the velocity decreased when the compound fully entered the gel. As commented previously, using 5% PBS and 250 μA the voltage in the hydrogel was very low. For this reason, the measurement of the velocity in GelMA was extremely challenging and it is not shown.

Table 4.1 Chemical composition, structure, absorbability, and size of sutures.
Drug delivery speed of FL was measured for first 5 minutes of delivery at 250 μA, 5% PBS. Conditions were the same as for Figure 4.5. Standard deviation based on 3 experiments.

Name®	**Composition**	**Properties**	**Absorbable**	**Size (USP)**	**Delivery (μm s^{-1})**
Monocryl	Poliglecaprone 25	Monofilament	91 - 119days	3/0	No
Prolene	Polypropylene	Monofilament	No	3/0	No
Ethilon	Nylon	Monofilament	No	3/0	No
Supramid	Polyamide based	Twisted and coated	No	0	No
Silk	Silk	Braided	No	3/0	No
Polyester	Polyester	Braided	No	4/0	3.4 ± 0.4
Vicryl	Polyglactin 910	Braided and coated	56 - 70 days	3/0	3.0 ± 0.3
Polysorb	Glycolide/Lactide copolymer	Braided and coated	56 - 70 days	3/0	2.9 ± 0.3
Surgicryl	Polyglycolic acid	Braided and coated	60 - 90 days	0	2.3 ± 0.3

To demonstrate a potential application for controlled localized delivery, the delivery of an anti-inflammatory drug, dexamethasone 21-phosphate disodium salt (DSP), was investigated. DSP is a prodrug of dexmathasone that is used to treat many different inflammatory conditions including skin inflammatory diseases and wound treatment. To monitor the amount of DSP delivered, buffer electrolyte from both inlet and outlet was examined using an HPLC. With an applied current of 250 μA, DSP was moving slowly enough to be diffused off the suture and spread within the 3D hydrogel space. After applying the electric field for 1 hour, DSP was only observed in the outlet reservoir at very low concentrations (0.096 ppm), indicating 97.6% was still in the hydrogel. When the electric field was applied for 2 hours, the percentage remaining within the hydrogel was reduced to 81.1% of the drug. Furthermore, no DSP was found in the inlet reservoir, proving that 100% of DSP was directed to the desired location and remained there for this period, which would be essential for its actuation in the target area. The applied electric field may also cause compounds presenting within the hydrogel to migrate toward their oppositely charged electrode. Thus, there is significant potential here to simultaneously monitor metabolites or products arising from the delivery of a bioactive agent. Moreover, this setup could also be used to study drug-cell interactions since metabolites and biomolecules of potential interest can be removed at will from the hydrogel for their analytical determination, leaving the surviving cells in place.

4.4 Discussion

Electrofluidic dynamics depend mostly on the physicochemical properties of the thread, the physical properties of the hydrogel, and the composition of the electrolyte/buffer used.[138, 141] Thread resistance (referred to the buffer suspended in the thread) changes with the thread diameter, length and wettability (material hydrophilicity), whereas hydrogel electrical resistance depends on gel dimensions, structure of crosslinked networks and water content (Figure 4.S2).[138]

Electrolyte composition is also important, as increases in concentration or conductivity will lead to higher currents. The magnitude of the applied current and polarity determine both speed and direction (migration) of the solutes upon the thread. If a bioactive species is present, its velocity would increase with the magnitude of the current.[138] Due to the change in cross-sectional area, the magnitude of the current density is higher along the bare thread, whereas it is substantially lower and spatially distributed within the hydrogel. Consequently, the bioactive velocity is reduced when it enters the hydrogel.

Structurally, braided sutures presented better connectivity, as they exhibit greater flow-through properties, arising from the open braided structure, thus allowing a continuous and homogeneous distribution of the electrolyte. However, braided silk sutures, a protein based natural suture from the species *Bombyx mori*, could not be used as these commercial sutures are typically processed to remove the natural waxes and gums, and coated with a special wax mixture that prevents electrolyte penetrating into the filaments.[246] Overall, the sutures which showed acceptable delivery performance can be applied in main medical indications (skin, gastro-intestinal, uterus, hernia,

orthopaedics, ophthalmic procedures, oral cavity, and muscle). Detailed information on indication and contra-indication from these sutures can be found in Table 4.S1 from the supporting information.

As illustrated in Figure 4.1, the 3D printed platform enabling this study comprised of several parts: two reservoirs containing buffer and electrodes into which each end of the thread is immersed. The thread travels from one reservoir to the other through the gel. When current is applied between the two buffer chambers, a heterogeneous electrical system is created, as shown in Figure 4.1B. Neither sutures/threads nor hydrogels are electrically conductive. Electrolyte serve as ionic conducting medium. When external electric field was applied, the electrokinetic phenomenon of electrophoresis was observed and ultimately caused the presence of a charged interface on the surface and the consequent migration of molecules.

By controlling electric field and polarity, small molecules, drugs or growth factors can be dispatched in a controlled manner throughout the gel. The advantages of this approach are that the rate of delivery can be controlled and, by controlling field on / field off times, spatial control over the displacement of the molecule is achieved.

For an effective targeted delivery, the drug should move quickly in the suture but slowed down when it is diffused off the suture to the gel, so that the desired biological effect can be produced. This would benefit several biological processes such as more efficient passive diffusion to a cell membrane or increase drug absorption for those with low permeable coefficients. To achieve that, modifications in electrolyte resistances were carried out, thus minimizing the electric field applied in the hydrogel and therefore the velocity (Equation 6S).

4.5 Conclusion

Herein, a novel system to release bioactive molecules such as small molecules, drugs, polysaccharides, or proteins in a controlled manner via an electric field into tissue-like 3D hydrogel supports was reported. Threads and commonly employed sutures were successfully assembled in GelMA-based hydrogels to facilitate the introduction of bioactive species, and to deliver them via controlled diffusion to fill a desired 3D space. Targeted drug delivery currently covers all means of delivering a bioactive species to a target region, point, or receptor within a biological system; and covers bulk targeted delivery (to a region) and selective drug delivery (to a specific receptor point, cell type or other target biomolecule/species). Surgical sutures and electric field were put together to deliver bioactive species into tissue-like materials. This work could use commonly employed sutures as the delivery conduit to deliver anti-inflammatory drugs for treatment of skin inflammatory diseases and wound infection. In addition, these early assemblies demonstrate the possibility of using such scaffolds for applications in bio-sensing and drug screening.

Supplementary information

Theory

Electric field intensity, E (V/m), in a heterogenous system formed by a connection of different cross-sectional parts (2 equal length thread/surgical suture and 1 hydrogel) is described by the following relationship:

$$E = \frac{V}{L} = \frac{V_T}{L_{thd} + \frac{L_{Gel}}{\chi^2}} = \frac{V_T}{L_{thd} + \frac{L_{Gel}}{\left(\frac{A_{Gel}}{\pi r^2}\right)^2}} \qquad (1S)$$

where V_T is the voltage applied (V), L_{thd} and L_{Gel} are the length of the individual parts of the thread and GelMA hydrogel (m), χ is the ratio of the internal cross-sections of the parts, A_{Gel} is the cross-section area of the hydrogel (m^2), and r the radius of the thread (m). Therefore, voltage in GelMA hydrogel (V_{Gel}) and thread (V_{thd}) can be calculated by:

$$V_{thd} = IR_{thd} = I\frac{L_{thd}\rho_{thd}}{\pi r^2} = EL_{thread} \qquad (Eq.\ 2S)$$

$$V_{thd} = IR_{Gel} = I\frac{L_{Gel}\rho_{Gel}}{A_{Gel}} = EL_{Gel} \qquad (Eq.\ 3S)$$

where I is the current intensity (A), R_{thd} is the resistance of the thread (Ω), R_{Gel} the resistance of the gel (Ω), and ρ_{thd} and ρ_{Gel} are the respective resistivities of the thread and the gel (Ω cm). Knowing I, voltage, and dimension of the thread and gel, ρ_{thd} and ρ_{Gel} can be calculated using a modified equation from 2S and 3S.

The change in resistance (f) can be calculated by:

$$f = \frac{R_{thd}}{R_{Gel}} = \frac{\frac{L_{thd}\rho_{thd}}{\pi r^2}}{\frac{L_{Gel}\rho_{Gel}}{A_{Gel}}} \qquad (Eq.\ 4S)$$

Supposing that $\rho_{thd} = \rho_{Gel}$, when a hydrogel of 2.5×2.5×2.4 mm (xyz; 15 µL) and a thread of radius 335 µm are used, the resistance within the hydrogel is 17-times lower. Whereas, if the thread radius is reduced to 100 µm, hydrogel resistance becomes 190-times lower.

Velocity of the band ($\bar{v}$, m s^{-1}) can be calculated as a function of the effective length (L_{ef}, m) and time, or the apparent mobility ($\bar{\mu}$, $m^2V^{-1}s^{-1}$), from the following:

$$\bar{v} = \frac{L_{ef}}{t} = \bar{\mu}E \qquad \text{(Eq. 5S)}$$

Since the flow of the bulk solution is 0, $\bar{\mu}$ equals the electrophoretic mobility (μ_e) and therefore this equation can be rewritten as:

$$\bar{v} = \mu_e E = \frac{qE}{6\pi\eta r} = \frac{qV}{6\pi\eta r(L_{thd} + L_{Gel})} \qquad \text{(Eq. 6S)}$$

where q and r are the charge of the respective ion charge and radius of the molecule, and η the viscosity (Pa·s) of the solution.

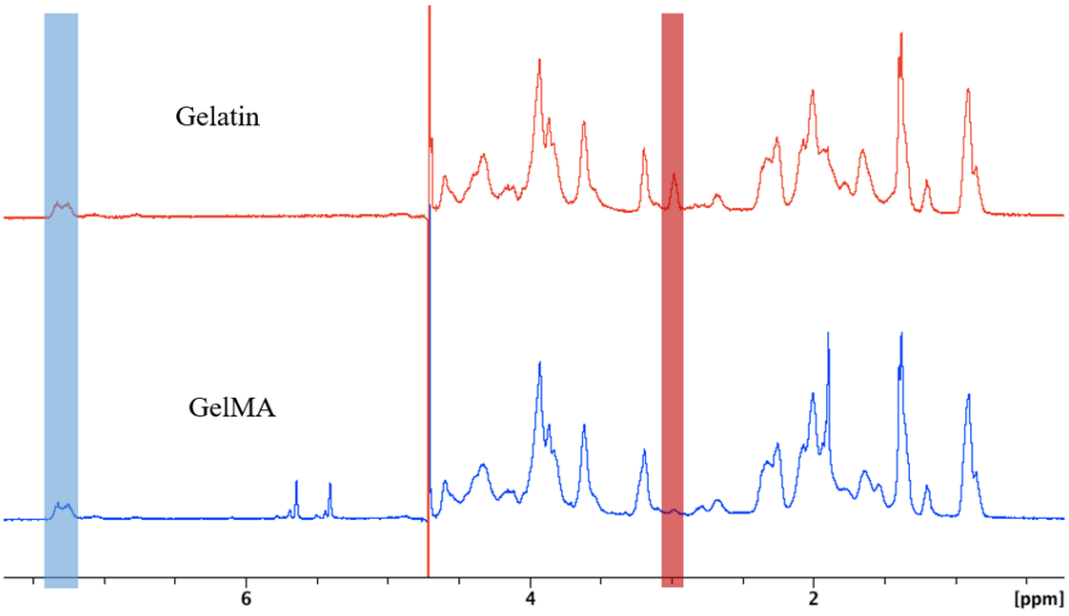

Figure 4.S 1 NMR spectra of gelatin and GelMA.

The red band is the lysine peak (2.8–3.0 ppm) used to quantify the degree of methacrylation. In each spectrum, the integration of the lysine peak is normalised by that of the phenylalanine peak (7.1–7.4 ppm, blue band).

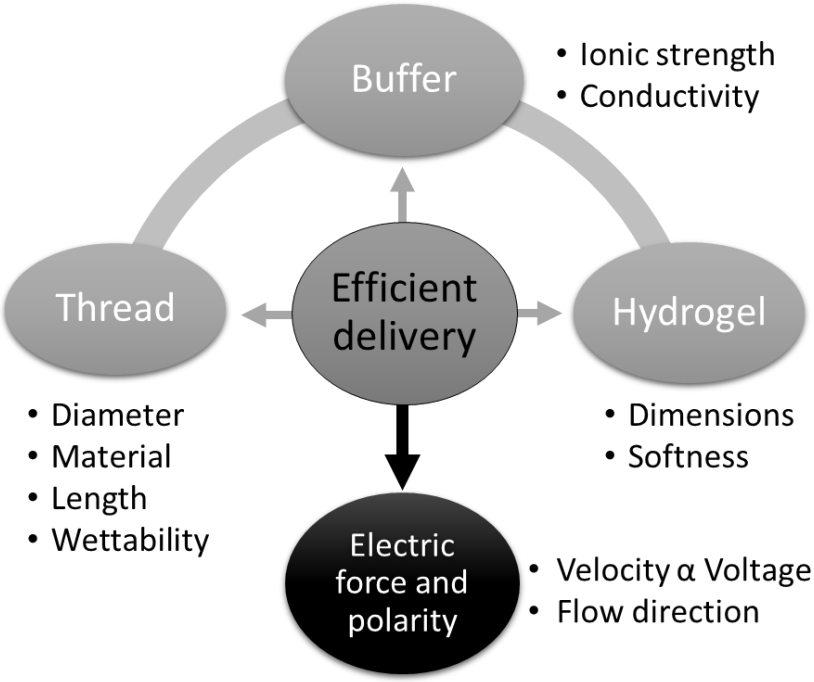

Figure 4.S 2 Schematic diagram depicting each of the electrodynamic considerations for the thread – hydrogel system.

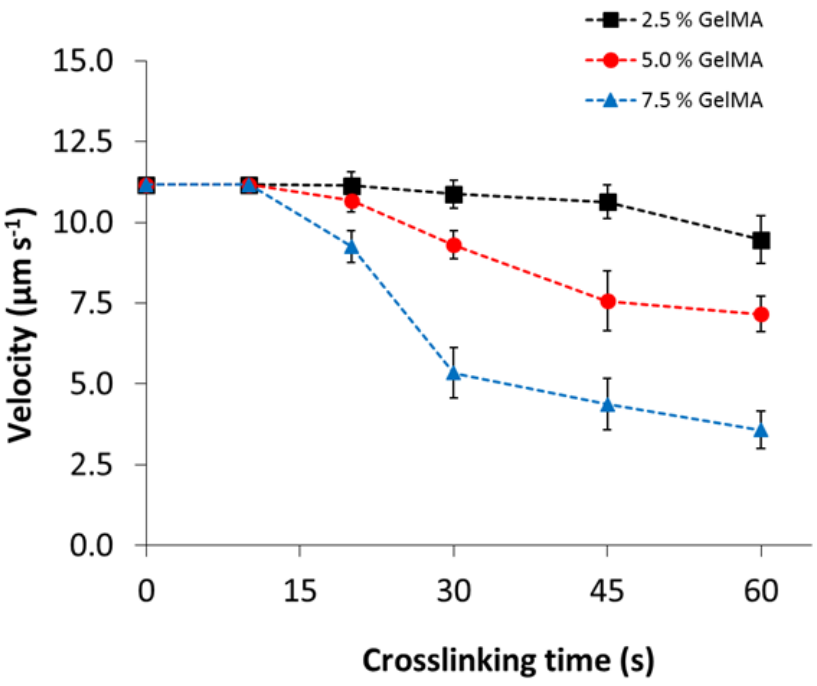

Figure 4.S 3 Speed of FL in the hydrogel

prepared from 2.5, 5.0, or 7.5 % of GelMA as a function of the crosslinking time. The velocity clearly decreased with increasing GelMA concentration and photo-crosslinking time. At low cross-linking times (≤~20 s), where the hydrogels were softer, velocities

were much faster, close to that prior to the photocrosslinking (velocity of 11.17 μm s^{-1}). Conditions: 0.5 pg of sample was dropped on acrylic and 100 μA was applied for electric field. Error bars are based on the standard deviation of 3 replicates.

Table 4.S 1 Compilation of indication/contra-indication from sutures studied in this work.

Name	Composition	Brand	Indication	Contra-indication
Monocryl	Poliglecaprone 25	Ethicon	General soft tissue approximation and/or ligation; subcuticular skin closure	Cardiovascular or neurological tissues, microsurgery or ophthalmic surgery; where extended approximation of tissue under stress is required.
Prolene	Polypropylene	Ethicon	General soft tissue approximation and/or ligation; cardiovascular, ophthalmic, and neurological procedures.	Where extended approximation of tissue is required.
Ethilon	Nylon	Ethicon	General soft tissue approximation and/or ligation; cardiovascular, ophthalmic, and neurological procedures.	Where permanent retention of tensile strength is required.
Supramid	Polyamide	SMI	General soft tissue approximation and/or ligation; skin closure.	Where extended approximation of tissue is required .
Silk	Silk	Ethicon	General soft tissue approximation and/or ligation; cardiovascular, ophthalmic, and neurological procedures.	Where permanent retention of tensile strength is required.
Vicryl	Polyglactin 910	Ethicon	General soft tissue approximation and/or ligation; ophthalmic procedures.	Cardiovascular and neurological tissues; where extended approximation of tissue is required.
Polysorb	Glycolide/lactide copolymer	Covidien	General soft tissue approximation and/or ligation; ophthalmic procedures.	Cardiovascular and neurological tissues; where extended approximation of tissue is required.
Surgicryl	Polyglycolic acid	SMI	General soft tissue approximation and/or ligation; general surgery, skin closure, gastrointestinal surgery, gynaecology, obstetrics, plastic surgery, urology, ophthalmic surgery, orthopaedics.	Cardiovascular and neurological tissues; where extended approximation of tissue is required.
Polyester	Polyester	Keebomed	General soft tissue approximation and/or ligation; cardiovascular, ophthalmic, and neurological procedures.	Only veterinary use in the USA / can be used in human or veterinary procedures in other countries.

4.6 References

[124] X. Zhao, Q. Lang, L. Yildirimer, Z.Y. Lin, W. Cui, N. Annabi, K.W. Ng, M.R. Dokmeci, A.M. Ghaemmaghami, A. Khademhosseini, Photocrosslinkable Gelatin Hydrogel for Epidermal Tissue Engineering, Advanced healthcare materials 5(1) (2016) 108-118.

[136] S. Farajikhah, J.M. Cabot, P.C. Innis, B. Paull, G. Wallace, Life-Saving Threads: Advances in Textile-Based Analytical Devices, ACS Comb Sci 21(4) (2019) 229-240.

[137] C. Zhao, S. Farajikhah, C. Wang, J. Foroughi, X. Jia, G.G. Wallace, 3D braided yarns to create electrochemical cells, Electrochemistry Communications 61 (2015) 27-31.

[138] J.M.J.M. Cabot, N.P.N.P. Macdonald, S.C.S.C. Phung, M.C. Breadmore, B. Paull, Fibre-based electrofluidics on low cost versatile 3D printed platforms for solute delivery, separations and diagnostics; from small molecules to intact cells, The Analyst 141(23) (2016) 6422-6431.

[139] R. Safavieh, G.Z. Zhou, D. Juncker, Microfluidics made of yarns and knots: from fundamental properties to simple networks and operations, Lab on a chip 11(15) (2011) 2618-2624.

[140] P. Mostafalu, M. Akbari, K.A. Alberti, Q. Xu, A. Khademhosseini, S.R. Sonkusale, A toolkit of thread-based microfluidics, sensors, and electronics for 3D tissue embedding for medical diagnostics, Microsystems & Nanoengineering 2(April) (2016) 16039-16039.

[141] J.M. Cabot, M.C. Breadmore, B. Paull, Thread based electrofluidic platform for direct metabolite analysis in complex samples, Analytica Chimica Acta (2017).

[142] X. Li, J. Tian, W. Shen, Thread as a versatile material for low-cost microfluidic diagnostics, ACS Applied Materials and Interfaces 2(1) (2010) 1-6.

[143] M. Reches, K.A. Mirica, R. Dasgupta, M.D. Dickey, M.J. Butte, G.M. Whitesides, Thread as a Matrix for Biomedical Assays, ACS Applied Materials and Interfaces 2(6) (2010) 1722-1728.

[144] S. Ramesan, A.R. Rezk, K.W. Cheng, P.P.Y. Chan, L.Y. Yeo, Acoustically-driven thread-based tuneable gradient generators, Lab Chip 16(15) (2016) 2820-2828.

[145] A. Nilghaz, S. Hoo, W. Shen, X. Lu, P.P.Y. Chan, Multilayer cell culture system supported by thread, Sensors and Actuators, B: Chemical 257 (2018) 650-657.
[224] M.W. Tibbitt, K.S. Anseth, Hydrogels as extracellular matrix mimics for 3D cell culture, Biotechnology and Bioengineering 103(4) (2009) 655-663.
[225] K.Y. Lee, D.J. Mooney, Hydrogels for Tissue Engineering, Chemical Reviews 101 (2001) 7-7.
[226] A.S. Hoffman, Hydrogels for biomedical applications, Advanced Drug Delivery Reviews 64 (2012) 18-23.
[227] K. Rahali, G. Ben Messaoud, C. Kahn, L. Sanchez-Gonzalez, M. Kaci, F. Cleymand, S. Fleutot, M. Linder, S. Desobry, E. Arab-Tehrany, Synthesis and Characterization of Nanofunctionalized Gelatin Methacrylate Hydrogels, International Journal of Molecular Sciences 18(12) (2017) 2675-2675.
[228] J. Zhu, R.E. Marchant, Design properties of hydrogel tissue-engineering scaffolds, Expert Review of Medical Devices 8(5) (2011) 607-626.
[229] T.R. Hoare, D.S. Kohane, Hydrogels in drug delivery: Progress and challenges, Polymer 49(8) (2008) 1993-2007.
[230] E.R. Ruskowitz, M.P. Comerford, B.A. Badeau, C.A. DeForest, Logical stimuli-triggered delivery of small molecules from hydrogel biomaterials, Biomater Sci 7(2) (2019) 542-546.
[231] D. Loessner, C. Meinert, E. Kaemmerer, L.C. Martine, K. Yue, P.A. Levett, T.J. Klein, F.P.W. Melchels, A. Khademhosseini, D.W. Hutmacher, Functionalization, preparation and use of cell-laden gelatin methacryloyl–based hydrogels as modular tissue culture platforms, Nature Protocols 11(4) (2016) 727-746.
[232] J.W. Nichol, S.T. Koshy, H. Bae, C.M. Hwang, S. Yamanlar, A. Khademhosseini, Cell-laden microengineered gelatin methacrylate hydrogels, Biomaterials 31(21) (2010) 5536-44.
[233] J.A. Benton, C.A. DeForest, V. Vivekanandan, K.S. Anseth, Photocrosslinking of gelatin macromers to synthesize porous hydrogels that promote valvular interstitial cell function, Tissue engineering. Part A 15(11) (2009) 3221-30.
[234] L.E. Bertassoni, M. Cecconi, V. Manoharan, M. Nikkhah, J. Hjortnaes, A.L. Cristino, G. Barabaschi, D. Demarchi, M.R. Dokmeci, Y. Yang, A. Khademhosseini, Hydrogel bioprinted microchannel networks for vascularization of tissue engineering constructs, Lab Chip 14(13) (2014) 2202-2211.

[235] K. Yue, G. Trujillo-de Santiago, M.M. Alvarez, A. Tamayol, N. Annabi, A. Khademhosseini, Synthesis, properties, and biomedical applications of gelatin methacryloyl (GelMA) hydrogels, Biomaterials 73 (2015) 254-271.
[236] B.J. Klotz, D. Gawlitta, A.J.W.P. Rosenberg, J. Malda, F.P.W. Melchels, Gelatin-Methacryloyl Hydrogels: Towards Biofabrication-Based Tissue Repair, Trends in Biotechnology 34(5) (2016) 394-407.
[237] C.D. O'Connell, C. Di Bella, F. Thompson, C. Augustine, S. Beirne, R. Cornock, C.J. Richards, J. Chung, S. Gambhir, Z. Yue, J. Bourke, B. Zhang, A. Taylor, A. Quigley, R. Kapsa, P. Choong, G.G. Wallace, Development of the Biopen: a handheld device for surgical printing of adipose stem cells at a chondral wound site, Biofabrication 8(1) (2016) 015019-015019.
[238] G. Eke, N. Mangir, N. Hasirci, S. MacNeil, V. Hasirci, Development of a UV crosslinked biodegradable hydrogel containing adipose derived stem cells to promote vascularization for skin wounds and tissue engineering, Biomaterials 129 (2017) 188-198.
[239] M.M. Fares, E. Shirzaei Sani, R. Portillo Lara, R.B. Oliveira, A. Khademhosseini, N. Annabi, Interpenetrating network gelatin methacryloyl (GelMA) and pectin-g-PCL hydrogels with tunable properties for tissue engineering, Biomater Sci 6(11) (2018) 2938-2950.
[240] C.T. McKee, J.A. Last, P. Russell, C.J. Murphy, Indentation Versus Tensile Measurements of Young's Modulus for Soft Biological Tissues, Tissue Engineering Part B: Reviews 17(3) (2011) 155-164.
[241] D.L. Bader, P. Bowker, Mechanical characteristics of skin and underlying tissues in vivo, Biomaterials 4(4) (1983) 305-308.
[242] E. Kaemmerer, F.P.W. Melchels, B.M. Holzapfel, T. Meckel, D.W. Hutmacher, D. Loessner, Gelatine methacrylamide-based hydrogels: An alternative three-dimensional cancer cell culture system, Acta Biomaterialia 10(6) (2014) 2551-2562.
[243] W. Schuurman, P.A. Levett, M.W. Pot, P.R. van Weeren, W.J. Dhert, D.W. Hutmacher, F.P. Melchels, T.J. Klein, J. Malda, Gelatin-methacrylamide hydrogels as potential biomaterials for fabrication of tissue-engineered cartilage constructs, Macromol Biosci 13(5) (2013) 551-61.
[244] X. Li, S. Chen, J. Li, X. Wang, J. Zhang, N. Kawazoe, G. Chen, 3D Culture of Chondrocytes in Gelatin Hydrogels with Different Stiffness, Polymers (Basel) 8(8)

(2016).
[245] C.D. O'Connell, B. Zhang, C. Onofrillo, S. Duchi, R. Blanchard, A. Quigley, J. Bourke, S. Gambhir, R. Kapsa, C. Di Bella, P. Choong, G.G. Wallace, Tailoring the mechanical properties of gelatin methacryloyl hydrogels through manipulation of the photocrosslinking conditions, Soft Matter 14(11) (2018) 2142-2151.
[246] D.L. Dunn, J. Phillips, Wound Closure Manual, Ethicon, Inc., University of Minnesota, 2007.

5 Chapter

Conclusion and Future Directions

Table of Contents

5.1 Conclusion

In the last decade, the advent of 3D printing and electrofluidic devices for tissue engineering and regenerative medicine has engendered great interest for those involved in skin repair and regeneration. 3D bioprinting allows spatial distribution of skin cells into predefined custom-made structures to produce living skin mimics on the bench for grafting. Electrofluidic technology, on the other hand, can be applied for fine controlled delivery of bioactive molecules/drugs.

Therefore, the work presented in this thesis focused to meet challenges of traditional approaches by describing for the first time, two innovative delivery system platforms which could be potentially integrated or used separated in wound management.

Chapter 1 presents a general overview of the skin physiology, skin cells and extra cellular components, stages of the wound healing process, compelling needs for advance wound healing products, and emerging technologies to solve current gaps in the clinic including bioprinting and electrofluidic approach. This chapter formed the basis of a first author review recently submitted to the journal Advanced Functional Materials entitled ‘Bioprinting for complex skin constructs fabrication’ 2021.

In chapter 2, studies aimed at establishing a foundation towards the development of a more complex skin equivalent with complete functional performance were presented. The results based on formulating a bioink containing PL and GelMA bioink (PLGMA), which would work as a scaffold for encapsulation of skin cells and delivery of growth factors while also mimicking key characteristics of native skin were presented. This bioink was then used for the biofabrication of the PLGMA dermal-like structure and this structure was used for initial *in vitro* characterisation. The results showed great

promise in several aspects of skin tissue engineering, including high cytocompatibility towards HDF, as well as promoting cell attachment and proliferation. Further benefits of this system include increased synthesis and deposition of ECM molecules. This work constitutes the major part of a first author paper that appears in the journal Acta Biomaterialia 2021.[109]

In chapter 3, the fabrication of a more complex skin equivalent structure was proposed by developing an innervated double layer skin-like structure based on the platform HDF-PLGMA established on chapter 3. Although this study had to be interrupted because of the coronavirus pandemic and the integration of the bilayer skin construct with the innervated component could not be performed, initial studies demonstrated that the PLGMA platform supported good cell-matrix interaction and provided optimal microenvironment for differentiation of keratinocytes and hNSC-H9 neurospheres when it was co-cultured with printed fibroblasts. In a proof-of-concept study, co-culture of keratinocytes and fibroblasts in a 3D printed PLGMA construct reported very distinct morphology in each layer (dermal and epidermal layer) in histological analysis. HDF-PLGMA construct also demonstrated to support neurite outgrowth and maturation of hNSC-H9 neurospheres over the period of 2 weeks of culture.

Chapter 4 details a novel electrofluidic/suture (e-suture) approach for controlled delivery, which could be potentially used to deliver anti-inflammatory drugs such as dexamethasone 21-phosphate disodium salt (DSP) for treatment of skin inflammatory diseases and wound infection. This system was designed for precise manipulation of fluids on commonly employed surgical sutures to deliver biomolecules into and throughout a soft tissue model based on gelatin methacryloyl (GelMA) hydrogel, via control of an applied electric field. In a proof-of-concept study, the proposed system

showed great potential in delivering bioactive molecules such as small molecules, drugs, polysaccharides, or proteins in a controlled manner via an electric field into tissue-like 3D hydrogel supports. The advantages afforded by this delivery system are: 1) delivery can be turned on and off when needed; 2) during delivery the rate can be controlled; 3) by alternating the field on/off, spatial control over the drug delivery is possible; 4) the thread / suture chemistry can be modified to afford control over the interaction and hence release of the bioactive species. This work was part of a collaboration with Dr Joan Marc Cabot and Dr Brett Paull from University of Tasmania and constitutes a significant component of a co-authored paper that appears in Scientific Reports 2020.[247]

5.2 Future directions

Future direction for the first 3D printed PLGMA platform involves 3D printing of the dermal, epidermal and nerve component as well as incorporation of other relevant cells/components, such as vascular components and other cutaneous appendages to develop a fully functional skin equivalent. Future studies will also involve demonstration of antimicrobial activity of PLGMA constructs against common airborne bacteria, and in-depth studies *in vivo* (e.g., swelling and degradation studies, wound healing histological analysis as well as evaluation of the construct adhesion strength to the wound bed) to assess the therapeutic efficacy of the proposed PLGMA platform in supporting skin tissue regeneration.

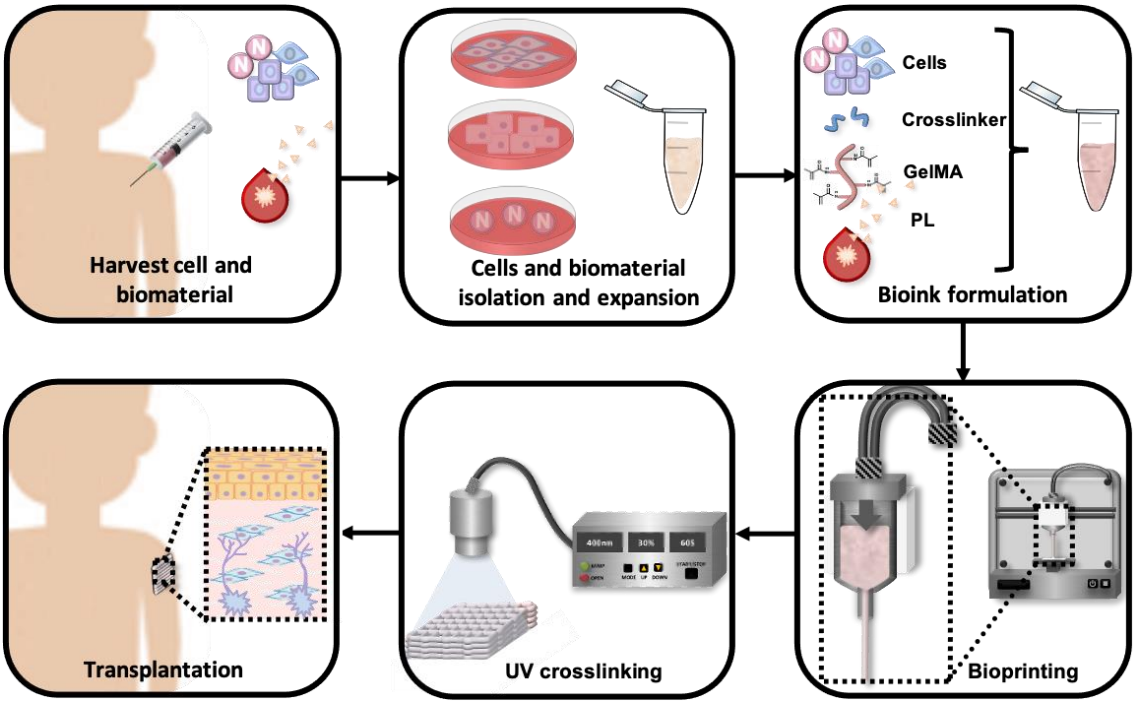

Figure 5.1 Schematic representation of the cell laden PLGMA 3D printed construct for wound healing application.

Illustration shows the application of the proposed biosynthetic skin construct in the clinic, implemented in a customizable and personalized approach. In this setting, cells

and PL would be harvested from the patient, expanded in the lab, encapsulated into the PLGMA bioink, crosslinked, culture in the lab to allow matrix maturation by ECM secretion, and implantation back to the patient, potentially promoting good cosmetic/functional outcome.

Future directions for the e-suture includes redesign of the system, as current system is not portable and would require long period of immobilization of an animal model for the delivery of the bioactive molecules to be achieved. Therefore, further investigation of the feasibility of the system will include the design of a portable system coupled with a portable battery (which would provide the electric field), *in vivo* studies involving the delivery of antimicrobial peptides to medium-sized animal model; and histological analysis by hematoxylin and eosin staining for comparison of the wound healing of an infected wound to an infected wound which received antimicrobial peptides through the e-suture system.

PLGMA 3D skin construct and the e-suture systems described in this thesis could also be integrated in the future by printing skin cell-PLGMA on top of the e-suture system to create a skin equivalent electric-fluid device for better delivery control of relevant molecules for wound management.

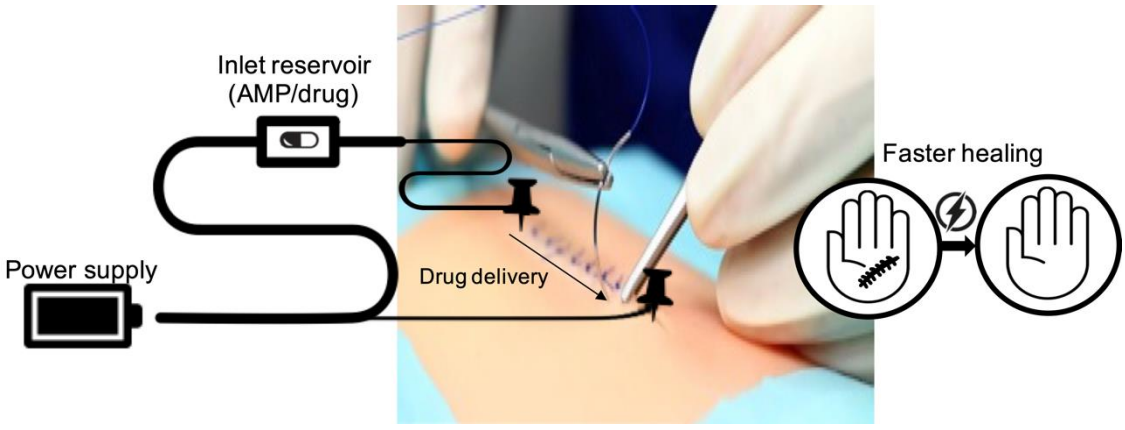

Figure 5.2 Schematic representation of the e-suture system for would healing application. Illustration of the portable device and its final application in the clinic. Re-designing the device would enable more flexibility to generate electric current for controlled delivery of drugs to the sutured wound.

Although it is still at an early stage, bioprinting and electrofludic technology holds great promise of producing living skin-mimicking tissues and delivery systems for medical testing and clinical applications. It is envisaged those technologies will advance further to alleviate the situation of an unmet need in skin transplantation. Yet, collaborative work between academia, industry and regulations will be essential to move the field forward. Advances in the regulatory frameworks and guidelines applicable to 3D bioprinting and microfludics devices are needed to enable the translation of those discoveries towards the use in a clinical setting. In order to facilitate development of these technologies while protecting patients, it is important to ensure quality and safety of materials and cells and establish specific standards for each stage of the printing process with appropriate printing validation methods, and quality assessment.

5.3 References

[109] L.Y. Daikuara, Z. Yue, D. Skropeta, G.G. Wallace, In vitro characterisation of 3D printed platelet lysate-based bioink for potential application in skin tissue engineering, Acta Biomaterialia 123 (2021) 286-297.

[247] J.M. Cabot, L.Y. Daikuara, Z. Yue, P. Hayes, X. Liu, G.G. Wallace, B. Paull, Electrofluidic control of bioactive molecule delivery into soft tissue models based on gelatin methacryloyl hydrogels using threads and surgical sutures, Scientific reports 10(1) (2020) 7120-7120.